

TRAJECTORY COMPUTATION OF SMALL SOLID PARTICLES  
RELEASED AND CARRIED BY FLOWFIELDS OF HELICOPTERS IN  
FORWARD FLIGHT

A THESIS SUBMITTED TO  
THE GRADUATE SCHOOL OF NATURAL AND APPLIED SCIENCES  
OF  
MIDDLE EAST TECHNICAL UNIVERSITY

BY

YUSUF OKAN PEKEL

IN PARTIAL FULFILLMENT OF THE REQUIREMENTS  
FOR  
THE DEGREE OF MASTER OF SCIENCE  
IN  
AEROSPACE ENGINEERING

JANUARY 2010

Approval of the thesis:

**TRAJECTORY COMPUTATION OF SMALL SOLID PARTICLES  
RELEASED AND CARRIED BY FLOWFIELDS OF HELICOPTERS IN  
FORWARD FLIGHT**

submitted by **YUSUF OKAN PEKEL** in partial fulfillment of the requirements  
for the degree of **Master of Science in Aerospace Engineering**  
**Department, Middle East Technical University** by,

Prof. Dr. Canan Özgen \_\_\_\_\_  
Dean, Graduate School of **Natural and Applied Sciences**

Prof. Dr. Ozan Tekinalp \_\_\_\_\_  
Head of Department, **Aerospace Engineering**

Prof. Dr. Yusuf Özyörük \_\_\_\_\_  
Supervisor, **Aerospace Engineering Dept., METU**

Prof. Dr. Nafiz Alemdaroğlu \_\_\_\_\_  
Co-Supervisor, **Aerospace Engineering Dept., METU**

**Examining Committee Members:**

Prof. Dr. Serkan Özgen \_\_\_\_\_  
Aerospace Engineering Dept., METU

Prof. Dr. Yusuf Özyörük \_\_\_\_\_  
Aerospace Engineering Dept., METU

Prof. Dr. Nafiz Alemdaroğlu \_\_\_\_\_  
Aerospace Engineering Dept., METU

Assoc.Prof.Dr. Sinan Eyi \_\_\_\_\_  
Aerospace Engineering Dept., METU

H.Özgür Demir, M.Sc. \_\_\_\_\_  
Senior Expert Engineer, ASELSAN

**Date:** \_\_\_\_\_  
29.01.2010

**I hereby declare that all information in this document has been obtained and presented in accordance with academic rules and ethical conduct. I also declare that, as required by these rules and conduct, I have fully cited and referenced all material and results that are not original to this work.**

Name, Surname: Yusuf Okan PEKEL

Signature:

# ABSTRACT

## TRAJECTORY COMPUTATION OF SMALL SOLID PARTICLES RELEASED AND CARRIED BY FLOWFIELDS OF HELICOPTERS IN FORWARD FLIGHT

Pekel, Yusuf Okan

M. Sc., Department of Aerospace Engineering

Supervisor : Prof. Dr. Yusuf Özyörük

Co-Supervisor : Prof. Dr. Nafiz Alemdaroğlu

January 2010, 127 pages

In this thesis, trajectory computations of chaff particles ejected from a medium weight utility helicopter are performed using computational fluid dynamics. Since these chaff particles are ejected from a helicopter and carried by its flow field, it is necessary to compute and include the effects of the helicopter flow field in general and engine hot gases, main and tail rotor wakes in particular. The commercial code FLUENT is used for flow field and trajectory computations. Both main rotor and tail rotor are simulated by the so-called Virtual Blade Model in a transient fashion. Flows through the engine inlets and exhausts are treated via appropriate boundary conditions in the analysis. The generic ROBIN geometry is studied first in order to assess the accuracy of the Virtual Blade Model and various turbulence models. The computational solutions related to the ROBIN geometry are validated against the available experimental data. Flowfield and trajectory computations of chaff particles are done at a forward flight condition at which certain flight data and chaff trajectory data were acquired by ASELSAN, Inc. In the flight test, three successive chaff decoy ejections were conducted, and the chaff cloud distributions were recorded by two high-speed cameras positioned on two different locations on the helicopter.

Numerical calculations employ the post-processed camera recordings for setting the initial distributions of the chaff particles. Then, the computational results related to the chaff particle trajectories are validated by comparing to the recorded transient chaff cloud distributions from the ASEL SAN flight test. For post-processing of the recorded chaff distributions, an experimental analysis commercial code called TrackEye is used. It is found that the numerical simulations capture the trends of chaff particle distributions reasonably well.

**Keywords:** Helicopter, CFD, Chaff, Discrete Phase Model, Fluent.

# ÖZ

## KÜÇÜK KATI PARÇACIKLARIN DÜZ UÇUŞTAKİ HELİKOPTERDEN ATILMASI VE AKIŞ ALANINDAKİ TAŞINIMIN HESAPLANMASI

Pekel, Yusuf Okan

Yüksek Lisans, Havacılık ve Uzay Mühendisliği Bölümü

Tez Yöneticisi : Prof. Dr. Yusuf Özyörük

Ortak Tez Yöneticisi : Prof. Dr. Nafiz Alemdaroğlu

Ocak 2010, 127 sayfa

Bu çalışmada, orta kapasiteli bir genel maksat helikopterinden atılan chaff parçacığının izlediği yörünge, hesaplamalı akışlar dinamiği (HAD) yöntemleri kullanılarak çözülmüştür. Bu chaff parçacıklarının helikopterden atılmasından ve helikopterin akış alanı içinde taşınmasından dolayı, helikopterin akış alanının etkisinin ve motordan kaynaklı sıcak gaz, ana rotor ve kuyruk rotorundan kaynaklı ard izi etkilerinin hesaplanması ve analizlere dahil edilmesi gerekmektedir. Akış alanı ve yörünge hesaplamalarında ticari bir kod olan FLUENT yazılımı kullanılmıştır. Hem ana rotor hem de kuyruk rotoru Sanal Pal Modeli ile zamana bağlı bir şekilde modellenmiştir. Motora giren ve çıkan hava analizlerde uygun sınır şartları kullanılarak çözülmüştür. İlk etapta hem Sanal Pal Modelinin hem de farklı türbülans modellerinin çözüm yaklaşımlarının doğruluk derecelerini anlayabilmek için genel bir helikopter modeli olan ROBIN geometrisi kullanılmıştır. ROBIN geometrisi ile ilgili hesaplamalı sonuçların doğrulama işlemi mevcut olan deneysel veriler kullanılarak yapılmıştır. Akış alanı ve chaff parçacıklarının yörünge hesaplamaları, uçuş test verisinin ve chaff parçacıklarının yörünge verilerinin toplandığı düz uçuş hızında gerçekleştirilmiştir. Uçuş testlerinde, üç ardışık chaff mühimmat atışı

gerçekleştirilmiş ve chaff bulut dağılımları helikopter üzerinde iki farklı yere yerleştirilen iki hızlı kamera ile kayıt altına alınmıştır. Sayısal hesaplamalarda chaff mühimmatının ilk dağılımı için hızlı kamera görüntüleri kullanılmıştır. Chaff mühimmatının yörüngesinin hesaplaması ile ilgili sayısal sonuçlar, ASELSAN tarafından gerçekleştirilen uçuş testleri sırasında toplanan zamana bağlı chaff bulut dağılımı verisi ile kıyaslanarak doğrulanmıştır. Chaff parçacık dağılımlarının ön işleme sırasında deneysel analizlerde ticari bir kod olan TrackEye yazılımı kullanılmıştır. Sayısal simülasyonların chaff parçacık dağılımını oldukça iyi seviyede yakaladığı bulunmuştur.

**Anahtar kelimeler:** Helikopter, HAD (Hesaplamalı Akışkanlar Dinamiği), Chaff, Ayrık Faz Modeli, Fluent.

To my family  
To my love

## ACKNOWLEDGEMENTS

I would like to express my sincere gratitude to Prof. Dr. Yusuf Özyörük and Prof. Dr. Nafiz Alemdarođlu for guiding this work. I want to state my special thanks to Prof. Dr. Yusuf Özyörük for his supervision, encouragement and patience during all steps in this work. I would also like to thank all committee members.

I owe my gratitude to Özgür Demir and Vahit Özveren for encouraging me to start my master thesis about this kind of topic, their guidance and friendship.

I wish to state my endless thanks to Sevinç Fahri for giving me a chance to collect flight test data and for her support. I would also like to thank Muharrem Arık for helping me in flight tests and image processing stages. I thank Zeynep Ece Gürsoy for her support and friendships.

Thanks to my family, my wife and my close friends for their endless support throughout my life.

I would also like to thank ASELSAN, Inc for providing the necessary software and hardware.

# TABLE OF CONTENTS

ABSTRACT.....	iv
ÖZ.....	vi
ACKNOWLEDGEMENTS.....	ix
TABLE OF CONTENTS.....	x
LIST OF TABLES.....	xiii
LIST OF FIGURES.....	xiv
LIST OF SYMBOLS.....	xxi
CHAPTER	
1. INTRODUCTION.....	1
1.1    OBJECTIVE OF THE THESIS.....	1
1.2    BACKGROUND.....	1
1.2.1    USE OF CHAFF AS COUNTERMEASURE.....	1
1.2.2    HELICOPTERS.....	5
1.3    LITERATURE REVIEW.....	8
1.4    SCOPE OF THE THESIS.....	11
2. THEORETICAL BACKGROUND.....	12
2.1    ROTOR THEORIES.....	12
2.2    PARTICLE DISPERSION METHOD.....	22
3. FLIGHT TESTS AND CHAFF CLOUD RECONSTRUCTION.....	23
3.1    INSTRUMENTATION AND DATA LOGGING.....	23

3.2	CHAFF CLOUD GENERATION.....	26
3.2.1	FIRST FIRING.....	30
3.2.2	SECOND FIRING.....	36
3.2.3	THIRD FIRING .....	43
4.	NUMERICAL METHOD AND FLOW SOLVER.....	51
4.1	FLUENT.....	51
4.2	GOVERNING EQUATIONS.....	52
4.3	TURBULENCE MODELING .....	53
4.4	BOUNDARY CONDITIONS .....	54
4.5	DISCRETIZATION.....	55
4.6	VIRTUAL BLADE MODEL .....	57
4.7	DISCRETE PHASE MODEL.....	60
4.8	PARTICLE MOTION THEORY .....	61
4.8.1	EQUATIONS OF MOTION FOR PARTICLES.....	61
4.8.2	TURBULENT DISPERSION OF PARTICLES .....	63
4.8.3	TRAJECTORY CALCULATIONS .....	63
4.8.4	DPM INITIAL CONDITIONS.....	65
4.9	COMPUTATIONAL GRID GENERATION.....	67
5.	FLOW SOLVER VALIDATION TEST CASE.....	75
5.1	OVERVIEW .....	75
5.2	ROBIN VALIDATION TEST CASES .....	76
5.3	MESH GENERATION.....	77
5.4	TURBULENCE MODELS USED.....	80
5.5	RESULTS AND DISCUSSION.....	81

6. RESULTS AND COMPARISON TO FLIGHT TESTS .....	93
6.1 ANALYSES OF FIRST FIRING .....	99
6.1.1 INITIAL SURFACE I AND UNIFORM PARTICLE VELOCITY.....	99
6.1.2 INITIAL SURFACE II AND LINEARLY VARYING PARTICLE VELOCITY .....	102
6.2 ANALYSES OF SECOND FIRING .....	105
6.2.1 INITIAL SURFACE I AND UNIFORM PARTICLE VELOCITY.....	105
6.2.2 INITIAL SURFACE II AND LINEARLY VARYING PARTICLE VELOCITY .....	108
6.2.3 INITIAL SURFACE III AND LINEARLY VARYING PARTICLE VELOCITY .....	111
6.3 ANALYSES OF THIRD FIRING .....	114
6.3.1 INITIAL SURFACE I AND UNIFORM PARTICLE VELOCITY.....	115
6.3.2 INITIAL SURFACE II AND LINEARLY VARYING PARTICLE VELOCITY .....	117
6.4 MASS AND TIME STEP INDEPENDENCY .....	120
7. CONCLUSION AND FUTURE WORK.....	122
REFERENCES .....	124

## LIST OF TABLES

### TABLES

Table 1- General Characteristics of Chaff Decoy [2].....	5
Table 2-Boundary Layer Properties .....	71
Table 3-Mesh Size .....	74
Table 4-Mesh Skewness.....	74
Table 5-Model Geometry [9] .....	76
Table 6-Dimensions of the Computational Domain.....	78
Table 7-Table of Cases.....	80

# LIST OF FIGURES

## FIGURES

Figure 1- Chaff Material Example [1] .....	2
Figure 2- Chaff used as an Self Protection [1] .....	3
Figure 3- Chaff used as Chaff Corridor [1] .....	4
Figure 4 - Flow around a helicopter in a forward flight [3] .....	6
Figure 5 - Chaff Dipole Spiral Motion [12] .....	10
Figure 6- Distribution of Velocity Normal to the Blades on a Rotor at Hover [15].....	13
Figure 7- Distribution of Velocity Normal to the Blades on a Rotor at Forward Flight [15] .....	13
Figure 8- Rotor Wakes At Hover [16] .....	15
Figure 9- Tip Vortex of a Blade [16] .....	15
Figure 10- Rotor Wakes At Forward Velocity [17] .....	15
Figure 11- Momentum theory for Hover [15] .....	16
Figure 12- Momentum Theory for a Forward Flight [15] .....	18
Figure 13- Velocities and Angles Definition at Blade Element [15] .....	19
Figure 14- Phantom V4.2 Camera [20] .....	23
Figure 15-Target Positions on Helicopter Fuselage (Tail Boom) .....	25
Figure 16- Snapshot Of An Image Processing Step .....	28
Figure 17-Boundary Lines of Particle Cloud, First Firing, Isometric View ...	30
Figure 18-Boundary Lines of Particle Cloud, First Firing, Isometric View ...	31
Figure 19-Boundary Lines of Particle Cloud, First Firing, Isometric View ...	31
Figure 20-Boundary Lines of Particle Cloud, First Firing, Top View.....	32
Figure 21-Boundary Lines of Particle Cloud, First Firing, Rear View .....	32
Figure 22- Trajectory of First Firing Data .....	33
Figure 23- Splices at All Time Steps .....	33
Figure 24- Geometry of The Chaff Cloud.....	34

Figure 25- Cross Section of First Fired Chaff Cloud At Specified Time Steps.....	34
Figure 26- Evolution of Particle Cloud from First Firing .....	35
Figure 27-Boundary Lines of Particle Cloud, Second Firing, Isometric View.....	37
Figure 28-Boundary Lines of Particle Cloud, Second Firing, Isometric View.....	37
Figure 29-Boundary Lines of Particle Cloud, Second Firing, Isometric View.....	38
Figure 30-Boundary Lines of Particle Cloud, Second Firing, Side View .....	38
Figure 31-Boundary Lines of Particle Cloud, Second Firing, Top View .....	39
Figure 32-Boundary Lines of Particle Cloud, Second Firing, Rear View .....	39
Figure 33- Trajectory of First Firing Data .....	40
Figure 34- Splices at All Time Steps.....	40
Figure 35- Geometry of The Chaff Cloud.....	41
Figure 36- Cross Section of Second Fired Chaff Cloud At Specified Time Steps.....	41
Figure 37- Evolution of Particle Cloud from Second Firing .....	42
Figure 38-Boundary Lines of Particle Cloud, Third Firing, Isometric View ..	44
Figure 39-Boundary Lines of Particle Cloud, Third Firing, Isometric View ..	44
Figure 40-Boundary Lines of Particle Cloud, Third Firing, Isometric View ..	45
Figure 41-Boundary Lines of Particle Cloud, Third Firing, Top View, .....	45
Figure 42-Boundary Lines of Particle Cloud, Third Firing, Side View .....	46
Figure 43-Boundary Lines of Particle Cloud, Third Firing, Rear View .....	46
Figure 44- Trajectory of First Firing Data .....	47
Figure 45- Splices at All Time Steps.....	47
Figure 46- Geometry of The Chaff Cloud.....	48
Figure 47- Cross Section of Third Fired Chaff Cloud At Specified Time Steps.....	48
Figure 48- Evolution of Particle Cloud from Third Firing .....	49
Figure 49- Coupled Discrete Phase Calculation Procedure [24].....	64

Figure 50- Mass, Momentum and Heat Transfer [24] .....	64
Figure 51-Surface Injection [24].....	66
Figure 52-File Injection Type [24] .....	67
Figure 53-Fuselage and Tail Boom Mesh Distribution. ....	69
Figure 54 -Boundary Layer Thickness .....	70
Figure 55- Distributed Boundary Layer Thickness .....	71
Figure 56-Main and Tail Rotor Mesh Distributions.....	72
Figure 57- Flow Domain Mesh.....	73
Figure 58- Flow Domain Mesh Around Experimental Data.....	74
Figure 59- Model of ROBIN in wind tunnel [10].....	77
Figure 60- Computational Domain for ROBIN analyses .....	78
Figure 61- Main rotor mesh (actuator disk).....	78
Figure 62- Computational domain around the helicopter with boundary layer.....	79
Figure 63- Boundary layers around the ROBIN geometry .....	80
Figure 64- Value of pressure coefficient on geometry obtained from various turbulence models at $\mu = 0.15$ .....	81
Figure 65- Value of Pressure on surface at $Y=0$ m at $\mu = 0.15$ .....	82
Figure 66- Body shear stress lines for ROBIN geometry .....	83
Figure 67- Pressure orifices located on ROBIN body .....	85
Figure 68-Comparison between test data and pressure coefficient on ROBIN surface at $X/L=0.0517$ .....	85
Figure 69-Comparison between test data and pressure coefficient on ROBIN surface at $X/L=0.0941$ .....	86
Figure 70-Comparison between test data and pressure coefficient on ROBIN surface at $X/L=0.1451$ .....	86
Figure 71- Comparison between test data and pressure coefficient on ROBIN surface at $X/L=0.2007$ .....	87
Figure 72-Comparison between test data and pressure coefficient on ROBIN surface at $X/L=0.2562$ .....	87

Figure 73- Comparison between test data and pressure coefficient on ROBIN surface at $X/L=0.3074$ .....	88
Figure 74- Comparison between test data and pressure coefficient on ROBIN surface at $X/L=0.3498$ .....	88
Figure 75- Comparison between test data and pressure coefficient on ROBIN surface at $X/L=0.4669$ .....	89
Figure 76- Comparison between test data and pressure coefficient on ROBIN surface at $X/L=0.6003$ .....	89
Figure 77- Comparison between test data and pressure coefficient on ROBIN surface at $X/L=0.8809$ .....	90
Figure 78- Comparison between test data and pressure coefficient on ROBIN surface at $X/L=1.0008$ .....	90
Figure 79- Comparison between test data and pressure coefficient on ROBIN surface at $X/L=1.1619$ .....	91
Figure 80- Comparison between test data and pressure coefficient on ROBIN surface at $X/L=1.3455$ .....	91
Figure 81- Comparison between test data and pressure coefficient on ROBIN surface at $X/L=1.5305$ .....	92
Figure 82- Model that gives closest results to test data at different faces at $\mu = 0.15$ .....	92
Figure 83- Example of particle tracked locations (viewed from flow direction).....	94
Figure 84- Locations used during interpolation (viewed from flow direction).....	95
Figure 85- Helicopter model with main and tail rotor.....	97
Figure 86- Flow around a helicopter geometry .....	97
Figure 87- Main and tail rotor interactions.....	97
Figure 88- Main rotor streamlines and tip effect, forward view.....	98
Figure 89- Main rotor streamlines and tip effect, rear view .....	98
Figure 90- Trajectory analysis of first firing from initial surface at 100ms, isometric view .....	100

Figure 91- Trajectory analysis of first firing from initial surface at 100ms, rear view .....	101
Figure 92- Trajectory analysis of first firing from initial surface at 100ms, top view.....	101
Figure 93- Trajectory analysis of first firing from initial surface at 100ms, side view .....	101
Figure 94- Streamlines from initial surface at 100ms, side view .....	102
Figure 95- Particle velocity distribution at initial surface (288ms) .....	102
Figure 96- Comparison of trajectory analysis between two initial surfaces, isometric view .....	103
Figure 97- Comparison of trajectory analysis between two initial surfaces, rear view .....	104
Figure 98- Comparison of trajectory analysis between two initial surfaces, top view.....	104
Figure 99- Comparison of trajectory analysis between two initial surfaces, side view.....	104
Figure 100- Streamlines from two initial surfaces, side view.....	104
Figure 101- Trajectory analysis of second firing from initial surface at 110ms, isometric view.....	106
Figure 102- Trajectory analysis of second firing from initial surface at 110ms, rear view .....	107
Figure 103- Trajectory analysis of second firing from initial surface at 110ms, top view .....	107
Figure 104- Trajectory analysis of second firing from initial surface at 110ms, top view .....	107
Figure 105- Streamlines from initial surface at 110ms, side view .....	108
Figure 106- Particle velocity distribution at initial surface (178ms) .....	108
Figure 107- Trajectory analysis of second firing from initial surface at 178ms, isometric view.....	109
Figure 108- Trajectory analysis of second firing from initial surface at 178ms, rear view .....	110

Figure 109 Trajectory analysis of second firing from initial surface at 178ms, top view.....	110
Figure 110- Trajectory analysis of second firing from initial surface at 178ms, sideview .....	110
Figure 111- Streamlines from initial surface at 178ms, side view .....	111
Figure 112- Particle velocity distribution at initial surface (245ms) .....	111
Figure 113- Comparison of trajectory analysis between three initial surfaces, isometric view .....	113
Figure 114- Comparison of trajectory analysis between three initial surfaces, rear view .....	113
Figure 115- Comparison of trajectory analysis between three initial surfaces, top view.....	114
Figure 116- Comparison of trajectory analysis between three initial surfaces, side view .....	114
Figure 117- Streamlines from three initial surfaces, side view .....	114
Figure 118- Trajectory analysis of third firing from initial surface at 100ms, isometric view .....	116
Figure 119- Trajectory analysis of third firing from initial surface at 100ms, rear view .....	116
Figure 120- Trajectory analysis of third firing from initial surface at 100ms, top view.....	116
Figure 121- Trajectory analysis of third firing from initial surface at 100ms, side view .....	117
Figure 122- Streamlines from initial surface at 100ms, isometric view.....	117
Figure 123- Particle velocity distribution at initial surface (200ms) .....	118
Figure 124- Comparison of trajectory analysis between two initial surfaces, isometric view .....	119
Figure 125- Comparison of trajectory analysis between three initial surfaces, rear view .....	119
Figure 126- Comparison of trajectory analysis between three initial surfaces, top view.....	120

Figure 127- Comparison of trajectory analysis between three initial surfaces,  
side view ..... 120  
Figure 128- Mass dependency on trajectory analysis, isometric view ..... 121

## LIST OF SYMBOLS

$\psi$	Azimuth angle
$\dot{m}$	Mass flow rate
$v_i$	Induced velocity
$C_T$	Thrust coefficient
$C_P$	Power coefficient
$C_Q$	Torque coefficient
$c$	Blade chord
$R$	Blade radius
$N_b$	Number of blade at rotor
$\lambda$	Inflow ratio
$\mu$	Advance ratio
$D$	Drag force
$L$	Lift force
$T$	Thrust
$C_l$	Sectional lift
$C_d$	Sectional drag
$\theta$	Pitch angle
$\phi$	Inflow angle
$\alpha_r$	Tip Path Plane angle
$\alpha$	Local angle of attack
$\omega$	Angular velocity
$u$	Fluid phase velocity
$u_p$	Particle velocity
$\mu$	Molecular velocity
$\rho$	Fluid density

$\rho_p$  Particle density  
 $d_p$  Particle diameter  
Re Reynolds number

Other parameters are clearly defined wherever applicable.

# **CHAPTER 1**

## **INTRODUCTION**

### **1.1 OBJECTIVE OF THE THESIS**

One goal of this thesis is to find a suitable turbulence model for simulation of flows around helicopter geometries. For this purpose, the experimental test geometry called ROBIN is employed. The second goal, after determining a suitable turbulence model, is to perform numerical simulations of chaff distributions ejected from a helicopter which were experimentally measured during a flight test conducted by ASELSAN, Inc. In the flight tests, the chaff particle distributions were recorded by high speed cameras. In order to provide an initial distribution to the numerical simulations as well as comparisons at later stages of chaff particle dispersion after their ejection, the recorded distributions by high speed cameras are also processed by an advanced image processing technique within the scope of the thesis.

### **1.2 BACKGROUND**

#### **1.2.1 USE OF CHAFF AS COUNTERMEASURE**

Today there exist many passive and active electromagnetic countermeasure techniques employed against military threats. Dispensing chaff material is one of passive countermeasure techniques used against radar threats. In fact, this technique was used widely even during the early stages of Second World War as a passive electromagnetic countermeasure. During the Second World War, allies used this method in forms of metallic strips in deception operations, and other forces also used these materials

during their attacks. Today chaff particles inside squib are ejected by dispensers, whereas during the Second World War these particles were dispensed manually by releasing bundles of materials. After the war, there has been a continuous progress towards this type of countermeasure. For many years, chaff has played an important role in simulations of radar and electronic countermeasure (ECM). Figure 1 shows RF chaff material as an example.



**Figure 1- Chaff Material Example [1]**

The amount of radar signal power returned from an object back to the radar characterizes radar cross section of the object (RCS). Upon ejection of chaff particles into the flow field of the flying vehicle subject to detection by enemy radar, they form a cloud, reflecting the radar waves back creating confusion between the actual target (flying vehicle) and the chaff cloud. The echo reflected from the chaff cloud depends on the number of individual dipoles in it. This echo can inactivate the locking on tracking radar or creates a false or imaginary target. Created imaginary targets close to aircraft causes missiles to deviate from aircraft toward the false target.

Furthermore, it is used to block the radar coverage area. Generally, chaff particles are used for either self-protection or to create chaff corridor which protects friendly aircraft from being detected and tracked by enemy radar. Figure 2 shows the process of using chaff as a self protection. In this figure, after the radar guided missile locks on the aircraft, the pilot ejects chaff and creates imaginary target. From this point on the missile locks on this imaginary target and deviates from the aircraft.

Figure 3 shows the usage of chaff material as a chaff cloud. Here the leading aircraft rapidly dispenses chaff to the flight corridor and so the following aircraft can go through without being detected and tracked by the enemy radar.

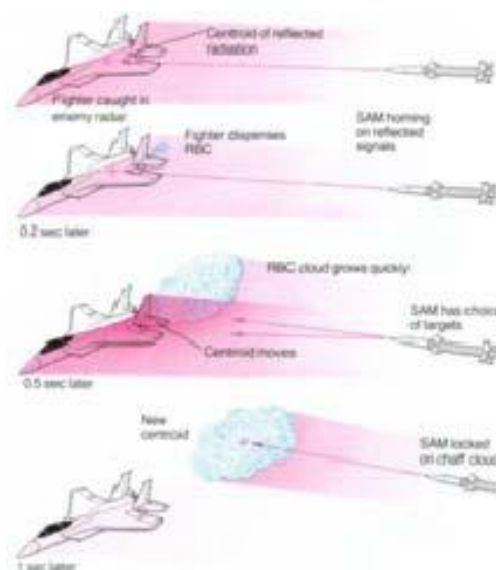
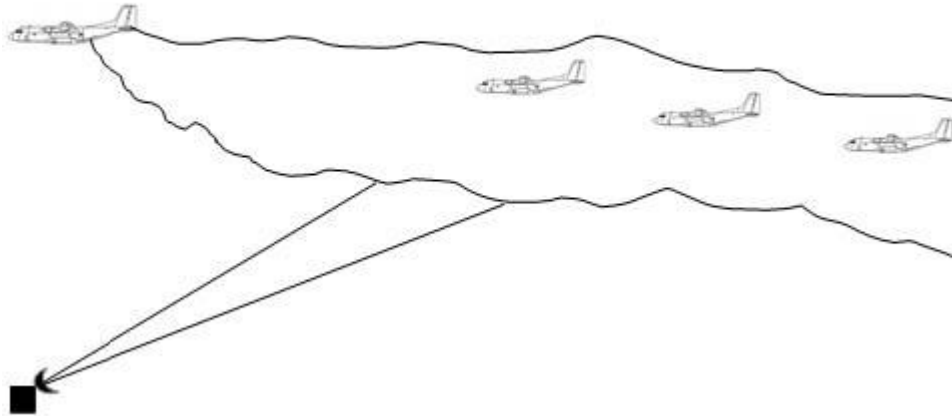


Figure 2- Chaff used as an Self Protection [1]



**Figure 3- Chaff used as Chaff Corridor [1]**

A chaff cloud is more effective when the particles in it are sufficiently distant to each other. When the particles are close to each other, the electrical coupling occurs that lowers reflection of the radar signals. Furthermore, the so-called birdnesting effect sticks particles together, and therefore, they could not behave as an individual dipole. This also affects the chaff performance. In addition to this, the birdnesting effect slows the growth of chaff cloud and limits the maximum radar cross section of the cloud. There are many parameters influencing the chaff cloud scattering, These can be listed as;

- Chaff type
- Chaff length
- Location of dispensers
- Type of dispensers
- Type, size and speed of an aircraft
- Weather
- Birdnesting

Chaff particles have fibrous structure. For increasing their effectiveness and coverage of wider frequency bands, resonant dipoles in large numbers

and at several different lengths are packaged into a small cartridge which is ejected from a dispenser. Generally chaff fibers have approximately the thickness of an human hair which is about 25 microns in diameter and ranges in length from 0.3 to 2.5 cm [2]. The weight of chaff material in a cartridge is approximately 100 gr and generally cartridge consists of about 5.5 million dipoles in it [2]. The size of a chaff cartridge is generally about 20x2.5x2.5 cm [2]. The fibers are manufactured in different ways and from different materials. The standard material used in the production is aluminum foil. Table 1 summarizes the general characteristics of chaff decoy.

**Table 1- General Characteristics of Chaff Decoy [2]**

Characteristics of Chaff Decoy	
Size	20x2.5x2.5 cm
Diameter of fibers	25 microns
Number Of Dipoles	5.5 million dipoles
Weight	100gr

### **1.2.2 HELICOPTERS**

Helicopter is a complicated aircraft which takes its lift from rotating blades. It has so many capabilities compared to fixed wing aircraft. They can take off and land vertically at any place. Capability for hover is the most distinguishing maneuver for this aircraft. It can hover both in ground and out of ground effect. In addition, helicopters can go sideward, backward, and forward. Drawbacks of this device are that their forward speed is slower with respect to fixed wing airplanes and also aerodynamics behavior of blades and fuselage as well as mechanism of rotary system makes helicopters complicated.



Forward flight velocity also changes the aerodynamic behavior of the blades. Each spanwise section of blades encounters different flow speeds. At the tip of blades this speed can reach as high as a Mach number of about 0.7. As the forward velocity increases, tip velocity of the blades at advancing side increases. Depending on the degree of forward velocity, the flow around there may enter the transonic region. Whereas the blades on the retreating side face lower flow velocities. To compensate the deficiency in velocity, blades on this side are pitched to higher angles. The angles of attack in some region on the retreating side may even be excessive to cause stall of the blades there. Due to these different velocities and blade pitches (or angles of attack), an unbalanced lift distribution over the blades results. This phenomenon in turn causes blades to bend and creates some aeroelastic problems.

Some other phenomena regarding the aerodynamic complexity of flow around the helicopter is due to the separated flows from the hub and pylon. The separated flows interact with the tail rotor and control surfaces.

The level of unsteadiness with the separated flow from helicopter geometry (fuselage) increases with increasing forward velocity. At hover condition induced flow from the main rotor dominates. One of the effects of this unsteady separation causes changes in the angles of attack of the blades, resulting in vibration and changes in response. Furthermore, the main rotor and fuselage interactions are the main causes of fatigue, drag, and control problems.

Because of all these complexities, accurate prediction of flow field around a helicopter is quite difficult. These interactions can be evaluated best in wind tunnel tests. However, since wind tunnel test method is very expensive and time consuming, computational fluid dynamic (CFD) serves as an alternative tool.

### 1.3 LITERATURE REVIEW

In order to understand the behavior of flowfield around a helicopter, many wind tunnel tests were carried out. Many CFD solutions were also realized by different groups. In the CFD analyses, generally rotor and fuselage interactions were examined.

Regarding the chaff particles, motional behavior and aerodynamic characteristics of individual chaff dipoles were investigated in laboratories. Using the experimental results, empirical models were developed to be used in simulations.

As pointed out earlier, the interaction between the rotor and fuselage is the most complicated part. Modeling this phenomena accurately plays an important role for successful solutions. O'Brien [4], [5] made a study to understand the effect of rotor modeling on rotor/fuselage interactions. In his study a constant actuator disk, varying actuator disk, and a blade element actuator disk were considered. When solutions were compared with the experimental test results, the blade element actuator disk results with the actual blade airfoil parameters found to yield the best fit to the measured data. RENAUD [6] made a study about the capabilities and weaknesses of CFD codes on the fuselage performance and rotor-fuselage interaction. Effects of grid density, turbulence models and compressibility were investigated on an isolated fuselage and a fuselage combined with a uniform and non-uniform actuator disk. His study indicated that for an isolated fuselage, pressure and forces are almost insensitive to the choice of one or two-equation turbulence models, and also uniform actuator disk model could not efficiently model rotor/fuselage interaction. A non-uniform actuator disk model gave better results. Ramasamy [3] investigated the physical structure and the evolution of blade tip vortices and rotation effects on turbulent structures by a set of model-scale hovering experiments and a

mathematical model containing Navier-Stokes equations. Hall [7] also studied wakes and tip vortex flowfields. This study investigated the use of high-order, unsteady computational fluid dynamics for the simulations of wake and vortex dominated flows.

Ruith [8] used the Virtual Blade Model (VBM) in FLUENT solver as a method for analyzing the mutual aerodynamic interactions between multiple rotors and fuselage. For validating this technique, a single rotor airframe interaction case in forward flight was considered. Obtained pressure distributions from the model were compared with the experimental data, and it was concluded that the VBM model gives close results to the experimental data when the rotor is assumed to operate at the conditions matching the experimental thrust and moment values.

Freeman and Mineck [9] made a wind tunnel test on the ROBIN (ROTOR Body Interaction) geometry in order to obtain surface pressure which could be used for validation of analytic models. Mineck [10] then made a numerical study comparing unstructured and structured grid results with experimental data. Numerical solutions were obtained through a Navier Stokes solver. The numerical results from the unstructured grid were in accordance with the structured grid and close to the experimental pressure coefficients.

Berry et al. [11] also used the ROBIN geometry to compare various aerodynamic methods at low speed flight conditions.

Brunk et al. [12] made several drop tests with thirteen distinct chaff dipole configurations in a special enclosed test chamber in order to obtain their aerodynamic characteristics. Multi image motion photographs were taken during the tests to follow the dipole motions and trajectories. Also this technique was used to obtain aerodynamic forces and moment coefficients

for each dipole configuration. The obtained data from tests were used in simulation programs afterwards. According to the tests, dynamic behavior of chaff particles strictly depends on their principal cross-sectional dimensions. Dipoles which have cross sections less or equal to 0.008 inches exhibit a singular characteristic with spiraling motion shown in Figure 5.

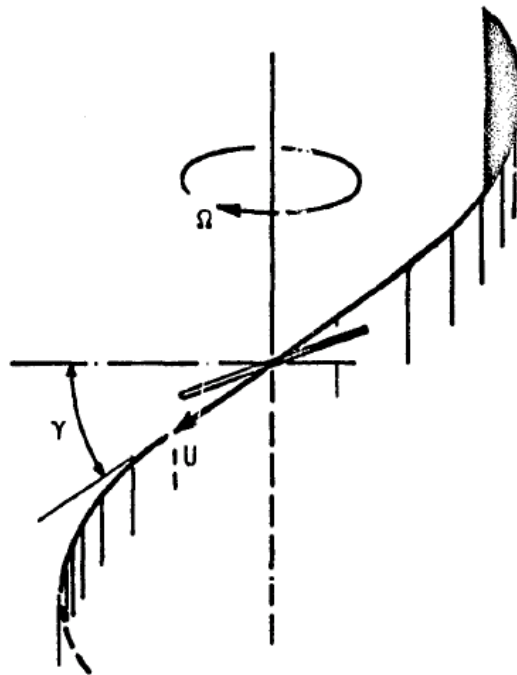


Figure 5 - Chaff Dipole Spiral Motion [12]

Fray [13] developed a computer algorithm to generate correlated random processes for simulating time-varying samples of chaff cloud radar sections. Arnott et al. [14] worked on determining a radar cross section distribution function correlated to the fall speed and concentration in the atmosphere by using the NEXRAD radar.

## **1.4 SCOPE OF THE THESIS**

In this thesis, flow around a medium weight utility helicopter including ejected chaff particles was computed using CFD at 100 knots in order to understand the behavior of these particles and to improve particle trajectory calculation techniques. The flight test data presented in this thesis were obtained by a high speed camera and interpreted after image processing. Chaff cloud generation and radar cross sections were created by modeling the data obtained during flight tests.

The numerical solutions were obtained by using a commercial CFD code FLUENT with discrete phase model incorporating the modeling of particles. Furthermore the main and the tail rotor of an helicopter were modeled by an user defined function, namely virtual blade model.

In the first chapter of the thesis, some background information about the chaff particles and flow around a helicopter geometry are given. In addition, the objective and the scope are presented. In Chapter 2, some theoretical background relating to this study are mentioned. In this chapter, basics of an rotor aerodynamics including the momentum theory and blade element theory, besides discrete phase particle theory are given. In Chapter 3, flight test and instrumentation are described as an entry to this chapter. Then, image processing technique and results follow. Moreover, reconstruction of obtained data, generation chaff cloud technique and radar cross sections for chaff cloud are mentioned. In Chapter 4, the numerical method and flow solver that are used during the analysis are described. Besides, computational grid generation and boundary conditions are mentioned in that chapter. Validation of rotor module and flow solver analyses are described in Chapter 5. Results of cases are presented and discussed in Chapter 6. Lastly Chapter 7 involves concluding remarks and future work.

## CHAPTER 2

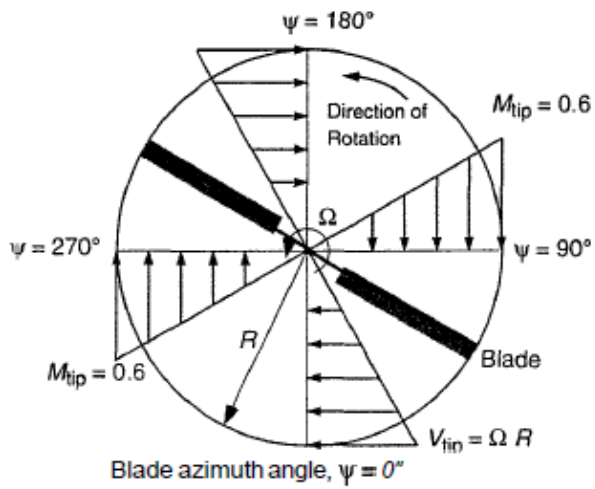
### THEORETICAL BACKGROUND

#### 2.1 ROTOR THEORIES

The rotor is the main part of a helicopter when considering its functions. It creates vertical lift in order to balance the weight of the helicopter. Furthermore, forward flight and maneuvers are attained by the propulsive forces generated by the rotor. The required power for hydraulic systems and avionics systems are also generated by the rotor mechanism. Therefore, aerodynamic characteristics of the rotor affect the entire behavior of the helicopter.

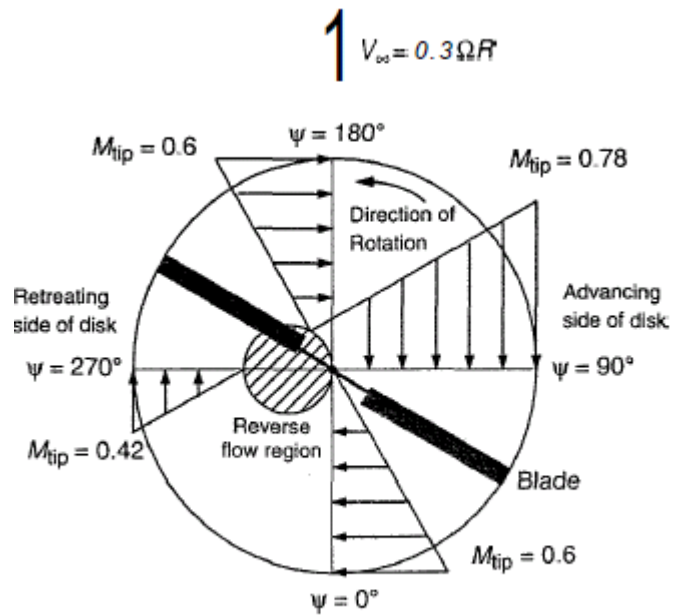
The creation of lift at rotating blades depends on the local angle of attack that blade encounters and local dynamic pressure. From a flight condition to another, pressure and velocity distributions on the blade change drastically. Besides these distributions also change from one blade azimuth angle ( $\psi$ ) to another, as well as from one radial blade section to another in a given flight condition itself. The blade angle ( $\psi$ ) is assumed equal to zero when the blade points the rearward direction of the helicopter. This identification can be seen in Figure 6.

As seen in Figure 6, normal velocity distribution to a blade at hover is azimuthally axisymmetric and radially linear. Since angular velocity varies with the radial distance, velocity at the root hub is zero. Whereas high velocity values occur at the blade tips.



(a) Hovering flight

Figure 6- Distribution of Velocity Normal to the Blades on a Rotor at Hover [15]



(b) Forward flight,  $\mu = 0.3$

Figure 7- Distribution of Velocity Normal to the Blades on a Rotor at Forward Flight [15]

In a forward flight condition, the rotor plane is tilted forward in order to overcome both the weight of the aircraft and drag. In a forward velocity case, since the free stream velocity adds or subtracts from the local blade velocity due to rotation, there no longer occurs an axisymmetric velocity distribution. Figure 7 shows the distribution of velocity normal on the rotor blades in forward flight. Although no axisymmetric distribution occurs, the normal velocity still changes linearly along the blade span. The value of velocity depends on the azimuthal location of the blade section. The highest velocity occurs at the advancing side of the blade since the forward speed adds on to the velocity due angular velocity. The lowest velocity occurs on the retreating side, because the two velocity vectors appear to be in opposite directions. The linear change in the velocity distribution causes zero velocity for some region at the retreating side. This type velocity distribution causes unbalanced lift distribution over the rotor. Because of this unbalanced distribution, rotor inherently tends to tilt.

Other very important aerodynamic features on a helicopter are related to the rotor wakes and vortices generated at the tip of the blades. Due to high dynamic pressure at the tip of the blades, strong vortices are generated from both main rotor and tail rotor blade tips. At hover condition, the rotor wakes follow a helical path downward. As discussed above the aerodynamic force loading on a blade varies almost linearly from root to tip. Figure 8 shows the rotor wake behavior and blade loading distribution at hover condition. Figure 9 shows the visualization of a tip vortex on a blade. This generated vortex causes the incoming blade to face an upwash and increased angle of attack. Lastly, Figure 10 shows the rotor wakes at forward velocity. The vortex sheet interacts with the empennage and tail rotor at this condition.

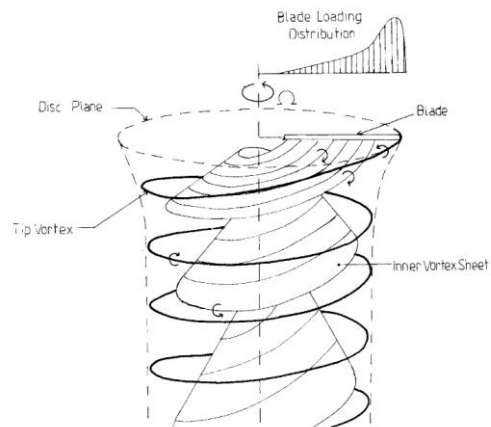


**Figure 8- Rotor Wakes At Hover [16]**

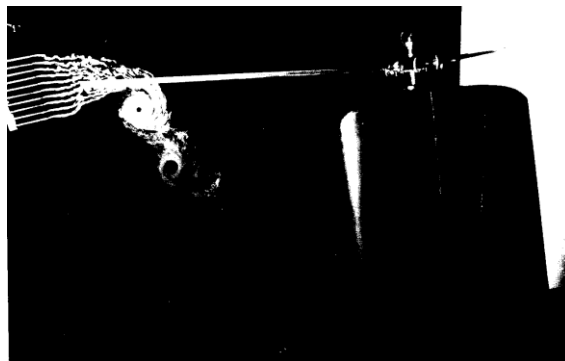


**Figure 9- Tip Vortex of a Blade [16]**

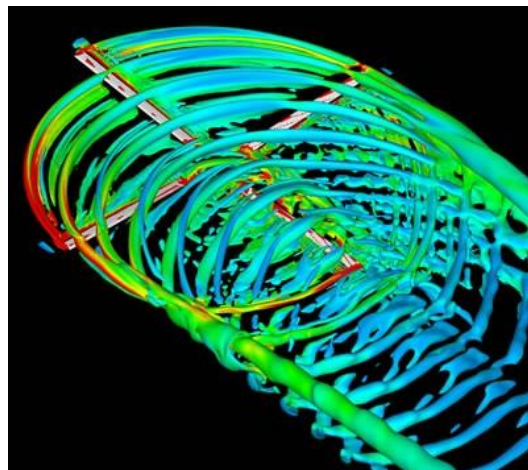


**Figure 10- Rotor Wakes At Forward Velocity [17]**

In momentum theory [15], rotor is modeled as an actuator disk which adds momentum and energy to the flow. This theory concerns with the global balance of mass, momentum and energy. Although details of the flow around blades are undervalued, it gives reasonable solutions away from the rotor. In momentum theory, flow is assumed to be incompressible, quasi-steady, inviscid and irrotational. Furthermore, it is one dimensional and flow is uniform through the rotor disk. Additionally flow around the actuator disk creates smooth slipstream. Figure 11 shows the flow characteristics for the momentum theory for hover.

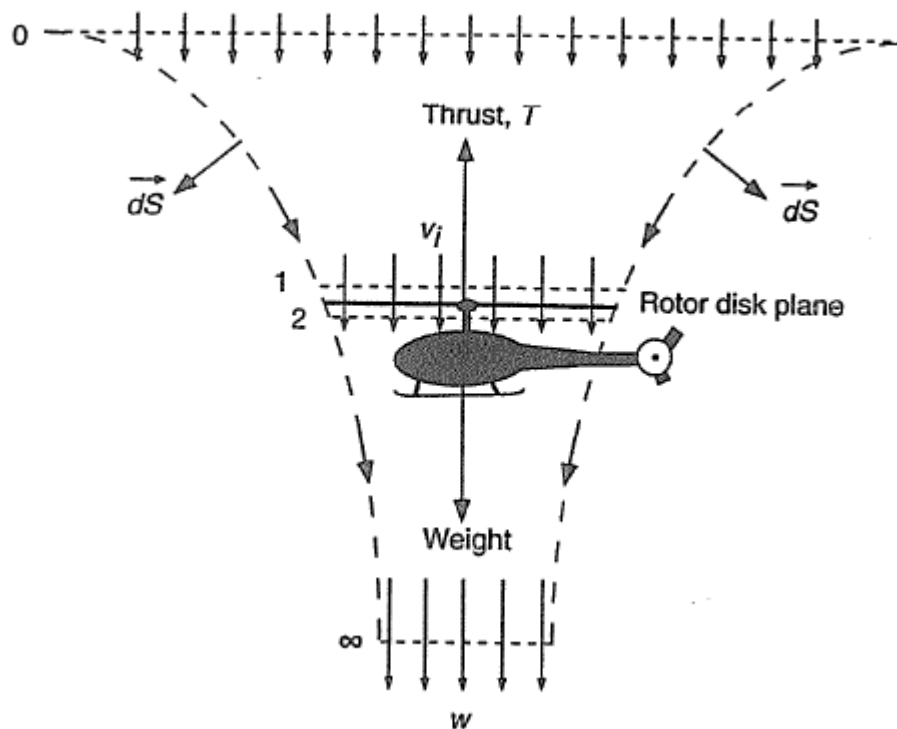


Figure 11- Momentum theory for Hover [15]

By using the quasi-steady assumption and conservation mass, mass flow rate within boundaries is defined as follows [15]

$$\dot{m} = \iint_{\infty} \rho \vec{V} \cdot d\vec{S} = \iint_2 \rho \vec{V} \cdot d\vec{S} \quad (1)$$

Thrust coefficient on rotor disk area is defined as [15]

$$C_T = \frac{T}{\rho A V_{tip}^2} = \frac{T}{\rho A \Omega^2 R^2} \quad (2)$$

Power coefficient is defined as [15]

$$C_P = \frac{P}{\rho A V_{tip}^3} = \frac{P}{\rho A \Omega^3 R^3} \quad (3)$$

Torque coefficient is defined as [15]

$$C_Q = \frac{Q}{\rho A V_{tip}^2 R} = \frac{Q}{\rho A \Omega^2 R^3} \quad (4)$$

In forward flight, the main rotor is tilted through the air since it should both compensate the weight of an helicopter and drag, as shown in Figure 12. This figure shows the flow characteristics in momentum theory for forward flight.

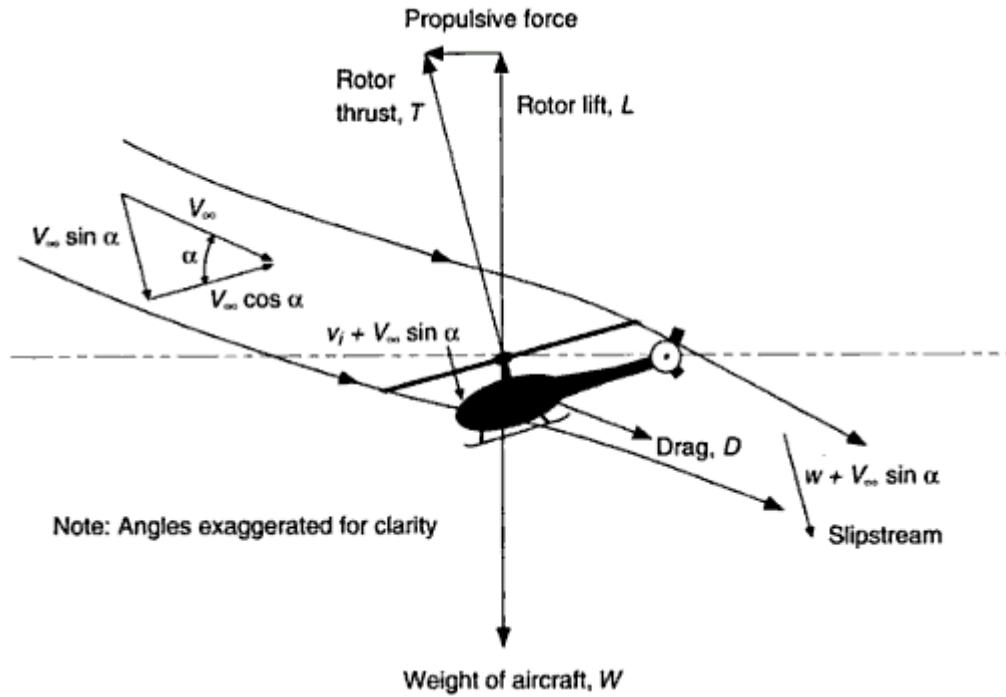


Figure 12- Momentum Theory for a Forward Flight [15]

As in the hover case, mass flow rate through the disk is given by [15]

$$\dot{m} = \rho AU$$

Where  $U$  is defined as [15]

$$U = \sqrt{(V_\infty \cos \alpha)^2 + (V_\infty \sin \alpha + v_i)^2} = \sqrt{V_\infty^2 + 2V_\infty v_i \sin \alpha + v_i^2} \quad (5)$$

Thrust is obtained as follows [15]

$$T = 2\dot{m}v_i = 2\rho Av_i \sqrt{V_\infty^2 + 2V_\infty v_i \sin \alpha + v_i^2} \quad (6)$$

In the Blade Element Theory (BET) [15], each sections of the blade acts as a 2-D dimensional airfoil to produce aerodynamic forces and moments.

Moments and forces on the entire rotor can be obtained by integrating the sectional airloads over the blades. Integrating these forces for each blade element and then taking its average over a rotor revolution results in the rotor performance. In contrast to the momentum theory, BET helps designing rotor blades in terms of blade twist, planform distribution, and airfoil shape which are critical for the required thrust, torque and power characteristic. Figure 13 shows the definitions of velocities and angles used in the blade element theory.

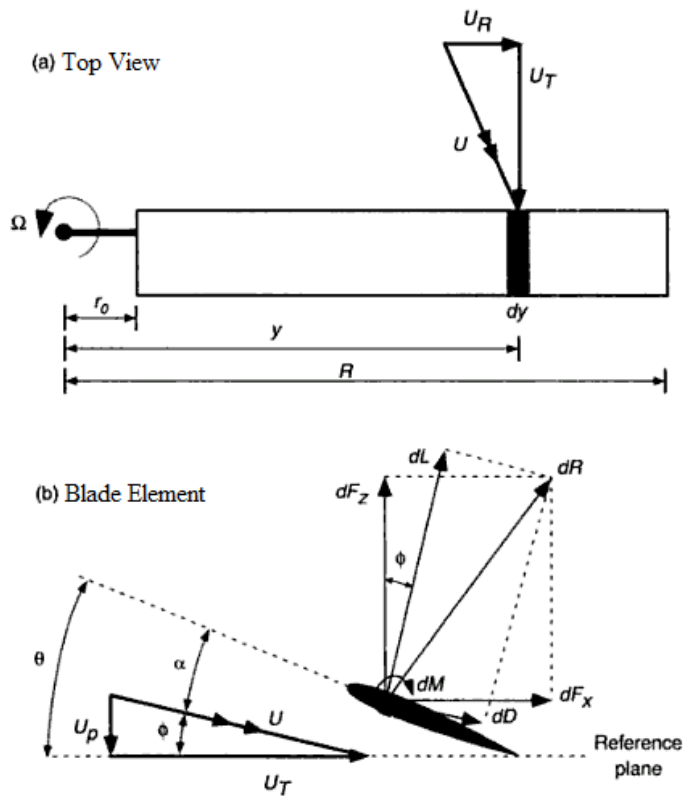


Figure 13- Velocities and Angles Definition at Blade Element [15]

The total local flow velocity at any blade section at a radial distance  $y$  from rotational axes has an out-of-plane component for hover or axial flight case

as  $U_p = V_c + v_i$  combined of climb velocity and induced inflow. For in plane component  $U_T = \Omega y$ . Therefore, the total velocity is [15]

$$U = \sqrt{U_T^2 + U_p^2} \quad (7)$$

The resultant incremental lift and drag per unit span on blade element is then [15]

$$dL = \frac{1}{2} \rho U^2 c C_l dy \quad \text{and} \quad dD = \frac{1}{2} \rho U^2 c C_d dy \quad (8)$$

where  $c$  stands for local blade chord.

The thrust coefficient is defined as [15]

$$\begin{aligned} dC_T &= \frac{N_b dL}{\rho A (\Omega R)^2} = \frac{N_b \left( \frac{1}{2} \rho U_T^2 c C_l dy \right)}{\rho (\pi R^2) (\Omega R)^2} \\ &= \frac{1}{2} \left( \frac{N_b c}{\pi R} \right) C_l \left( \frac{y}{R} \right)^2 d \left( \frac{y}{R} \right) \\ &= \frac{1}{2} \left( \frac{N_b c}{\pi R} \right) C_l r^2 dr \end{aligned} \quad (9)$$

where  $\sigma = \frac{N_b c}{\pi R}$  is defined as , then thrust coefficient gets [15]

$$dC_T = \frac{1}{2} \sigma C_l r^2 dr \quad (10)$$

Power coefficient is defined as [15]

$$\begin{aligned} dC_P = dC_Q &= \frac{dQ}{\rho A (\Omega R)^2 R} = \frac{N_b (\phi dL + dD) y}{\rho (\pi R^2) (\Omega R)^2 R} \\ &= \frac{1}{2} \left( \frac{N_b c}{\pi R} \right) (\phi C_l + C_d) r^3 dr \end{aligned}$$

$$= \frac{1}{2} \sigma (\phi C_l + C_d) r^3 dr \quad (11)$$

The total thrust and power coefficients can be found by integrating these incremental coefficients along the blade from root to tip.

In forward velocities, main rotor is tilted through airflow. Velocities are periodic and depend on the blade azimuthal position. For forward flight condition, in plane velocity have two components due to rotation and due to forward velocity. Additionally, there is a spanwise velocity component due to the forward speed factor. For out of plane velocity, it has three components as, inflow velocity, velocity caused by flapping motion and velocity due to coning.

$$r = \frac{y}{R} \text{ and } \frac{U}{\Omega R} = \frac{\Omega y}{\Omega R} = \frac{y}{R} = r \text{ are non-dimensional quantities [15].}$$

$u_T$  is the normalized velocity component.

Thrust coefficient for forward flight condition is defined as follows [16].

Assume  $U_p$  is much smaller than  $U_T$  i.e.  $U \approx U_T$

$$\begin{aligned} dC_T &= \frac{N_b dL}{\rho A (\Omega R)^2} = \frac{N_b \left( \frac{1}{2} \rho U_T^2 c C_l dy \right)}{\rho (\pi R^2) (\Omega R)^2} = \frac{1}{2} \frac{N_b c}{\pi R} \frac{U_T^2}{(\Omega R)^2} C_L d\left(\frac{y}{R}\right) \\ &= \frac{1}{2} \sigma u_T^2 C_L dr \end{aligned} \quad (12)$$

Incremental power and torque coefficients are defined as

$$\begin{aligned} dC_P = dC_Q &= \frac{dQ}{\rho A (\Omega R)^2 R} = \frac{N_b (\phi dL + dD) y}{\rho (\pi R^2) (\Omega R)^2 R} = \frac{1}{2} \left( \frac{N_b c}{\pi R} \right) (\phi C_l + C_d) u_T^2 r dr \\ &= \frac{1}{2} \sigma (\phi C_l + C_d) u_T^2 r dr \end{aligned} \quad (13)$$

## **2.2 PARTICLE DISPERSION METHOD**

As mentioned, dispersion of chaff particles in the atmosphere has a great importance regarding as a countermeasure technique for radar guided-missiles and radars. Two different approaches are used to describe this process. These are the Eulerian and Lagrangian approaches.

In the Eulerian framework, attention is given to the fluid which passes through a control volume that is fixed in space. The fluid inside the control volume at any instant in time will consist of different fluid particles from that which was there at some previous instant in time [18].

In the Lagrangian approach, attention is given to a particular mass of fluid as it flows. The principles of mass, momentum and energy conservation are then applied to this particular element of fluid as it flows, resulting in a set of conservation equations in the Lagrangian coordinates [18].

The discrete phase model (DPM) in FLUENT follows the Euler-Lagrange approach. The fluid phase is treated as a continuum by solving the time-averaged Navier-Stokes equations whereas the dispersed phase is solved by tracking a number of particles through the calculated flow field of continuous phase.

## CHAPTER 3

# FLIGHT TESTS AND CHAFF CLOUD RECONSTRUCTION

### 3.1 INSTRUMENTATION AND DATA LOGGING

Flight tests were performed on a medium weight utility helicopter by ASELSAN, Inc. The flight test profiles included forward flight at 100 knots, which is approximately the cruise speed for this helicopter. Three chaff decoys were ejected at different time intervals. The test instrumentation, data logging process and processing steps are all explained in this chapter.

The instrumentation was composed of high-speed cameras, a data acquisition system and a laptop PC. Phantom V4.2 model high-speed cameras were used in the tests. Their characteristics are given in reference [19]. Their user-friendly software operates in a Windows™ environment. Figure 14 is a picture of a Phantom V4.2 camera.



Figure 14- Phantom V4.2 Camera [20]

Since firing of a chaff decoy is a high-speed process and because of the nature of the chaff, the particles cannot be detected very easily with naked eyes and with usual cameras, high-speed camera was used. In the flight tests, Phantom V4.2 cameras were operated when firing was in action. Two high-speed cameras were used in order to get 3-D position data. Since two cameras were used, synchronization between them was important. In these tests, cameras took picture at 400Hz with a lens having 6.5mm optical focus-length. Before the flight, camera settings and display properties were set according to the atmospheric conditions in order to take good quality pictures. Also the flight direction was organized in order the quality of the pictures not to be affected by the sunshine.

The reason why two cameras were used is that from one camera view it is not possible to get 3-D positions. To be able to get 3-D positions of the particles, one additional camera was used. The essential point in placing the cameras is ; they should be located as far apart as possible with high position angle difference.

Furthermore before the test, instrumentation target points were marked on the helicopter fuselage and tail boom at different locations. These target points played the role of reference points for the data processing. The positions of the markers were chosen in such a way that both cameras viewed them properly. Otherwise the recorded pictures could not be processed accurately. Figure 15 shows the target (marker) positions on the helicopter fuselage.



**Figure 15-Target Positions on Helicopter Fuselage (Tail Boom)**

The raw data, which were composed of pictures taken by the high-speed cameras, were logged online to the PC. The acquisition interface allowed the user to see the pictures and movies during the flight. Also the user could change the display properties. A commercial code called TrackEye [21] was used as image processing software for this thesis. This software is used for motion analysis on military test ranges and automotive crash test labs. This software covers the entire process from digitizing images (film or video) through automatic tracking to a complete predefined report [22].

Typical applications are [22] :

- 2D, 3D and/or 6D motion analysis on flying objects at military test ranges. The analysis often involves images from fixed cameras as well as cameras on tracking mounts.
- 6D analysis on objects in store separation. The analysis normally involves images from cameras mounted on wing tips or under the fuselage of an aircraft.
- 2D and 3D analysis of different parts of a vehicle during a crash test in the automotive industry.

A problem arises if the cameras are not synchronized because the different camera views show the target at different times, and the target may have moved between them. The method requires that there are at least two images of the target taken at the same time. TrackEye solves this problem by interpolating the pixel coordinates to a common timebase [22].

The accuracy of the result depends on the camera geometry, i.e. the way the cameras are placed. This is especially important if only two cameras are used. The best results are obtained when the lines of sight from the cameras intersect at right angles. If they intersect at a very narrow angle the accuracy is considerably lower [22]. During the flight tests, two cameras were located with some distance from each other with different lines of sight. However, there were some geometrical limitations due to fuselage that might have caused some inaccuracies in the trajectory calculations.

The inaccuracy of a lens is called lens distortion. TrackEye uses a mathematical model of the distortion to correct the image data from the camera. The need for a calibration rises from the fact that most camera/lens systems have a number of random and systematic errors. The calibration procedure takes into account these systematic errors [22].

### **3.2 CHAFF CLOUD GENERATION**

Three firings were performed during the flight tests, so three different image processing steps should be performed. As stated before, pictures were taken at a rate of 400 Hz. This means that at the image processing step, user should control 800 pictures for two camera views in one second interval. The pictures that the user responsible for increases linearly, since three firings were done.

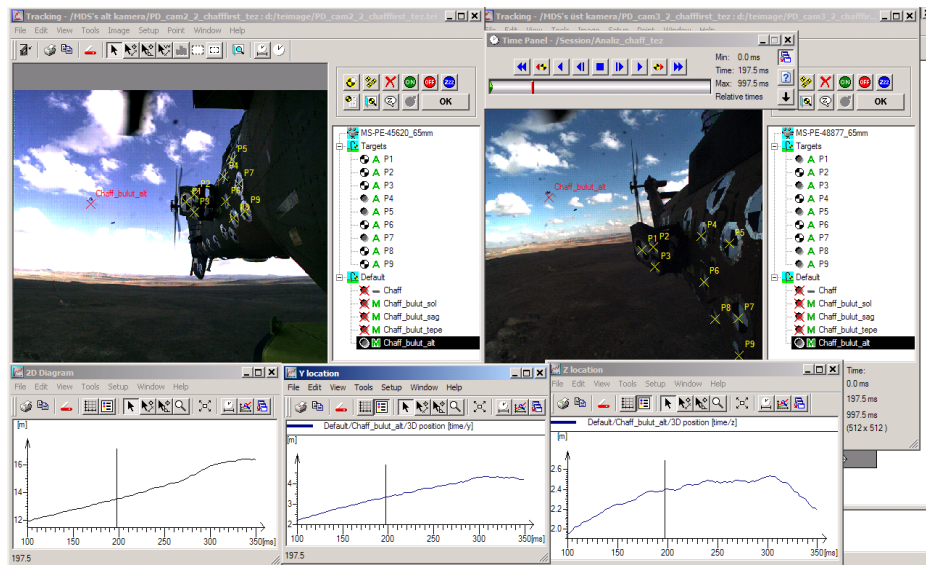
Length of camera views are not longer than one second, because as the time increases, the space for the data increase rapidly. Length of one second camera view is enough to track chaff particles because at some extend, the user cannot distinguish the chaff material from the nature itself.

Image processing starts with the recognition of the target location at the pictures. Before starting pre-processing, user should define target positions to the program. Also user can define target shapes to program, so program can track target positions automatically. Unfortunately, this recognition cannot be done for chaff material. The reason is that as the time passing, chaff geometry changes whereas recognition target geometry remains same. Hence to be able to get chaff locations user must manually track chaff positions from both camera view.

Just immediately after the firing, chaff particles disperse. During these tiny seconds, chaff particles tracked from whole center of gravity position. But when the chaff particles start to disperse, in order to be tracked accurately, at least four geometrical locations were selected. These points define the max-min's of the generated chaff dispersion. This means that the locations are ;

- Upper Boundary
- Lower Boundary
- Right Boundary
- Left Boundary

The tracking process of the initial step is called initial boundary. Figure 16 shows an example of an image processing step.



**Figure 16- Snapshot Of An Image Processing Step**

The results coming from the image processing were only the positions of the tracked locations. While plotting the obtained values, data was adjusted according to the head of helicopter fuselage. This means that the plotted data were respect to the helicopter itself. Post-processing of the results was performed in MATLAB [23].

Having determined the time evolution of the chaff distributions from the three firings, cross sectional area changes at any time step can be found easily. This is important because the numerical simulation of the flow field with chaff particles needs an initial condition (distribution) for them. Numerically calculated chaff particle positions are used to form the chaff cloud to compare with those found from the flight test firings. Several sets of numerical computations are carried out utilizing the chaff cloud cross sections from the experimentally determined distributions at different times as initial conditions to see the effects of the initial chaff positions on the computed trajectories. Understanding these effects on the simulated results is important since the birdnesting effects cannot be taken into account by

the CFD computations. This chapter also mentions steps to construct chaff cloud geometry and represents cross sectional area of the ejected chaff particles at a unique time step and evolution of particle clouds.

Since the CFD computations require initial positions and velocities of the chaff particles, constructing an initial cloud cross section (surface) with their velocity information is very important. Such surfaces with velocity information are constructed from the time evolution of the particles obtained from the high speed camera views. After post-processing with the TrackEye software, the construction of chaff cloud geometry was performed with the following steps:

1. Identify a set of outermost particles in the cloud and their positions as a function of time, and form a time series.
2. Pass linear splines through two successive positions of each particle identified in the outermost set. For these particles, the position vector change divided by the time step will be their velocity vector.
3. Also, pass splines through all the particles in the outermost set to form the outer boundary of the cloud. Assume this boundary is the circumference for a cloud section corresponding to that time, and there are particles in the average plane formed by this boundary. The velocities of these particles in the average plane is determined by interpolation.

In the end, a closed chaff particle distribution volume is created. The following sections give the results of the above procedure for all the three firings.

### 3.2.1 FIRST FIRING

Figure 17 to Figure 21 show trajectory histories of the boundary lines from the first firing. Image processing data contains the position histories of the particles which were visualized by MATLAB [23]. For initial time steps, only one boundary was tracked during the process, so only one boundary line can be seen at the post-processing plot, namely, initial boundary. It symbolizes the unseparated chaff particles. After that, the number of boundary lines increases, since the chaff particles start to separate from each other. From the histories of the trajectories, it can be understood that to some extent particles go with the initial momentum, but later the flow field around the helicopter dominates how the trajectories shape. Initially particle separation is not extensive which can be explained by the so-called birdnesting effect. The particles remain mostly bound together in early stages, and therefore, the growth of the separation is impeded.

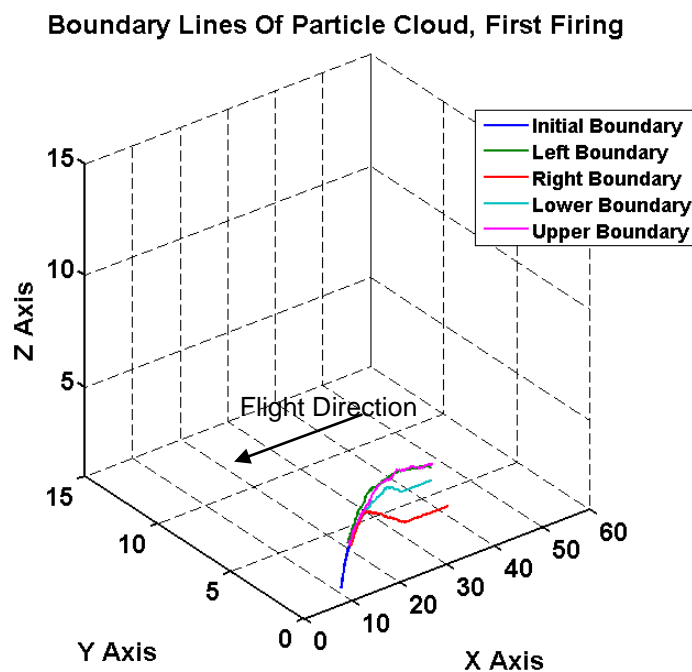


Figure 17-Boundary Lines of Particle Cloud, First Firing, Isometric View

Boundary Lines Of Particle Cloud, First Firing

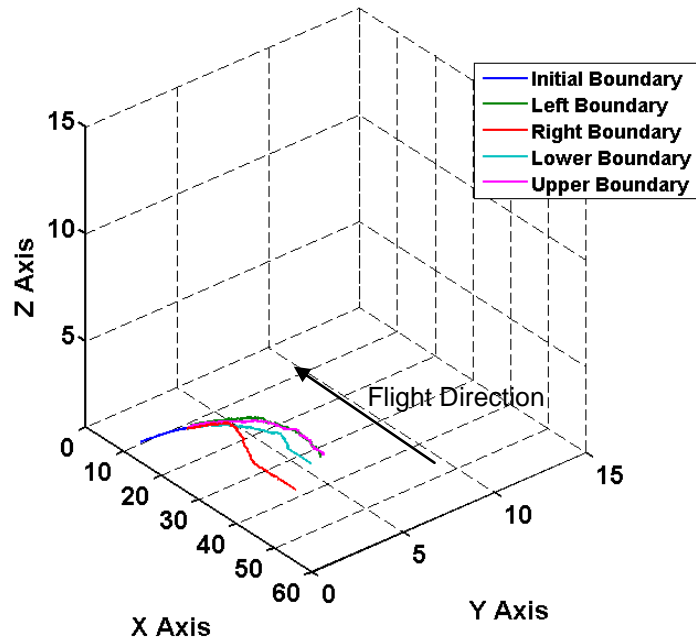


Figure 18-Boundary Lines of Particle Cloud, First Firing, Isometric View

Boundary Lines Of Particle Cloud, First Firing

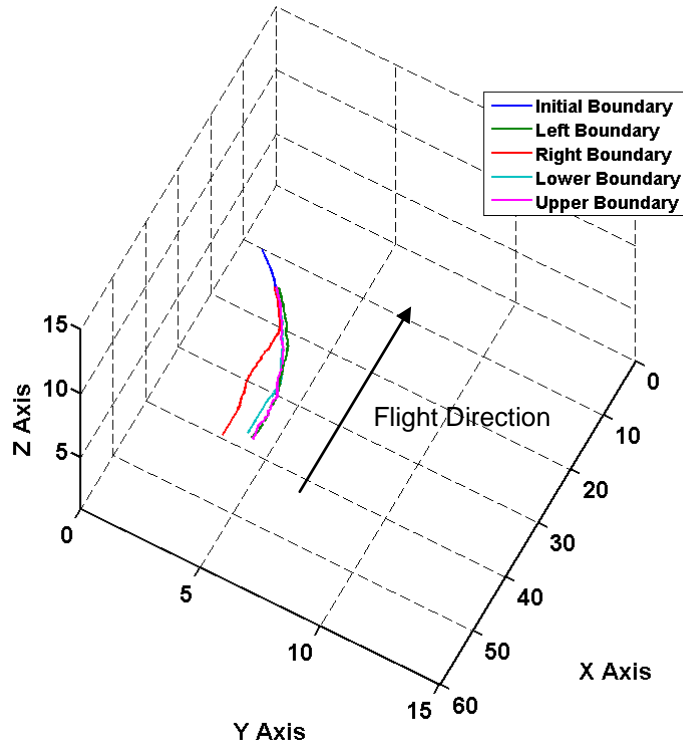


Figure 19-Boundary Lines of Particle Cloud, First Firing, Isometric View

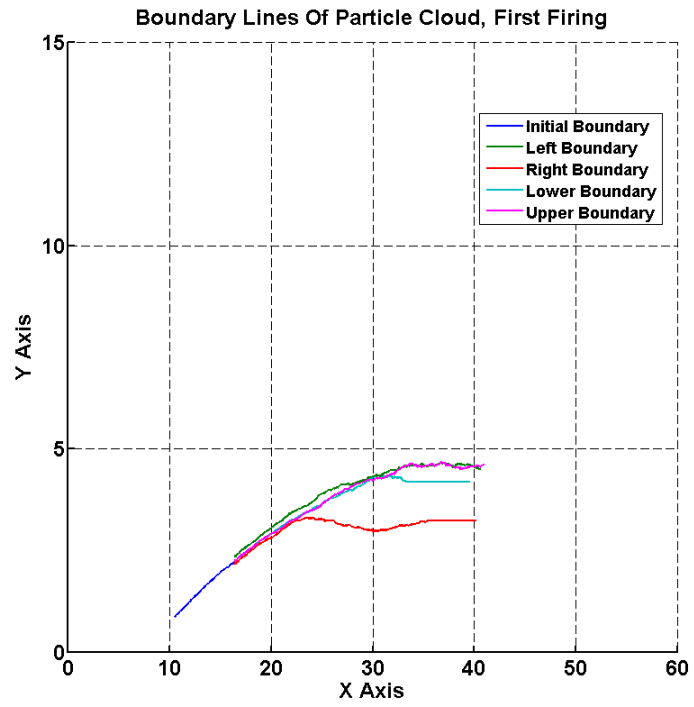


Figure 20-Boundary Lines of Particle Cloud, First Firing, Top View

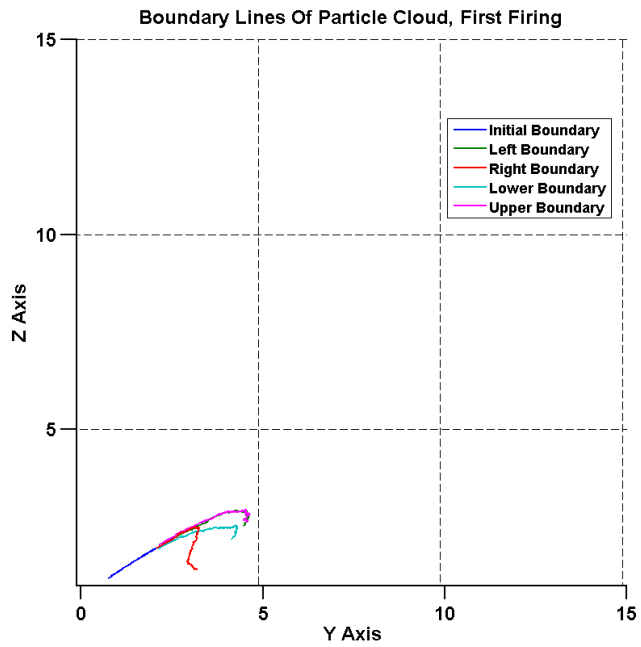
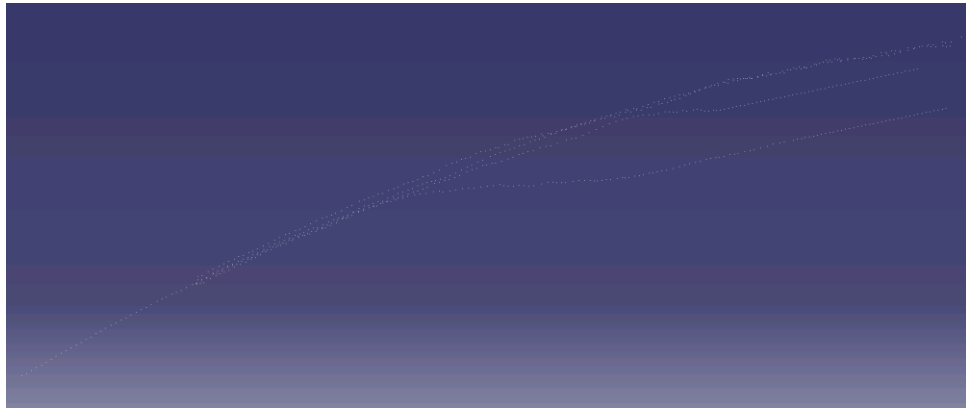
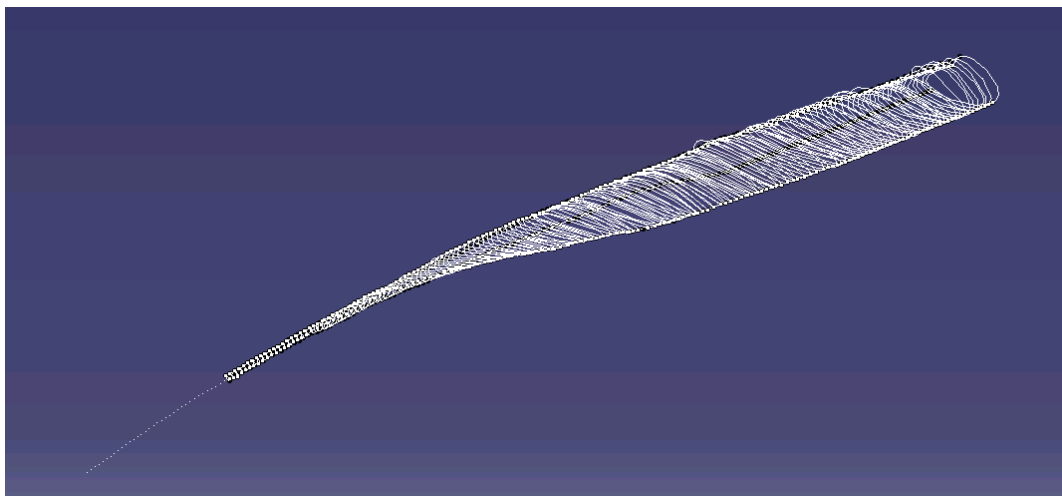


Figure 21-Boundary Lines of Particle Cloud, First Firing, Rear View

Figure 22 shows some trajectories from the first firing data. Figure 23 shows the generated outer splines for the whole data set, and lastly Figure 24 shows the constructed chaff cloud as a 3-D geometry.



**Figure 22- Trajectory of First Firing Data**



**Figure 23- Splines at All Time Steps**

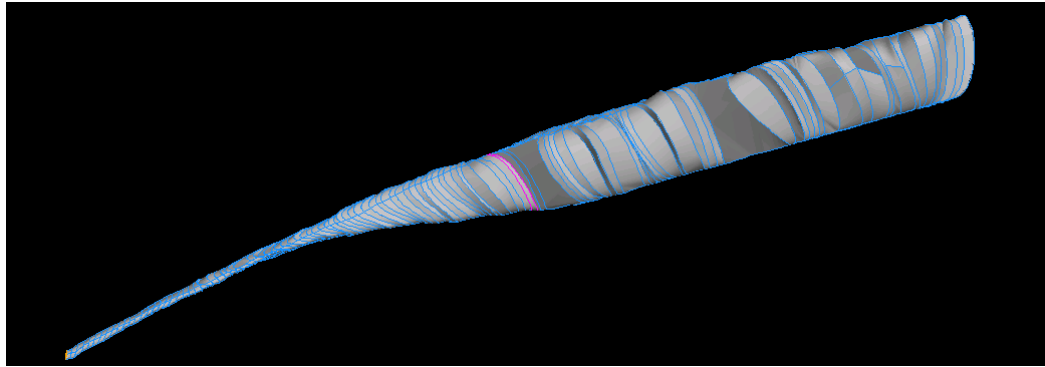


**Figure 24- Geometry of The Chaff Cloud**

The importance of constructing the chaff cloud particles also come into existence if someone seeks the cross sectional area of the ejected chaff particles at a unique time step. Cross sectional area of chaff cloud at unique time is important because it gives an idea about radar cross sectional area of this countermeasure.

Figure 25a-d, show the cross sectional areas of first generated chaff cloud at specified time intervals of 100 ms, 200 ms, 300 ms and 400 ms after the firing.

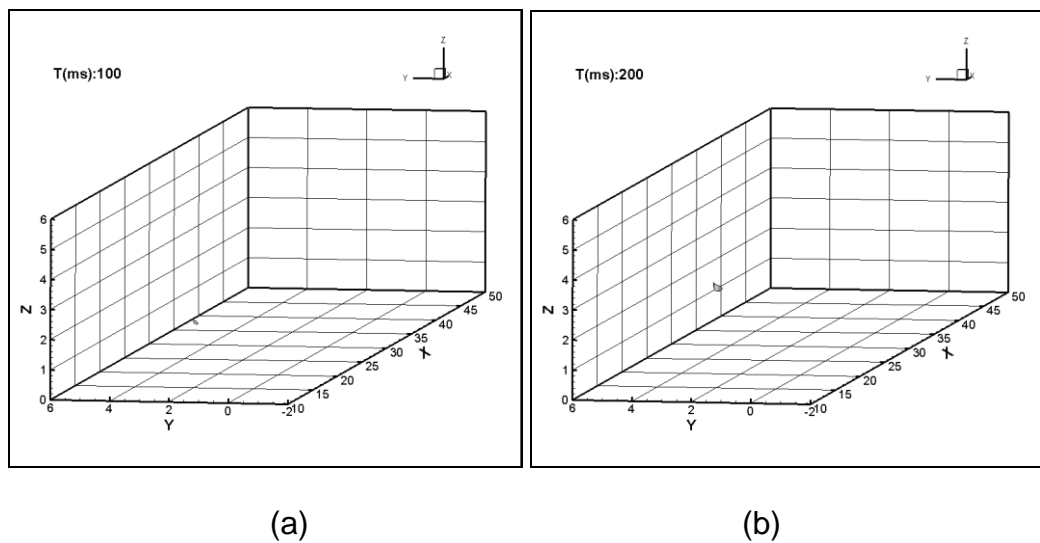


**Figure 25- Cross Section of First Fired Chaff Cloud At Specified Time Steps**

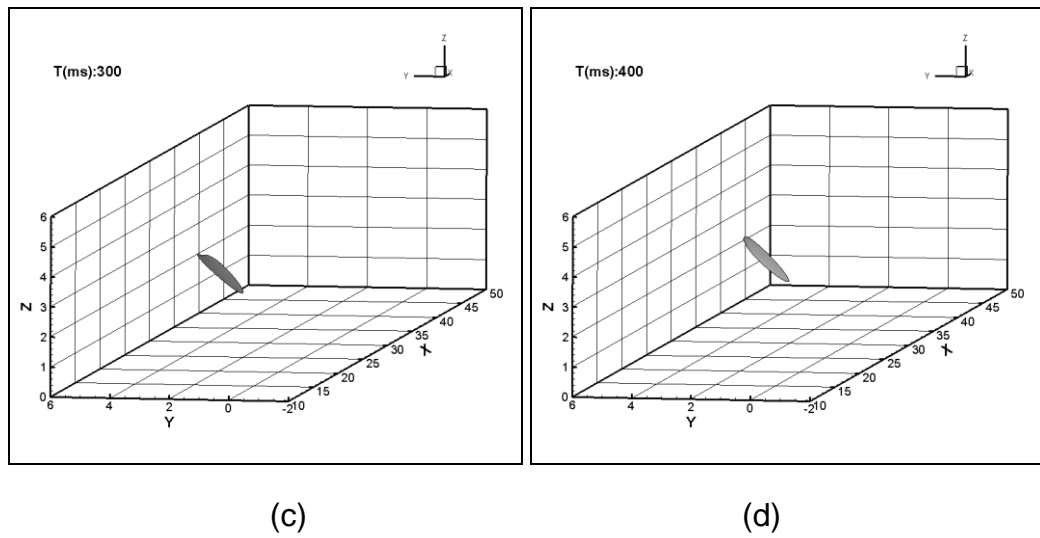


**Figure 25 (Continued)- Cross Section of First Fired Chaff Cloud At Specified Time Steps**

The eight small figures shown in Figure 26 exhibit the evolution of the particle cloud from the first firing at different periods. Up to unique time, dispersion rate is high. But after passing this time, dispersion rate starts to decrease. Why this phenomena occurs can be explained by flow around the helicopter dominates the distribution and after that particle dispersion stays with the flow characteristics.



**Figure 26- Evolution of Particle Cloud from First Firing**

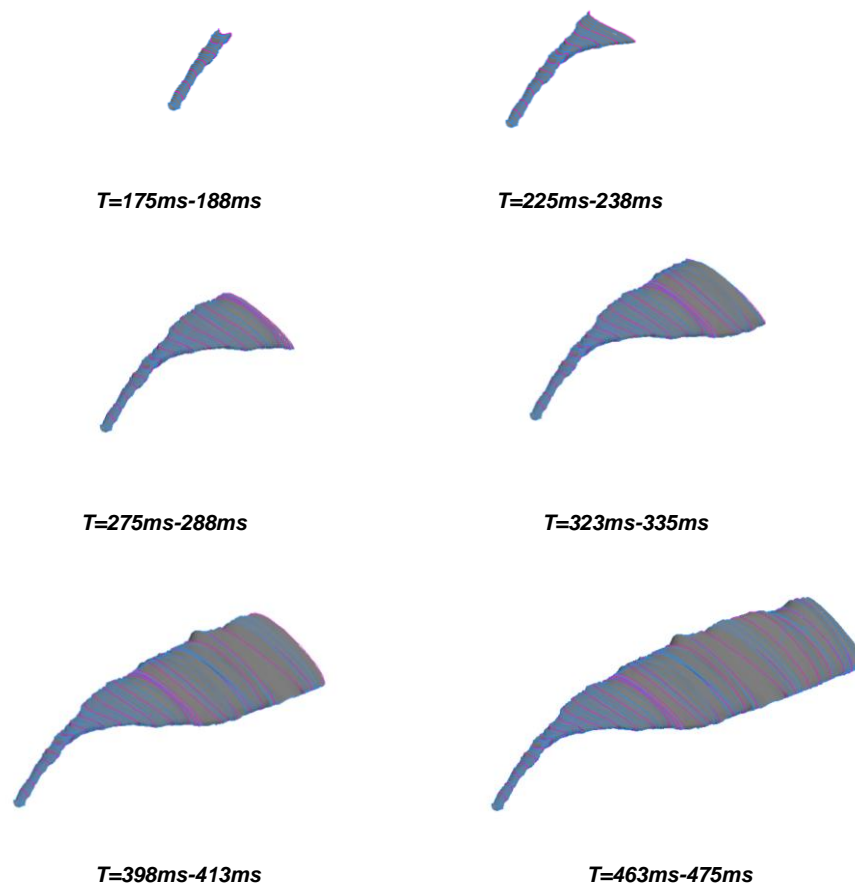


Figure 26 (Continued)-Evolution of Particle Cloud from First Firing

### 3.2.2 SECOND FIRING

Figure 27 to Figure 32 show trajectory histories of the boundary lines from the second firing. General trends look similar to those of the first firing. When examined more closely, it is observed that chaff distributions of the second firing look more uniform than the first firing. When the top-view plots are compared with each other, it can be said that the first firing chaff particles stick together for longer durations. Figure 30 shows the main rotor downwash effect on the particle trajectory. After the particles lose their initial momentum, they start to go downward with the help of main rotor downwash and partially by gravity. These firings were performed at forward

velocity of 100 knots. If these firings had been made at lower forward velocities, the particles could have gone more downward.

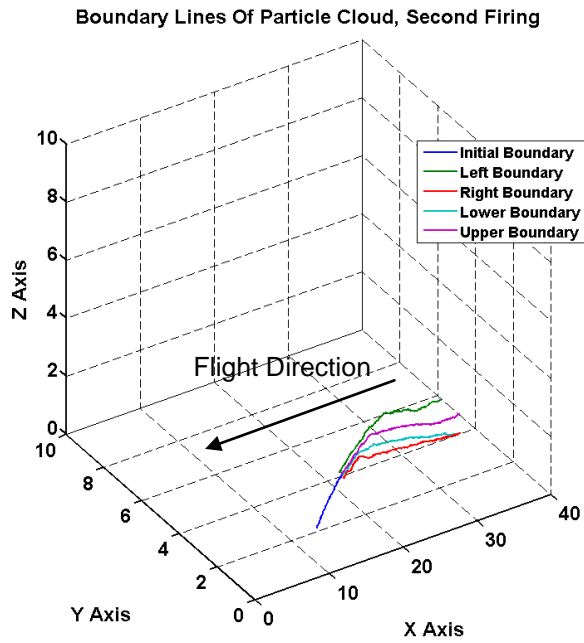


Figure 27-Boundary Lines of Particle Cloud, Second Firing, Isometric View

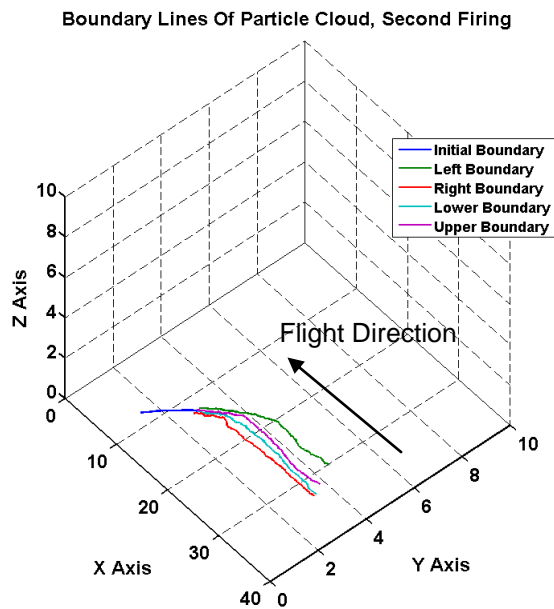
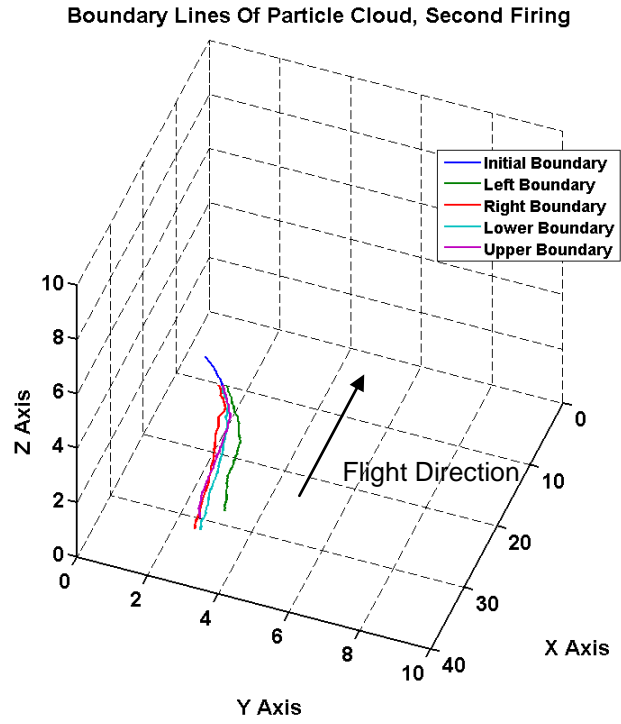
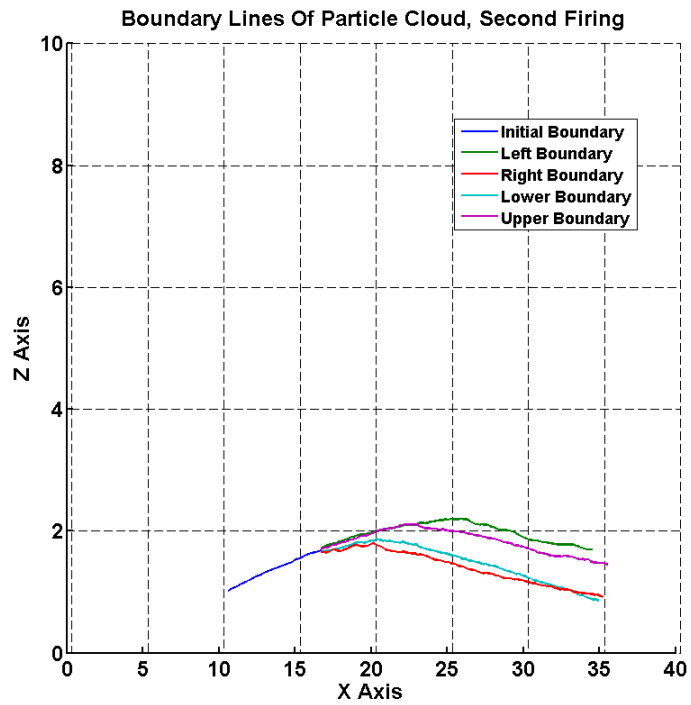


Figure 28-Boundary Lines of Particle Cloud, Second Firing, Isometric View



**Figure 29-Boundary Lines of Particle Cloud, Second Firing, Isometric View**



**Figure 30-Boundary Lines of Particle Cloud, Second Firing, Side View**

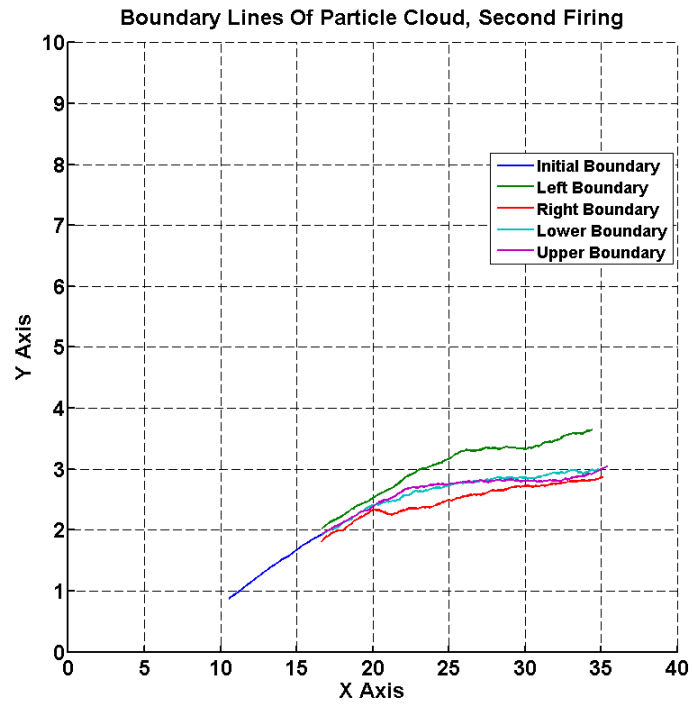


Figure 31-Boundary Lines of Particle Cloud, Second Firing, Top View

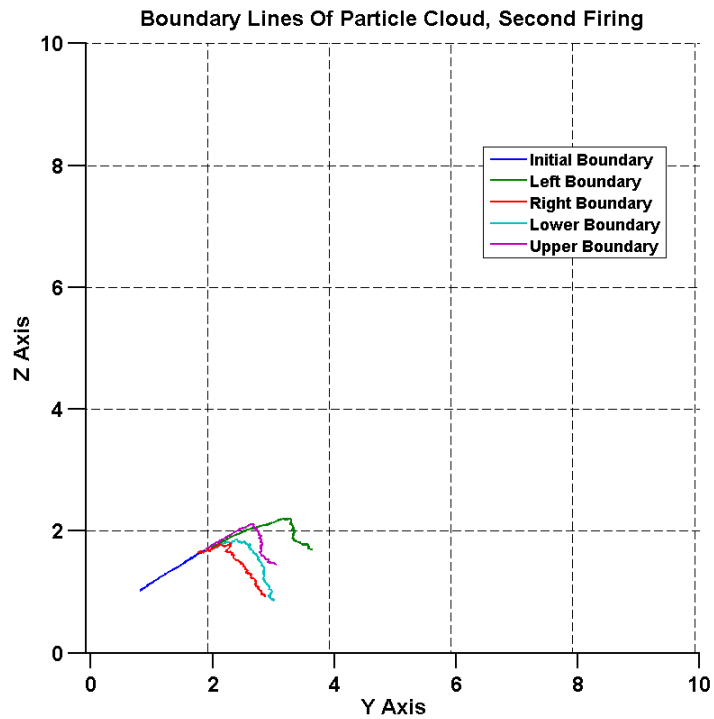
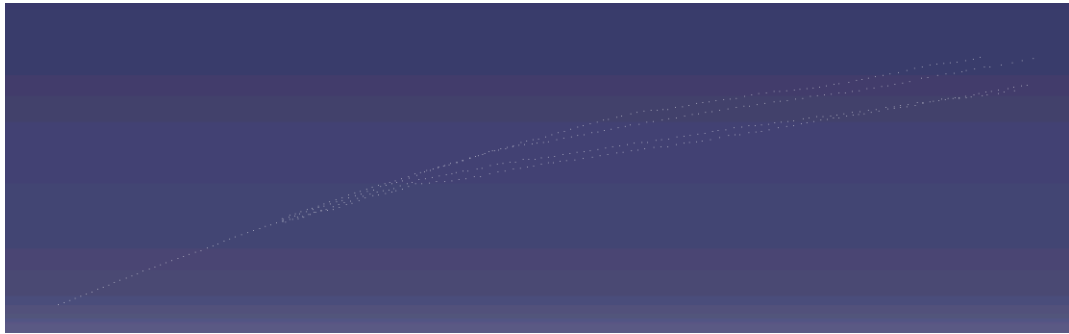
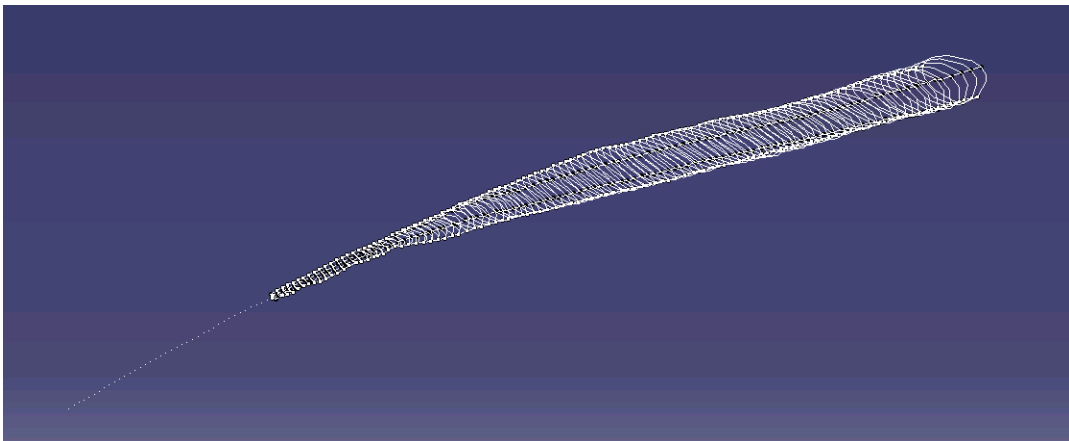


Figure 32-Boundary Lines of Particle Cloud, Second Firing, Rear View

Figure 33 shows some trajectories from the second firing data. Figure 34 shows the sequence of generated splines corresponding to the outer particles in the cloud, and lastly Figure 35 shows constructed chaff cloud as a 3-D geometry.



**Figure 33- Trajectory of First Firing Data**



**Figure 34- Splines at All Time Steps**

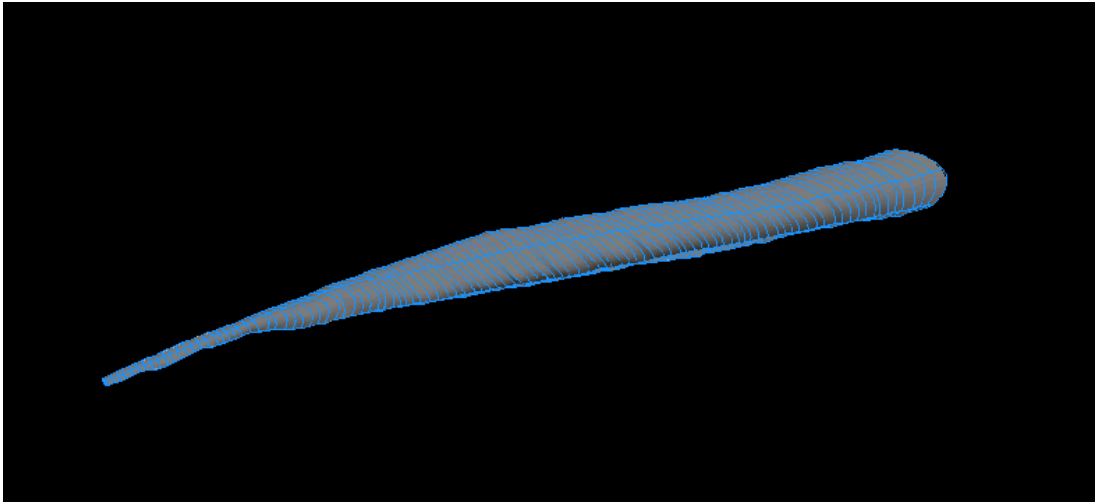
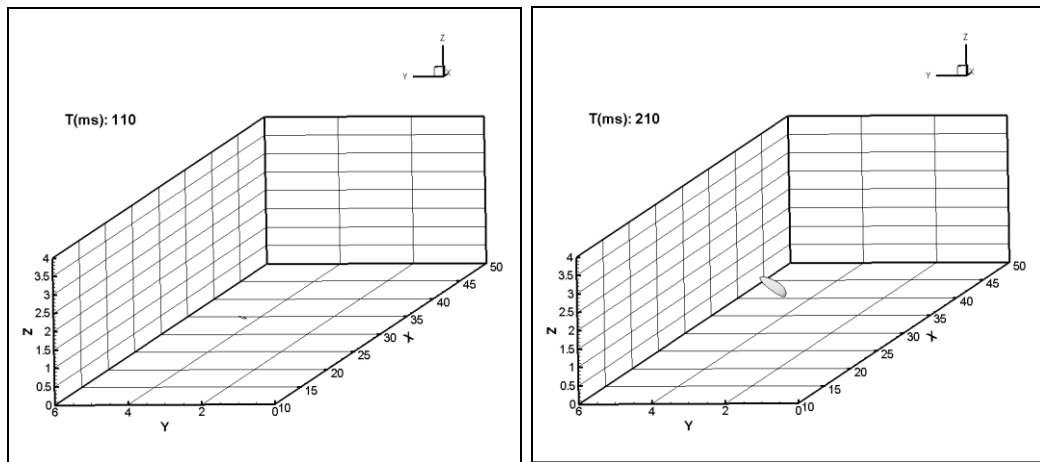


**Figure 35- Geometry of The Chaff Cloud**

Figure 36a-d show the cross sectional areas of second generated chaff cloud at specified time intervals of 110 ms, 210 ms, 310 ms and 375 ms after firing.



(a)

(b)

**Figure 36- Cross Section of Second Fired Chaff Cloud At Specified Time Steps**

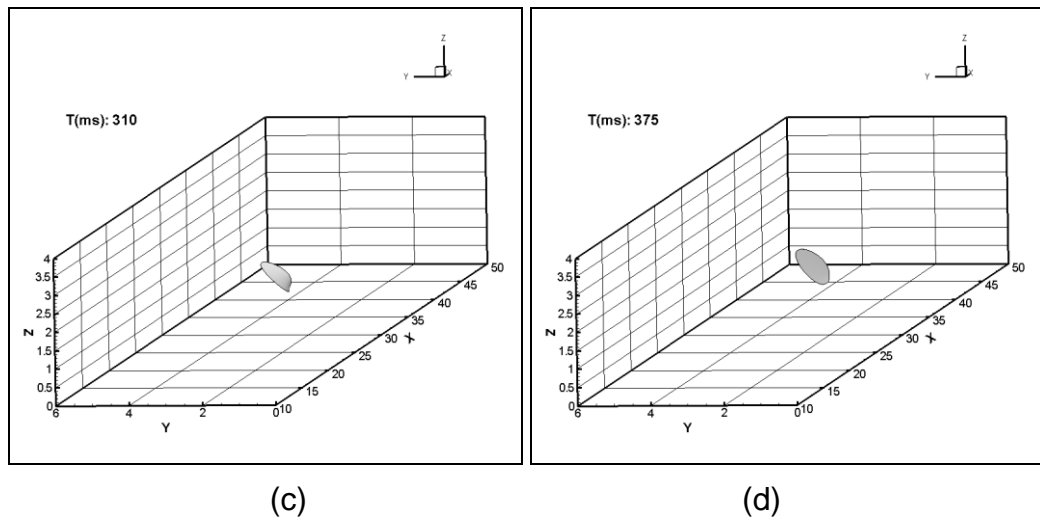


**Figure 36 (Continued)- Cross Section of Second Fired Chaff Cloud At Specified Time Steps**

The eight small figures shown in Figure 37 exhibit the evolution of the particle cloud from the second firing at different periods. In this firing, particles seem to have started dispersing at an earlier time. As a result, the dispersion rate looks somewhat different compared with that of the first firing with more uniform particle distribution. These small differences stem mainly from the birdnesting effect.



**Figure 37- Evolution of Particle Cloud from Second Firing**

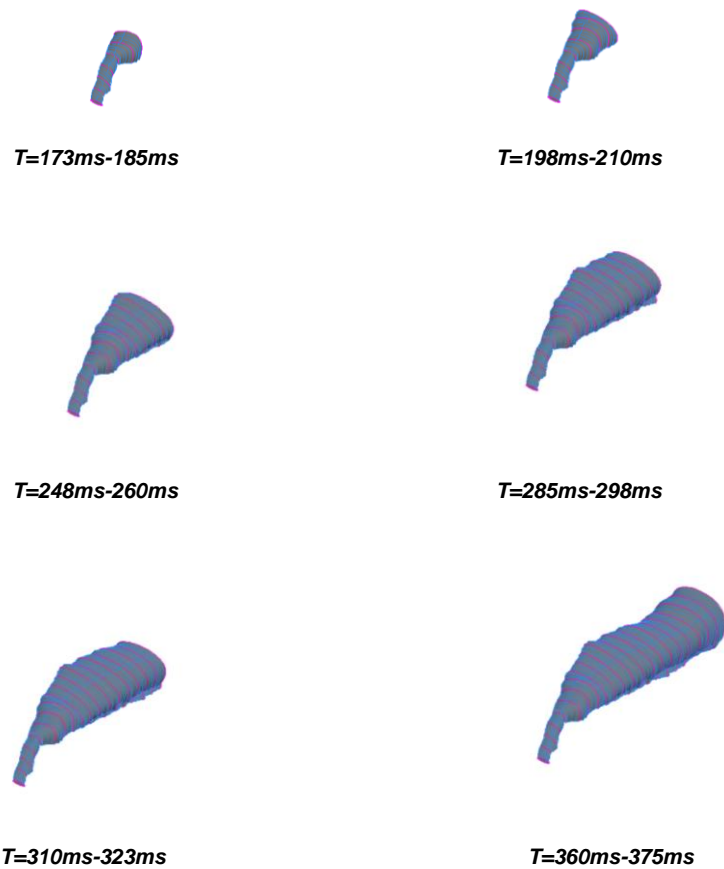
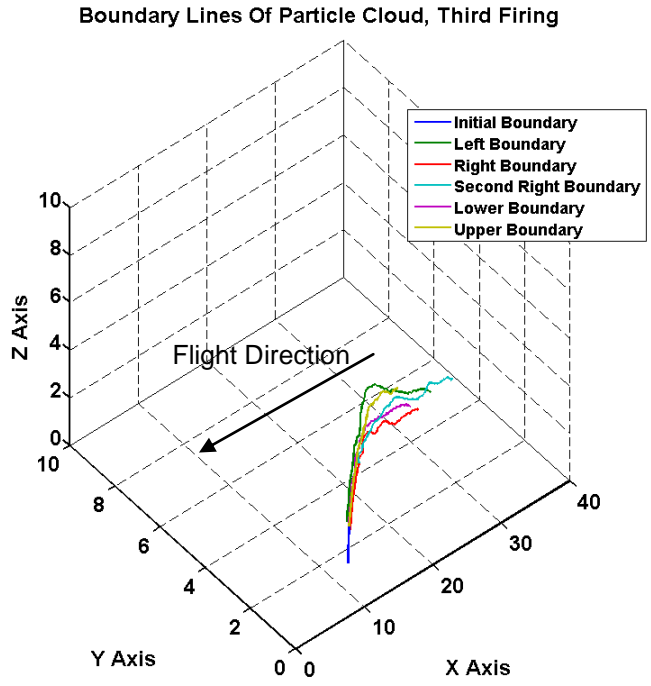


Figure 37 (Continued)-Evolution of Particle Cloud from Second Firing

### 3.2.3 THIRD FIRING

Figure 38 to Figure 43 show trajectory histories of the boundary lines from the third firing. Since the flowfield is inherently unsteady and the firings were made back to back on the same flight, the relative positions of the rotor blades during the ejections seem to have affected the trajectories of the particles relative to each other. Furthermore, during the flight test, wind direction and the wind velocity were not recorded. Therefore, there is some uncertainty in the recorded data regarding the influence by the atmospheric conditions. Despite all these, the main trends of the distributions look similar to the those of the previous firings. The effect of the main rotor downwash can also be seen on the third firing results.



**Figure 38-Boundary Lines of Particle Cloud, Third Firing, Isometric View**

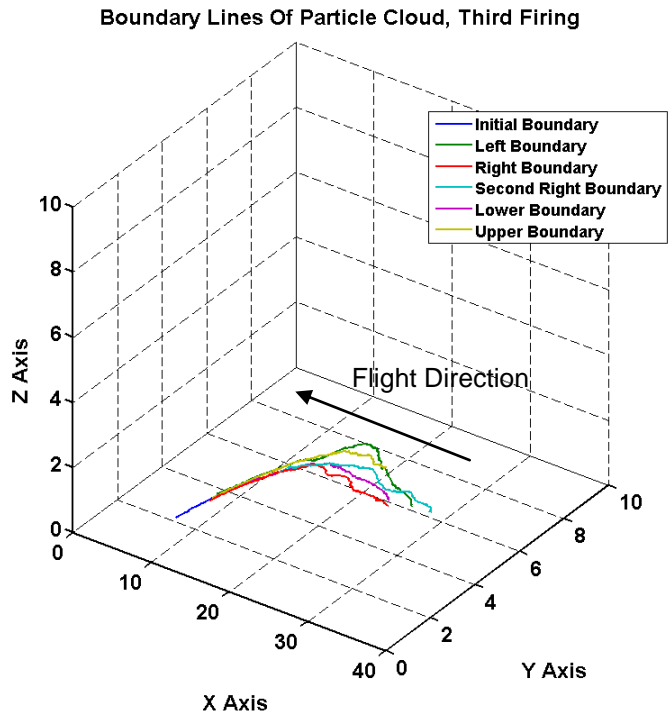


**Figure 39-Boundary Lines of Particle Cloud, Third Firing, Isometric View**

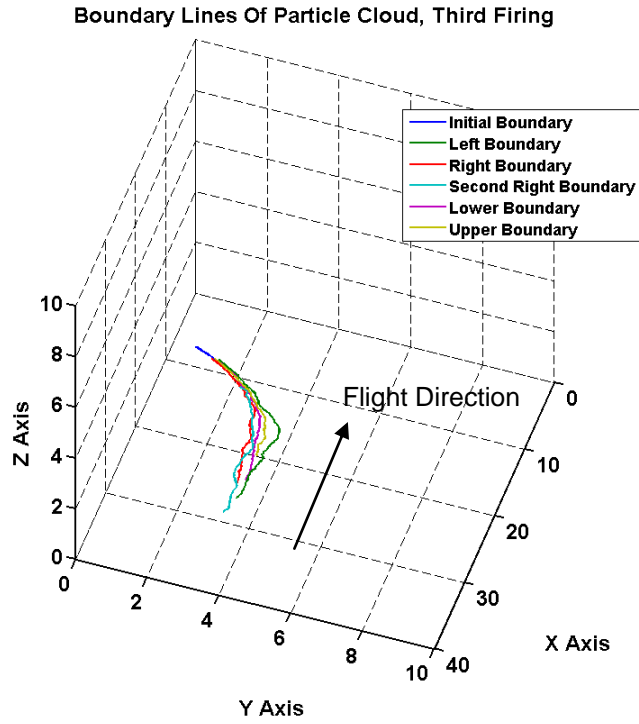


**Figure 40-Boundary Lines of Particle Cloud, Third Firing, Isometric View**

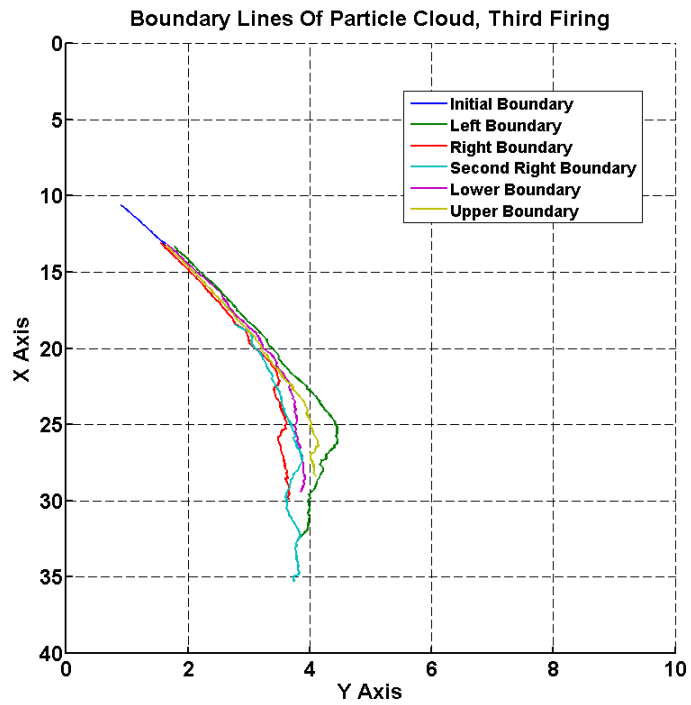


**Figure 41-Boundary Lines of Particle Cloud, Third Firing, Top View,**

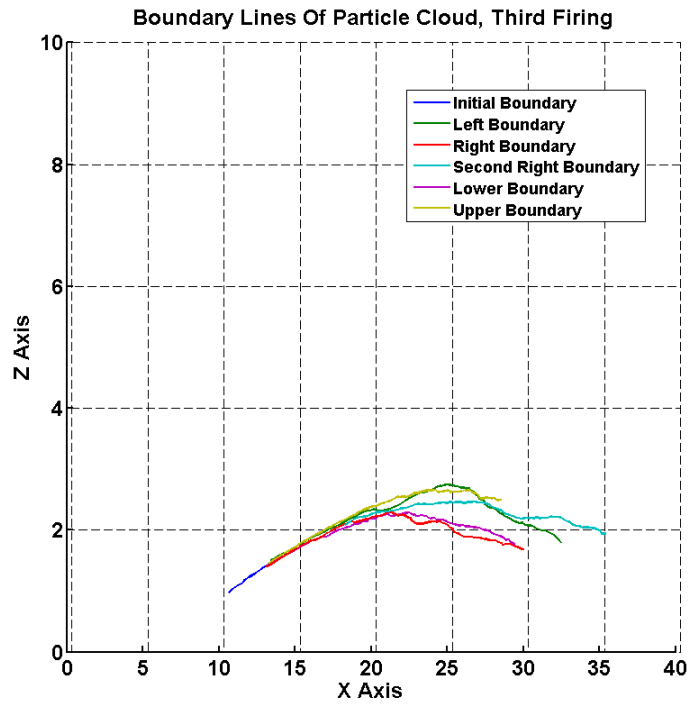


**Figure 42-Boundary Lines of Particle Cloud, Third Firing, Side View**

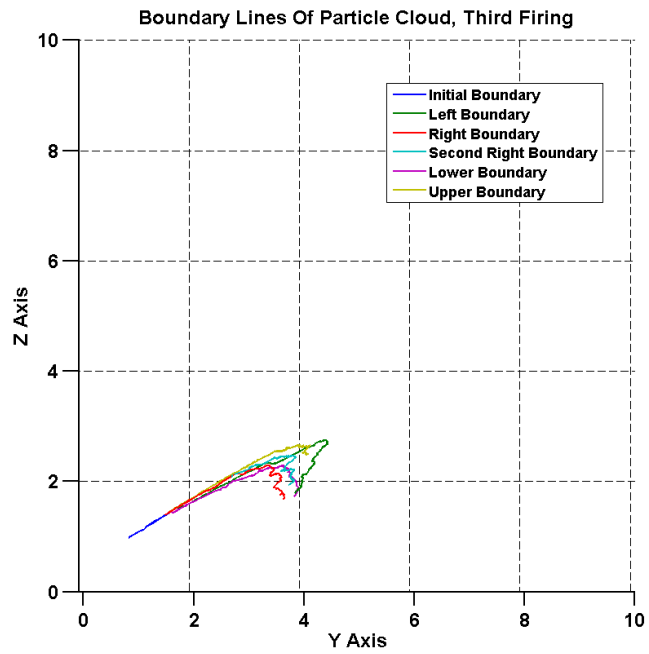


**Figure 43-Boundary Lines of Particle Cloud, Third Firing, Rear View**

Figure 44 shows some trajectories from the third firing data, while Figure 45 shows the generated series of splines passed through for the outermost chaff particles in the cloud. Finally, Figure 46 shows the constructed chaff cloud as a 3-D geometry.

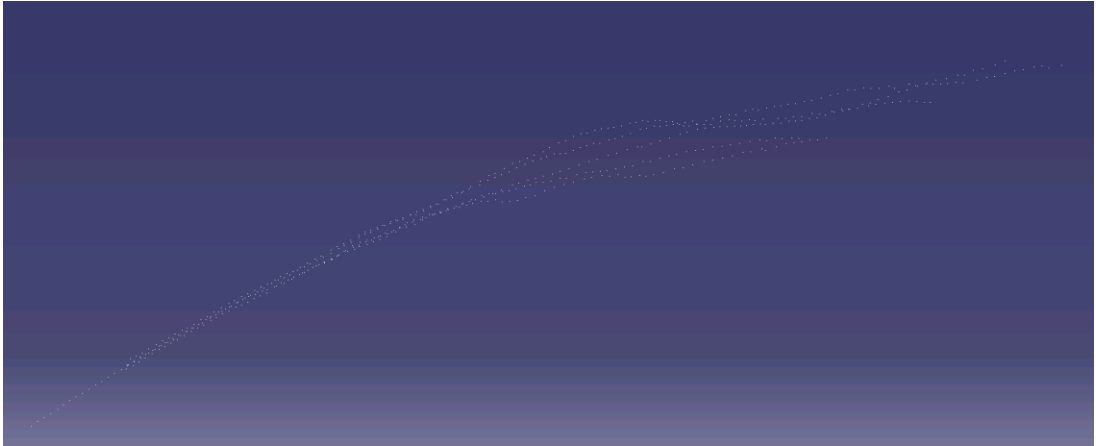


**Figure 44- Trajectory of First Firing Data**

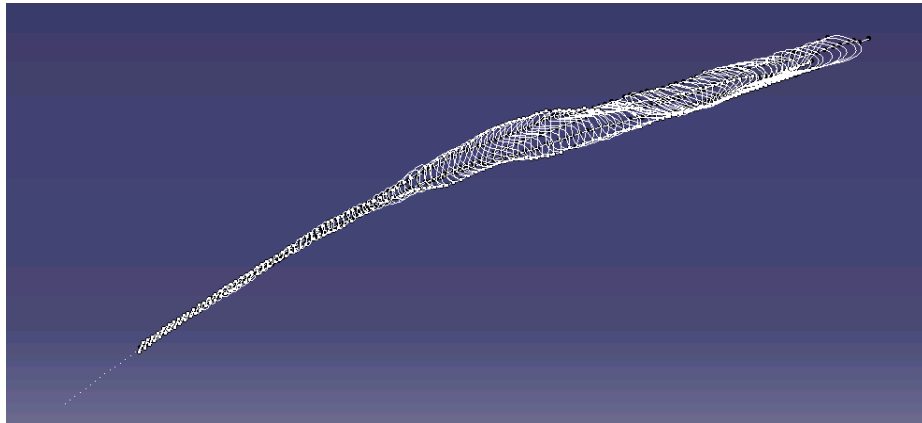


**Figure 45- Splines at All Time Steps**



**Figure 46- Geometry of The Chaff Cloud**

Figure 47a-d show the cross sectional areas of third generated chaff cloud at specified time intervals of 100 ms, 150 ms, 200 ms and 288 ms after firing.

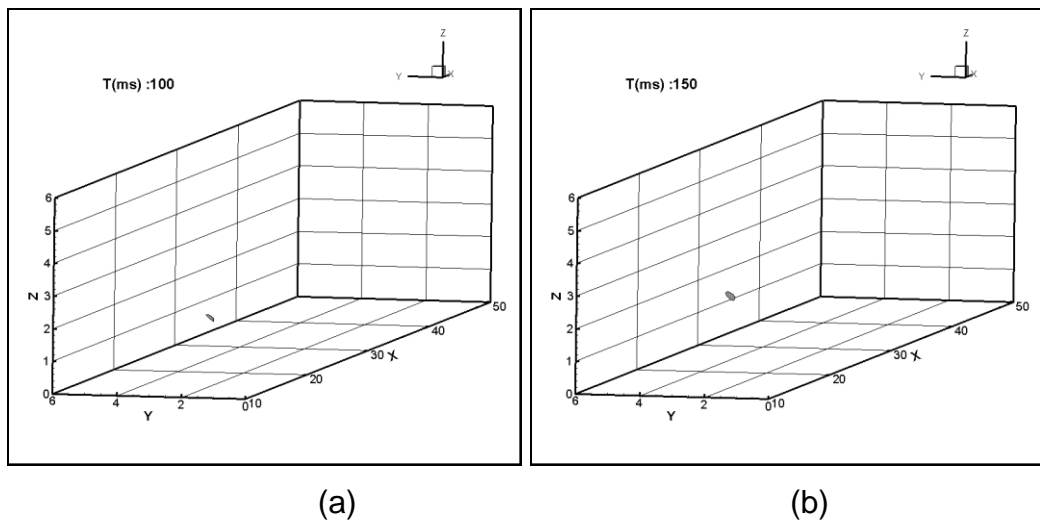


**Figure 47- Cross Section of Third Fired Chaff Cloud At Specified Time Steps**

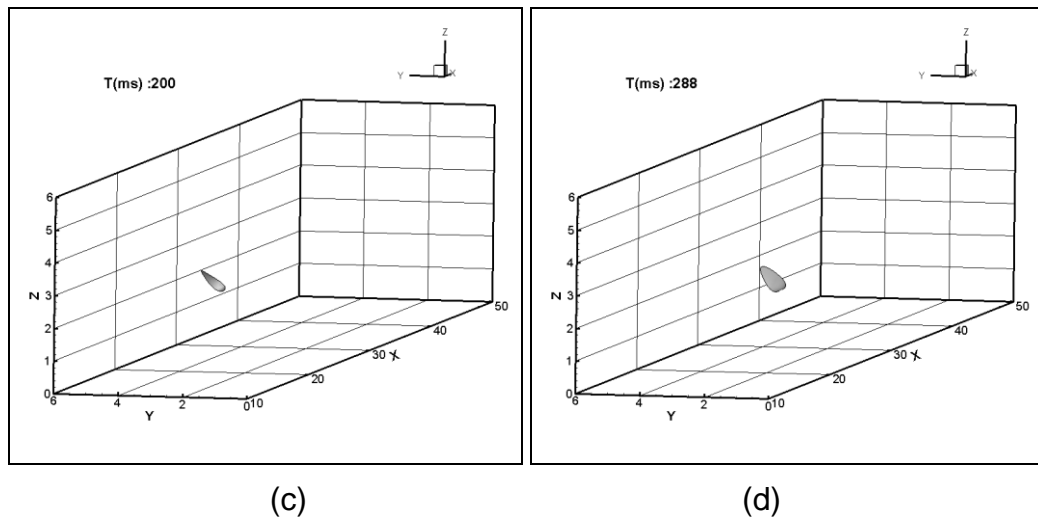


**Figure 47 (Continued)- Cross Section of Third Fired Chaff Cloud At Specified Time Steps**

These cross sections also give an idea about evolution of particle cloud. At first times, dispersion of chaff particles is limited. Their cross-sectional areas are very small. As time passes, with the help of the flow around the helicopter, particle cross sections start to grow.

The eight small figures shown in Figure 48 exhibit the evolution of the particle cloud from the third firing. The general dispersion characteristics of this cloud resemble those of the other firings with a small time delay. This time delay is mainly due to the birdnesting effect which took longer for this firing than the other firings.



**Figure 48- Evolution of Particle Cloud from Third Firing**

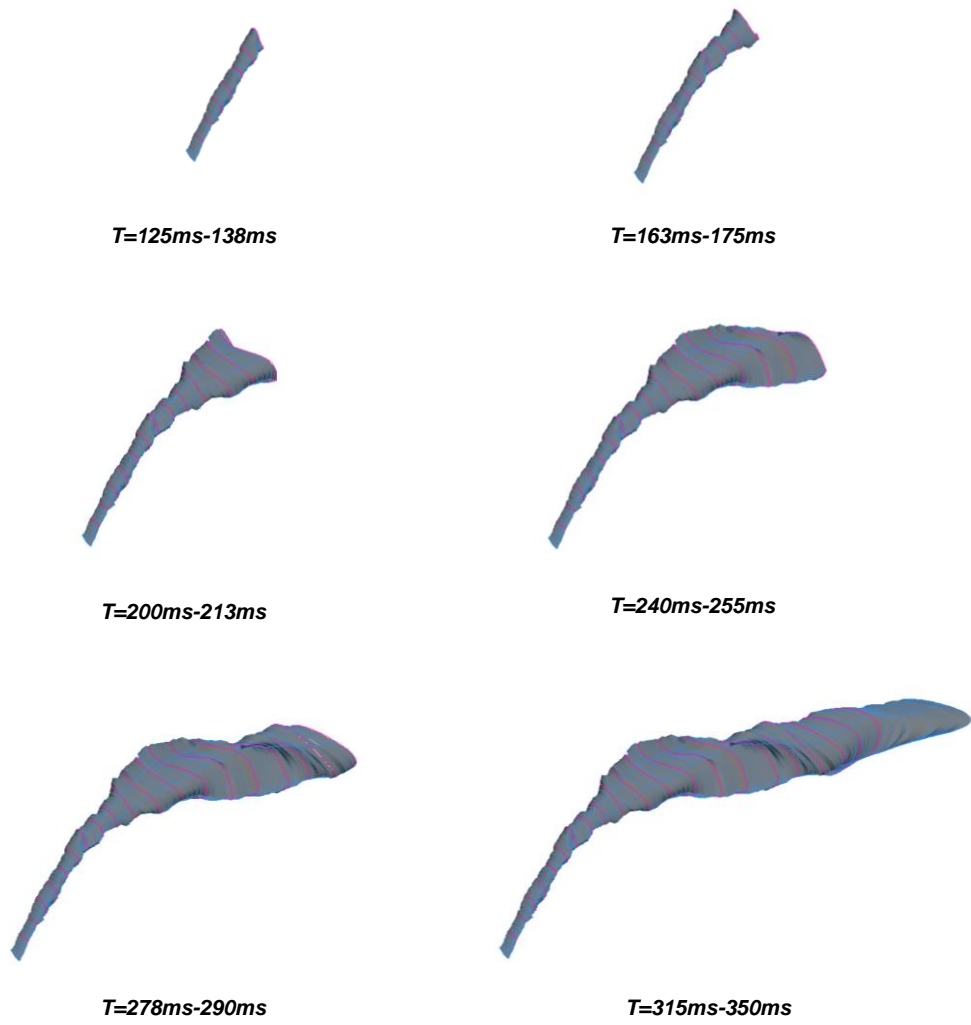


Figure 48 (Continued)- Evolution of Particle Cloud from Third Firing

## CHAPTER 4

### NUMERICAL METHOD AND FLOW SOLVER

#### 4.1 FLUENT

FLUENT [24] is a commercial CFD analysis software. It has capabilities of solving inviscid, laminar and turbulent flow problems. For turbulent flow problems, several turbulence models such as k-epsilon, k-omega and Spalart-Allmaras are available. Furthermore for highly swirling or anisotropic flows, Reynolds Stress Model (RSM) is also available. Regarding the turbulence, wall functions and enhanced wall treatment options for representing of wall bounded flows are also available inside. Both steady and unsteady analyses can be performed and different kinds of conditions such as heat transfer, phase change, reaction flow and multiphase can be modeled [24].

Meshes can be created by GAMBIT which is a pre-processor of FLUENT. GAMBIT's [25] unique curvature and size functions produce smooth meshes for CFD applications [25]. Another pre-processor tool is a TGRID [26], which can produce well defined boundary layers and domain meshes [26].

For multiphase applications, FLUENT has its own model called Discrete Phase Model (DPM). It is a Lagrangian model and with the help of this model spray dryers, liquid fuel injections, injection of particles, bubbles or droplets can be modeled and solved [24].

FLUENT is also capable of solving problems in parallel. Moreover user-defined functions can be embedded in to this software [24].

## 4.2 GOVERNING EQUATIONS

FLUENT solves conservation of mass and momentum for all kinds of flows. Additionally, the energy equation is solved when heat transfer and compressibility effects are taken into account. For turbulent flows, FLUENT solves some additional transport equations [24]. Since the flow field around the helicopter is turbulent, all solutions were solved with turbulence. Reynolds-Averaging was used during these analyses. The continuity and averaged momentum equations are given as follows

Continuity equation:

$$\frac{\partial \rho}{\partial t} + \frac{\partial}{\partial x_j} (\rho U_j) = 0 \quad (14)$$

Averaged Momentum Equation:

$$\rho \left( \frac{\partial \bar{U}_i}{\partial t} + \bar{U}_j \frac{\partial \bar{U}_i}{\partial x_j} \right) = \frac{\partial}{\partial x_j} \left[ -\bar{p} \delta_{ij} + \mu \left( \frac{\partial \bar{U}_i}{\partial x_j} + \frac{\partial \bar{U}_j}{\partial x_i} \right) - \rho \overline{u_i u_j} \right] \quad (15)$$

The first three terms on the right-hand side of Eq. (15) represents isotropic pressure component term, viscous stress and Reynolds stress.

The equation governing the kinetic energy of turbulent flow is given by

$$\left[ \frac{\partial k}{\partial t} + \bar{U}_j \frac{\partial k}{\partial x_j} \right] = -\frac{\partial}{\partial x_j} \left[ \frac{1}{2} \overline{u_i u_i u_j} + \frac{1}{\rho} \overline{p u_j} - 2\nu \overline{u_i s_{ij}} \right] - \overline{u_i u_j} \frac{\partial \bar{U}_i}{\partial x_j} - 2\nu \overline{s_{ij} s_{ij}} \quad (16)$$

where

$$s_{ij} = \frac{1}{2} \left( \frac{\partial u_i'}{\partial x_j} + \frac{\partial u_j'}{\partial x_i} \right) \quad (17)$$

### 4.3 TURBULENCE MODELING

Turbulent flows are characterized by fluctuating velocity. It is computationally expensive to solve turbulent flows by direct numerical simulations if fluctuating velocities inside the turbulence have high-frequency and a small scale that would require very fine meshes. In order to smooth these fluctuations and scales, instantaneous governing equations can be time-averaged, ensemble-averaged or manipulated. Hence, a modified set of equations is obtained which reduces the computational expense.

Modifying equations reveals some new unknowns. Turbulence models try to simulate these unknown parameters by using known quantities. Reynolds Averaging and Filtering methods are used to transform Navier-Stokes equations so that the small scale turbulent motions are not explicitly solved. The RANS (Reynolds Averaged Navier Stokes) equations represent transport equations for the mean flow quantities only with all scales of turbulence. The Spalart-Allmaras, k- $\epsilon$ , and k- $\omega$  models all use this approach.

Spalart and Allmaras described a one equation turbulence model for aerodynamic applications. This one equation model solves the transport equations for the kinematic turbulent viscosity [24].

The k- $\epsilon$  model is a two equation model. This two equation model solves transport equations for turbulence kinetic energy (k) and rate of dissipation of turbulent kinetic energy ( $\epsilon$ ) [24].

The RNG  $k$ - $\varepsilon$  model was derived by using renormalization group method. In the RNG  $k$ - $\varepsilon$  model, there is an additional term in the  $\varepsilon$  equation [27]. On the whole, RNG and the standard  $k$ - $\varepsilon$  models are similar to each other, but the  $\varepsilon$  term responsible for the performance differences between the standard and RNG models. The  $\varepsilon$  term in the RNG model, improves the accuracy for rapidly strained flows [24]. Furthermore the effect of swirl on turbulence is included in this model [24].

The realizable  $k$ - $\varepsilon$  model is a recently developed version. The differences between the standard  $k$ - $\varepsilon$  model and the realizable one stem from a new formulation for the turbulent viscosity and dissipation rate [24].

The second most widely used two-equation turbulence model is the  $k$ - $\omega$  turbulence model. This model has been developed by Wilcox and others. The expression of turbulence viscosity and turbulence kinetic energy are same as in  $k$ - $\varepsilon$  models. The difference comes from the  $\omega$  rather than  $\varepsilon$  [24].

#### **4.4 BOUNDARY CONDITIONS**

Boundary types and the corresponding state variables are defined in order to animate the test data conditions. There may be more than one appropriate boundary type for a given boundary. In this case, whichever boundary type results in most accurate and faster computations is employed.

Pressure inlet boundary condition was used for the upstream and side outer boundaries of the solution domain surrounding the helicopter geometry. Pressure inlet boundary condition is used with defined total pressure and total temperature values. Both at the upstream and side boundaries the total pressure and temperature were set to those of the free-stream. Also the flow direction and turbulence parameters were needed to be specified.

At the downstream boundary where the flow exits pressure outlet boundary condition was used. In FLUENT, this type of boundary condition requires the specification of a static (gauge) pressure. FLUENT extrapolates the pressure from the flow in the interior as well as all other flow quantities. In case of occurrence of backflow (flow reversal), the corresponding flow quantities from the outside of the domain must be specified.

For helicopter engine inlets and exhausts, mass flow inlet boundary conditions were employed. At these boundaries the mass flow rate, total (stagnation) temperature, static pressure, flow direction and turbulence parameters were specified.

For helicopter geometry itself, wall boundary condition was used. No slip boundary condition was enforced at the walls along with no normal heat transfer condition.

## **4.5 DISCRETIZATION**

FLUENT has two types of numerical methods as pressure-based solver and density-based solver. In the thesis the pressure based solver was used. In the pressure based approach, the pressure field is obtained by solving a pressure or pressure correction equation. FLUENT uses this method to solve governing integral equations for the conservation of mass, momentum, energy and turbulence. FLUENT also uses a control-volume based technique for the pressure-based solver. In this technique domain is divided into discrete control volumes using computational grid. The governing equations are for individual control volumes and algebraic equations for the discrete variables such as velocity, pressure and temperature are obtained [24].

In FLUENT, the scalar values are stored at cell centers. These values are interpolated by upwind scheme to obtain face values for the convection terms [24]. In the thesis first-order and second-order schemes are used. Numerical solutions are initiated using a first-order scheme to damp the errors that are large initially. In the first-order upwind scheme, it is assumed that cell center values are equal to cell face quantities. After the flow field starts settling, the discretization method is changed to second order. In the second-order scheme, Taylor series expansions of the cell centered solution about cell centroid are used in order to obtain higher order accuracy at cell faces [24].

PRESTO! is used in the analysis as a pressure interpolation scheme. This scheme uses the discrete continuity balance for a "staggered" control volume about the face to compute the "staggered" pressure to come over for flows with high swirl numbers, high Rayleigh-number natural convection and high-speed rotating flows [24].

Gradients which are used for computing diffusion terms and velocity derivatives in addition to construct values of scalar at cell faces can be computed in FLUENT in three different ways. In this thesis Green-Gauss-Node-Based type was used. According to this type, cell value can be computed by the arithmetic average of the nodal values on the face. The following expression is used for this type [24];

$$\bar{\phi}_f = \frac{1}{N_f} \sum_n^{N_f} \bar{\phi}_n \quad (18)$$

In order to avoid divergence at the beginning of the analysis, small under relaxation factors were chosen because of the non-linearity of the equations. The control of relaxations factor is important since very low values cost extensive computational time whereas high values result in

diverged results. The method used during the under-relaxation is stated as below [24].

$$\phi = \phi_{old} + \alpha\Delta\phi \quad (19)$$

## 4.6 VIRTUAL BLADE MODEL

There are different ways of modeling rotors in FLUENT. The simplest one is the fan model [24]. In this model, a time-averaged pressure jump condition across the fan surface is implemented. However, flow characteristics through the fan blades cannot be modeled accurately with this model. It only predicts the amount of flow coming from the fan. Although the fan model is easy and fast, the basic requirements related to the blade and rotor aerodynamics are not accounted for. Therefore, this model cannot give accurate result for this kind of applications.

Another way of modeling the rotor is the MRF (Multiple Reference Frame) model [24]. In this model blades are individually meshed. Therefore, number of cell counts in the domain increases as a consequence of resolution of all the blades. Rotation effects are modeled via source terms in the equations and the blades are not actually rotated. However, the cyclic pitch variations along the azimuthal direction cannot be modeled [28].

Sliding mesh model is the third way of modeling the rotor [24]. In this model, each blade is individually meshed. The blades are moved in real time. Since a rotation exists in real time, resolving of the blades and flow domain around the blades becomes important.

The Virtual Blade Model, the fourth among all models, can be thought as a model between the fan model and MRF models [28]. In this model, the blade geometric parameters, local flow incidence angles, airfoil data, etc are

all taken into account. Therefore, the VBM is a more accurate model than the fan model.

In the Virtual Blade Model, rotor blades are not meshed individually. Instead, time-averaged aerodynamic effects of the rotating blades are modeled with momentum sources on an actuator disk [8]. The momentum sources generate a pressure jump across the actuator disk. Generated pressure differences vary with the radial section and azimuth of the blades. Momentum source terms that are used to generate pressure jumps are computed based on the Blade Element Theory [8]. During this calculation, blade twist, chord and local flow incidence angles are taken into account implicitly. In this model local blade aerodynamics is not computed directly; rather, its effects are modeled with the available blade section aerodynamics data [8].

At the beginning of the analysis, the values of the momentum source terms are unknown. The Mach number, local flow incidence and Reynolds number are needed by this theory, and all these parameters are calculated from the solved flow field. A transformation is performed for the velocity component from the global coordinate to the blade coordinate system.  $C_l$  and  $C_d$  values for blade sections are obtained from look up tables. Instantaneous sectional rotor forces are calculated as follow [8];

$$f_{L,D} = c_{L,D}(\alpha, Ma, Re) \cdot c(r/R) \cdot \frac{\rho \cdot U_{tot}^2}{2} \quad (20)$$

where  $C_{L,D}$  stands for 2D airfoil lift (subscript L) and drag (subscript D) coefficients,  $\alpha$  stands for the local angle of attack, and  $U$  stands for the total lift/drag producing velocity component experienced by each blade cross-section including the angular velocity  $\omega$  [8]. Time averaging of one

period is identical to geometric averaging over an angle of  $2\pi$  if revolution of the rotor is assumed constant [8]. The overall lift and drag forces are then calculated by the integral

$$F_{L,D} = N_b \int_0^R f_{L,D} dr \quad (21)$$

Hence, the resultant force per blade element becomes [8]

$$F_{L,D,cell} = N_b \frac{dr \cdot rd\theta}{2\pi r} \cdot f_{L,D} \quad (22)$$

By transforming this force vector into the flowfield reference frame, time averaged source term is obtained, which is given as [8].

$$\vec{S}_{cell} = -\frac{\vec{F}_{cell}}{V_{cell}} \quad (23)$$

This time averaged source term is added to the momentum equation and the flowfield is updated accordingly. This procedure is repeated until the solution converges.

The VBM enables user to define desired thrust and moment coefficient [8]. Correct twist and cyclic pitches are then obtained iteratively in order to achieve the desired coefficients. While doing this calculation, the Newton-Rapson iterative method is used [8].

In VBM, spanwise blade lift and drag values are computed assuming two-dimensional flow [8]. In nature this assumption is not valid near the tip of the blades because of strong secondary flows around there, namely tip effects. In order to model this phenomenon, the VBM allows user to define

what percentage of the blade is affected by the secondary flow [8]. According to this percentage, the region under the secondary flow is assumed to create no lift while drag still exists.

#### **4.7 DISCRETE PHASE MODEL**

In FLUENT, a discrete second phase which consists of particles dispersed in the continuous phase can be modeled in a Lagrangian frame of reference in addition of solving the transport equation for continuous phase [24]. Mass and heat transfer between these phases and trajectory calculation of these entities can be computed. Therefore, coupling between the phases, their effects on each other and their trajectories are all included in FLUENT [24]. Furthermore, for both steady and unsteady situations a discrete phase trajectory can be calculated by Lagrangian formulation by taking into account the discrete phase inertia, hydrodynamic drag and gravitational force. This model can also account for the effects of turbulent eddies of the continuous phase on the dispersed particles [24].

Heating and cooling of the discrete phase, vaporization and boiling of liquid droplets as well as combusting particles can also be modeled via this model [24].

With the help of the modeling capabilities stated above, FLUENT has a wide range of simulating discrete phase problems such as particle separation, spray drying, aerosol dispersion, liquid fuel combustion, etc. FLUENT 's this modeling capability, namely the "Discrete Phase Model" is employed in this thesis in order to simulate chaff dispersion.

The physical equations that are used during discrete phase calculation are given in following sections.

## 4.8 PARTICLE MOTION THEORY

### 4.8.1 EQUATIONS OF MOTION FOR PARTICLES

FLUENT integrates the force balance on discrete phase particles in Lagrangian reference frame and calculates their trajectories. This force balance equates the particle inertia with the forces acting on the particle. When this equation is written in Cartesian coordinate system for the x direction, it becomes [24]

$$\frac{du_p}{dt} = F_D(u - u_p) + \frac{g_x(\rho_p - \rho)}{\rho_p} + F_x \quad (24)$$

In this equation  $F_x$  stands for an additional acceleration term (force/unit particle mass), and  $F_D(u - u_p)$  stands for the drag force per unit particle mass.

$F_D$  is defined as follows [24];

$$F_D = \frac{18\mu C_D \text{Re}}{\rho_p d_p^2 24} \quad (25)$$

In these equations  $u$  is the fluid phase velocity,  $u_p$  is the particle velocity,  $\mu$  is the molecular viscosity of the fluid,  $\rho$  is the fluid density,  $\rho_p$  is the density of the particle,  $d_p$  is the particle diameter, and Re is the Reynolds number for the particle which is defined as [24]:

$$\text{Re} = \frac{\rho d_p |u_p - u|}{\mu} \quad (26)$$

As can be seen from equation (24), the gravity term is also included in the force balance equation.

The force required to accelerate the fluid around the particle is defined as [24]

$$F_x = \frac{1}{2} \frac{\rho}{\rho_p} \frac{d}{dt} (u - u_p) \quad (27)$$

The additional force that arises due to the pressure gradient in the fluid is defined as [24].

$$F_x = \left( \frac{\rho}{\rho_p} \right) u_{p_i} \frac{\partial u}{\partial x_i} \quad (28)$$

The drag coefficient that appears in equation (25) is expressed for non-spherical particles by using the Haider and Levenspiel equation [24] which is given as ;

$$C_D = \frac{24}{\text{Re}_{sph}} \left( 1 + b_1 \text{Re}_{sph}^{b_2} \right) + \frac{b_3 \text{Re}_{sph}}{b_4 + \text{Re}_{sph}} \quad (29)$$

where the constant are [24]

$$\begin{aligned} b_1 &= \exp(2.3288 - 6.4581\phi + 2.4486\phi^2) \\ b_2 &= 0.0964 + 0.5565\phi \\ b_3 &= \exp(4.905 - 13.8944\phi + 18.4222\phi^2 - 10.2599\phi^3) \\ b_4 &= \exp(1.4681 + 12.2584\phi - 20.7322\phi^2 + 15.8855\phi^3) \end{aligned} \quad (30)$$

In the Haider and Levenspiel equation, the shape factor  $\phi$  is defined as [24]

$$\phi = \frac{S}{S} \quad (31)$$

In this equation,  $s$  is the surface area of a sphere having the same volume as the particle and  $S$  stands for the actual surface area of the particle. The Reynolds number stated in equation (29) is calculated by using the diameter of the sphere having the same volume.

#### **4.8.2 TURBULENT DISPERSION OF PARTICLES**

The effect of turbulence on particle dispersion in fluid phase is calculated by a stochastic tracking model called “random walk.” This model includes the effect of instantaneous turbulent fluctuations on the particle trajectory [24]. Furthermore generation or dissipation of turbulence in the continuous phase can be taken into account by using this model.

In the stochastic tracking approach, FLUENT uses instantaneous fluid velocity  $\bar{u} + u'(t)$  to calculate the turbulent dispersion of the particles with integration of the trajectory equations for individual particles along the particle path [24]. With this method random effects of turbulence on particle dispersion are taken into account. In this model each particle injection is tracked repeatedly in order to generate statistically meaningful sampling [24].

#### **4.8.3 TRAJECTORY CALCULATIONS**

Coupled discrete phase calculations were performed during analysis. In a coupled two-phase simulation, FLUENT solves the continuous flow initially. Then discrete phase is generated by calculating the particle trajectories for each discrete phase injections. After discrete phase is generated, continuous phase flow is recalculated by using the interphase exchange of momentum, heat, and mass. After continuous phase flow is recalculated that is to say modified, trajectories of discrete phase is also recalculated. This procedure continues until there exist unchanged with each additional

iterations. Figure 49 shows the coupled discrete phase calculation procedure.

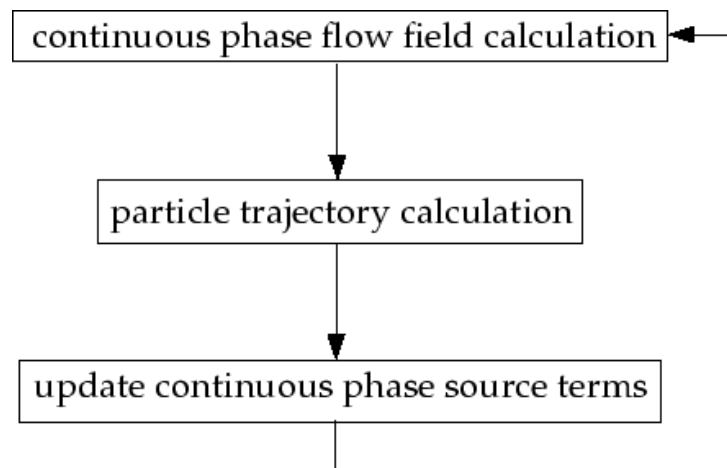


Figure 49- Coupled Discrete Phase Calculation Procedure [24]

Figure 50 shows the interphase change of mass, momentum and heat from particle to continuous phase.

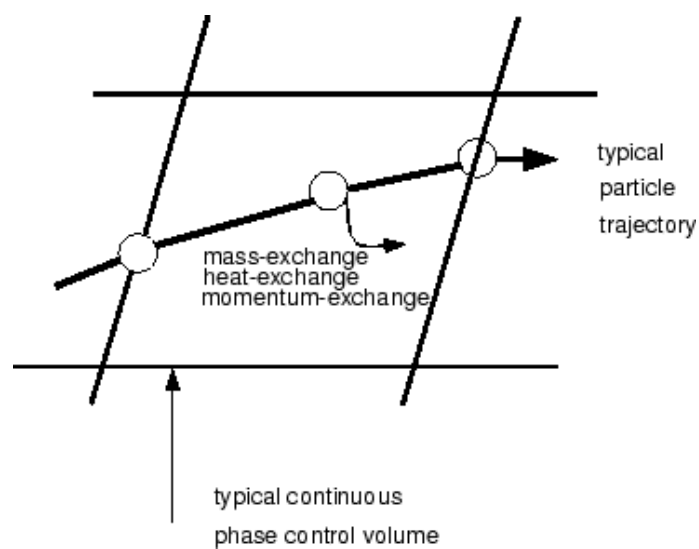


Figure 50- Mass, Momentum and Heat Transfer [24]

Momentum transfer from continuous phase to the discrete phase is defined in FLUENT as follows [24] ;

$$F = \sum \left( \frac{18\mu C_D \text{Re}}{\rho_p d_p^2 24} (u_p - u) + F_{other} \right) \dot{m}_p \Delta t \quad (32)$$

This momentum transfer is computed by calculating the momentum change of a particle as it goes over each control volume

Heat transfer from continuous phase to the discrete phase is defined in FLUENT as follows [24] ;

$$Q = (m_{p_{in}} - m_{p_{out}}) [-H_{lat_{ref}} + H_{pyrol}] - m_{p_{out}} \int_{T_{ref}}^{T_{p_{out}}} c_{p_p} dT + m_{p_{in}} \int_{T_{ref}}^{T_{p_{in}}} c_{p_p} dT \quad (33)$$

This heat transfer is computed by calculating the internal energy change of a particle as it goes over each control volume. Mass transfer from continuous phase to the discrete phase is defined in FLUENT as follows [24];

$$M = \frac{\Delta m_p}{m_{p,0}} \dot{m}_{p,0} \quad (34)$$

This mass transfer is computed by calculating the mass change of a particle as it goes over each control volume.

#### 4.8.4 DPM INITIAL CONDITIONS

Initial conditions define starting values for discrete phase parameters and these discrete phase parameters constitute the instantaneous condition for

all individual particles. In FLUENT the following initial conditions can be described [24].

- 3-D position of particle
- Velocity of particle
- Diameter of particle
- Temperature of particle
- Mass flow rate of particle

Once the injection was created, injection properties characterizes the type of this injection. As an injection properties particle types, injection types and material of the particles are defined.

In FLUENT, many number of injection types can be defined. In this thesis only two of them were used. These are surface injection and file injection.

Surface injection can be defined as particle streams are injected from a surface. For each face, one particle stream is injected. For surface all the initial conditions defined except 3-D position of particles. The initial location of particles are the specified position on the surface. Figure 51 shows the surface injection.

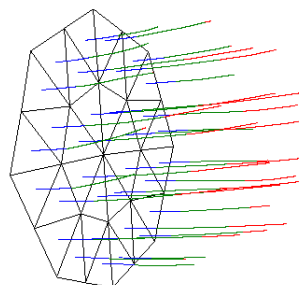


**Figure 51-Surface Injection [24]**

Particle initial conditions can also be read from an external file if none of the injection types are suitable that kind of problem. Figure 52 shows the format of file injection type.

```
(( x y z u v w diameter temperature mass-flow) name )
```

**Figure 52-File Injection Type [24]**

In FLUENT four type of particles can be defined as an initial conditions. These are inert, droplet, combusting and multicomponent particle types. An inert particle is a discrete phase element (particle, droplet or bubble) obeys the force balance and it is subjected to heating or cooling. This type of particle is available for all models in FLUENT. In thesis inert particle type is used during analysis. The particle material can also be selected from the existing material that already defined in FLUENT or user can define unique particle. In thesis chaff particle is defined according to its parameters.

## **4.9 COMPUTATIONAL GRID GENERATION**

All computational grids used in this thesis were generated by using FLUENT preprocessors. GAMBIT was used while generating grid for unstructured surface meshes. GAMBIT was also used for generating flow domain boundaries, main rotor and tail rotor volume meshes. TGRID was employed for generating the boundary layers on the helicopter geometry. It was also used to make improvements on the surface meshes.

The computational grid used in thesis is made up of four main parts. These parts in sequence are helicopter surface, boundary layer around the helicopter, main rotor and tail rotor meshes.

Initially, helicopter geometry was imported to GAMBIT as a step format. Then, some surface modifications were made to geometry because of the gaps, duplicated faces and unwanted surfaces that came with the geometry file. These all made the grid generation difficult. As a next step, modifications were made to smooth the model. This procedure is essential for not resolving unnecessarily detailed surfaces for aerodynamic analyses that leads better surface meshes. Better surface meshes means better boundary layer meshes and also better domain meshes. Furthermore eliminating detailed surfaces decreases the number of cells created which plays an important role in computational time.

While creating surfaces meshes, a curvature size function was used. This tool is an ability of GAMBIT, and by using this tool, the angles between adjacent grid cells can be determined. Furthermore, maximum and minimum allowable grid cell size can be applied. Since the models usually have sharp corners, and high angle curved faces, mesh density around these areas should be higher than in the other regions. While determining the size function values, the location of the chaff dispenser and possible trajectory were taken into account. Hence, more than one size function values were applied to separate regions of the model. These were the main body, empennage and the lifting surfaces. Applying different size function values to each region yields better distributed cells. Also in regions where high flow gradients were expected. Figure 53 shows the generated mesh around part of the fuselage and tail boom.

After surface meshing was accomplished, the mesh file was imported to TGRID to generate the boundary layer mesh.

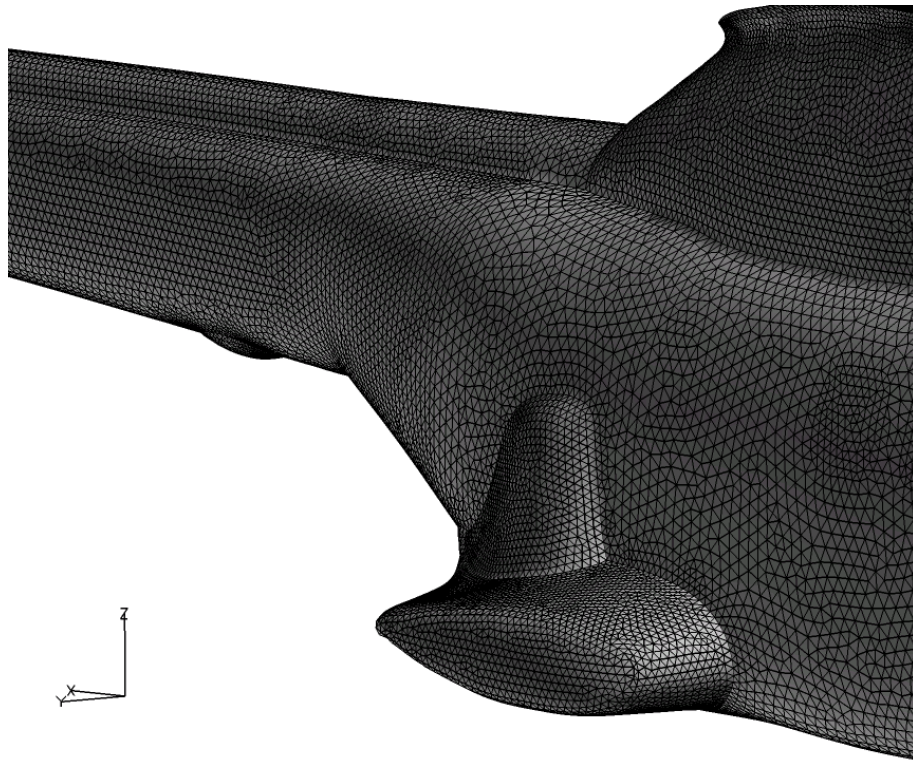


**Figure 53-Fuselage and Tail Boom Mesh Distribution.**

Boundary layer mesh was generated using TGRID. After importing the mesh file into the program, some surface modifications were carried out. This procedure was critical because creating sufficient number of boundary layer cells, surface meshes in some regions needed to be modified through the merge, split and smooth operations. While generating boundary layer cells, the last-ratio method was used. This method adjusts the height of the last row of the boundary layer mesh according to the determined percentage of the edge size of the surface mesh [26]. This method leads to a smooth transition from the boundary layer wedge cells to the unstructured tetrahedral volume cells. If a fixed cell method had been used the thickness of the boundary layer around the helicopter would have remained the same and in some regions unbalanced growth of the boundary layer cells would have existed. A significantly high number of layers and hence a significant boundary layer region thickness was achieved without damaging the overall

mesh quality. The first thickness of boundary layer cells is important to resolve the flow gradients. This thickness was determined according to the y-plus criteria. The y-plus values for the generated mesh on the fuselage ranged between 30 and 250. At this point it should be noted that the requirement for the value of y-plus changes from one turbulence model to another. The above values meet the criteria for the turbulence model employed in this thesis.

Figure 54 shows the thickness of the boundary layer cells generated around the helicopter geometry while Table 2 gives the boundary layer properties applied during the generation. Figure 55 shows the distributed boundary layer thickness around the helicopter.

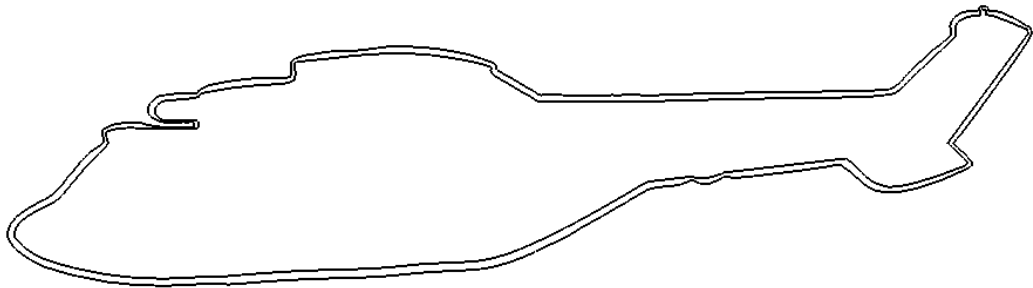


**Figure 54 -Boundary Layer Thickness**

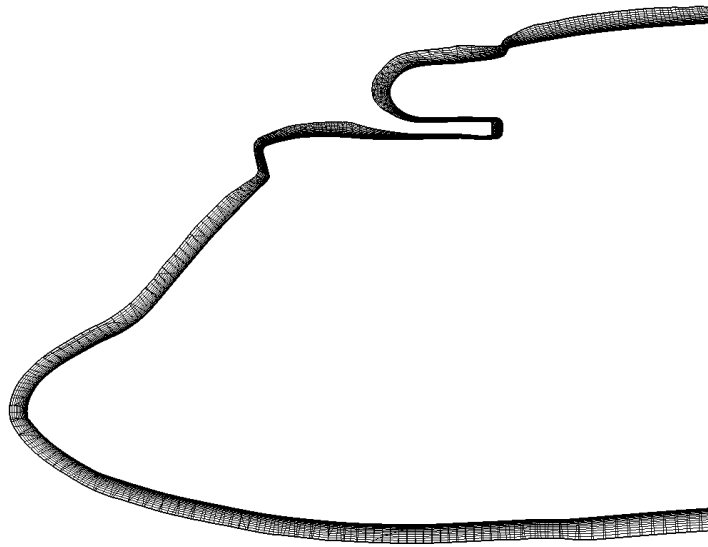


**Figure 55- Distributed Boundary Layer Thickness**

**Table 2-Boundary Layer Properties**

First Layer Thickness (m)	0.0025
Numbers of Layer	14
Last Layer to Edge Size Ratio	60

Since in the analyses the VBM was used, blades were not modeled individually. In VBM, rotors are modeled as computational fluid zones. The thickness of rotor domain was determined in a way not to alter the growth of the mesh from boundary layer to the rotor zones. This was important because the distance between the helicopter surface and rotor domain is not very big. The main and tail rotor surface meshes were created by the 'Pave Scheme'. For volume meshes, the 'Cooper Scheme' was used. For both rotor surface meshes, a size function was used near the rotor root and tip to refine the mesh there. Figure 56 shows the main and tail rotor mesh distributions.

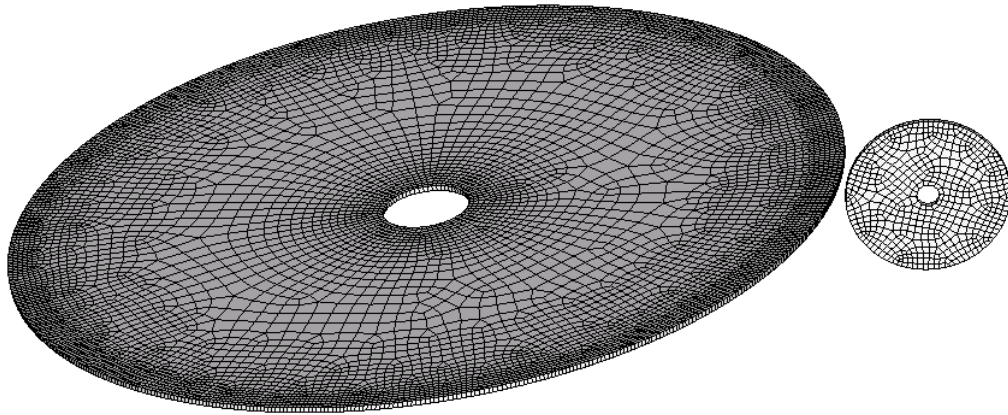


**Figure 56-Main and Tail Rotor Mesh Distributions**

The flow domain contains the helicopter geometry, rotor fluid zones and meshed surfaces for the three firings at different time steps. The domain was created in sufficiently large size so that the flow conditions at the boundaries are approximately those of the free stream. Therefore, the dimensions of the domain were much larger than the helicopter dimensions. Moreover, in order to increase the convergence rate and have the boundary conditions well defined, all outer side faces of the domain were tilted 5.5 degrees outward so that they were the flow-inlet boundaries. Figure 57 shows the mesh structure on the boundaries of the flow domain. The domain extends 100 meters upstream, sideways, above and below from the helicopter and 200 meters downstream.

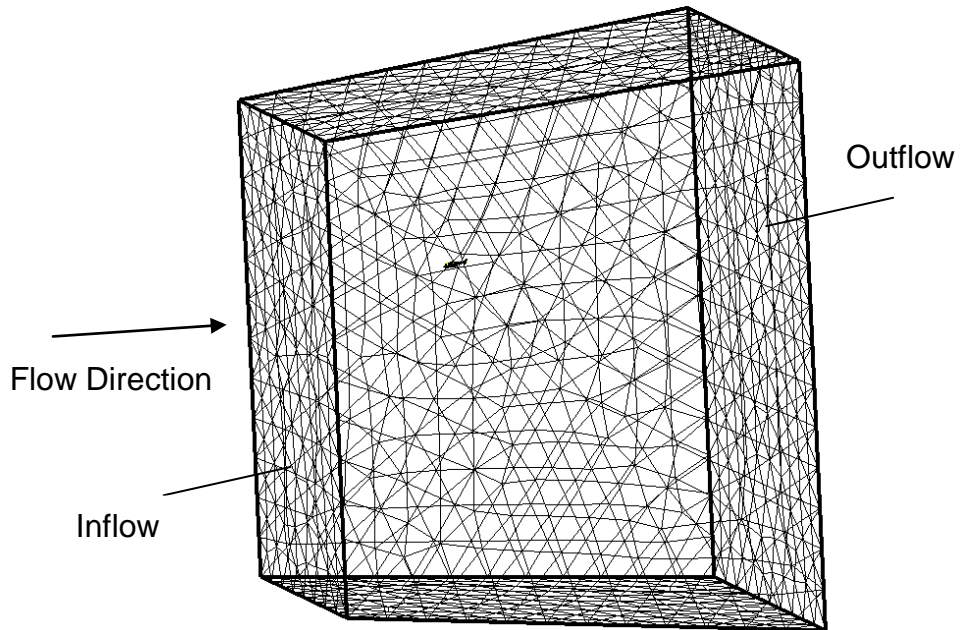


**Figure 57- Flow Domain Mesh**

As seen in Figure 56, while the main and tail rotor domains were filled with quadrilateral elements, tetrahedral elements were used for the volume mesh. The transition from quadrilateral cells to tetrahedral elements was achieved through use of  $120^{\circ}$  pyramid cells.

Control surfaces in some regions inside the flow domain, usually in the region where chaff particles were expected to travel, were used to refine the computational mesh there. Figure 58 shows the flow domain mesh around helicopter geometry. Table 3 summarizes the mesh size of subparts and Table 4 summarizes the mesh skewness.

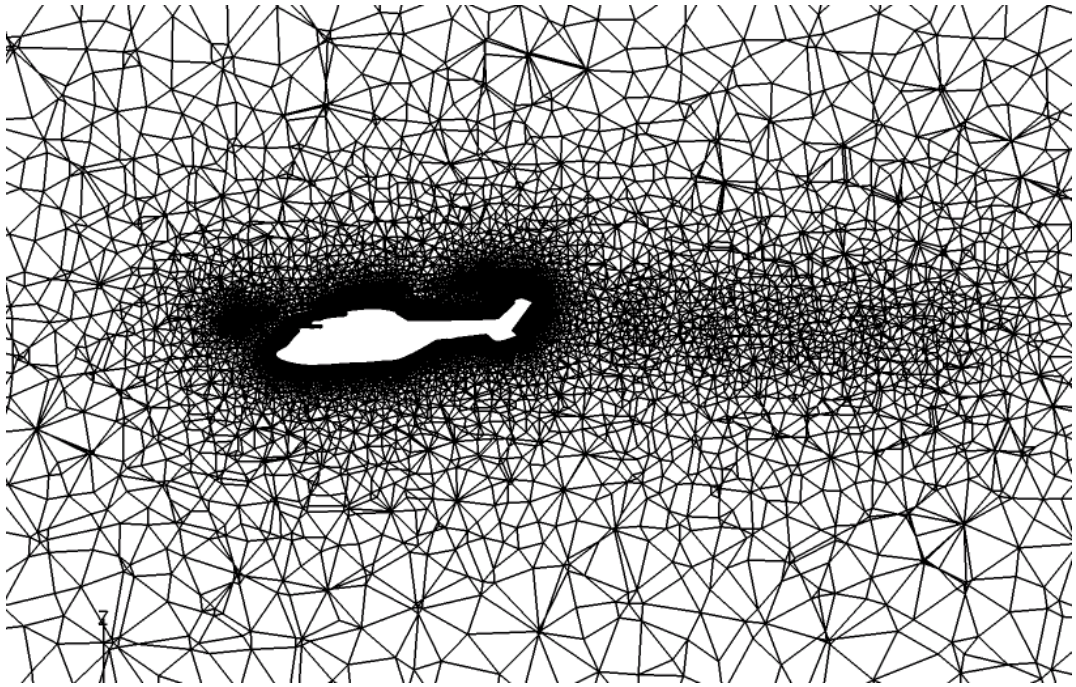


**Figure 58- Flow Domain Mesh Around Experimental Data**

**Table 3-Mesh Size**

	Number of Mesh Size
Fuselage Surface Mesh	159472
Main Rotor Mesh (Vol+Surf)	25200
Tail Rotor Mesh (Vol+Surf)	1658
Boundary Layer	2263608
Volume Mesh (total)	5858198

**Table 4-Mesh Skewness**

	Maks. Skew	Avg. Skew
Fuselage Mesh	0.92	0.044
Volume Mesh	0.96	0.26

## CHAPTER 5

### FLOW SOLVER VALIDATION TEST CASE

#### 5.1 OVERVIEW

The downwash of the rotor on the fuselage and its empennage produces an effect on the overall helicopter performance especially at hover and low-speed flight. The flow field is complicated due to separated region around the helicopter. Furthermore, interactions of the free stream about the fuselage with the rotor wakes make this phenomenon even more complicated. Therefore, the purpose of this chapter was set to understand which eddy viscosity models around a rotorcraft fuselage yield good results as well as to validate the VBM tool. The helicopter geometry chosen for this study was the experimental ROBIN (ROtor-Body-INteraction Fuselage) [9] configuration which was tested extensively in the Langley 14-by 22 Foot Subsonic Wind Tunnel [9], [11].

Analyses were performed considering only the body with the main rotor configuration. While modeling the main rotor, actuator disk theory was used and the trim module was switched on. Numerical investigations were carried out at an advance ratio of  $\mu = 0.15$ . Solutions at this advance ratio were compared with the available surface pressure experimental data at different sections.

## 5.2 ROBIN VALIDATION TEST CASES

The numerical computations performed at  $\mu = 0.15$  correspond to the experimental data set from RUN 25, Point 148 at the Langley tunnel (the Freeman and Mineck [9]). This advance ratio corresponds to a free stream Mach number of  $M_{inf} = 0.087$ . The fuselage angle of attack with respect to the free stream was  $2.86^\circ$ . The rotor shaft was tilted forward with a value of  $2.00^\circ$  with respect to the fuselage reference line. The actuator disk was defined in the shaft plane. The rotor thrust coefficient was  $C_T = 0.005$  [9]. Table 5 summarizes the Model Geometry. Figure 59 shows the model of ROBIN in the wind tunnel.

Table 5-Model Geometry [9]

<b>Fuselage :</b>	
<b>Moment Reference Center</b>	X=0.690R Y=0.0 R Z=0.0 R
<b>Length</b>	2.0 R
<b>Rotor :</b>	
<b>Hub Coordinates</b>	X=0.690R Y=0.0 R Z=0.124 R
<b>Number of Blades</b>	4
<b>Rotor Shaft Tilt Angle</b>	2
<sup>1</sup> Xs	0.009 R
<sup>2</sup> Zs	0.034 R

---

<sup>1</sup> distance from moment reference center of gimbal pivot point

<sup>2</sup> distance from moment reference center of gimbal pivot point

**Table 5 (Continued)-Model Geometry [9]**

<b>Hh</b>	0.090 R
<b>Root Cutout</b>	0.20 R
<b>Chord</b>	0.108 m
<b>Radius</b>	1.574 m
<b>Twist</b>	-8.0°
<b>Flapping Inertia</b>	0.653 Kg-m <sup>2</sup>
<b>Solidity</b>	0.0871

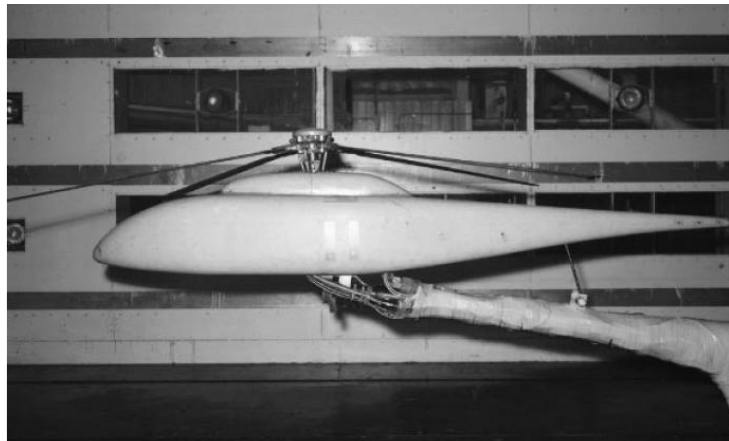


**Figure 59- Model of ROBIN in wind tunnel [10]**

### **5.3 MESH GENERATION**

The computational mesh was generated using the GAMBIT [25] and TGRID [26] mesh generators. The surface and volume meshes were generated using GAMBIT but boundary layers were generated using TGRID. In order to decrease computational time, computational domain was generated as a pyramid. Table 6 shows the dimensions of the computational domain while Figure 60 shows the computational domain for the ROBIN analyses, and Figure 61 displays the mesh generated for main rotor as an actuator disc.

**Table 6-Dimensions of the Computational Domain**

Computational Domain	Inward Direction	Outward Direction	Sideward Direction	Number of Cells
	5 rotor length	10 rotor length	5 rotor length	1435091

Pyramid Domain	
Length	50 meter
Enter width	10 meter
Exit width	15 meter

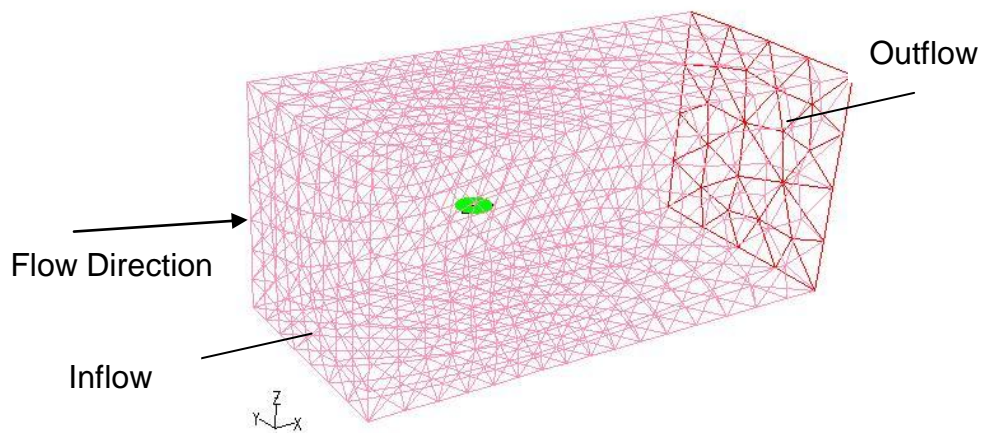


**Figure 60- Computational Domain for ROBIN analyses**

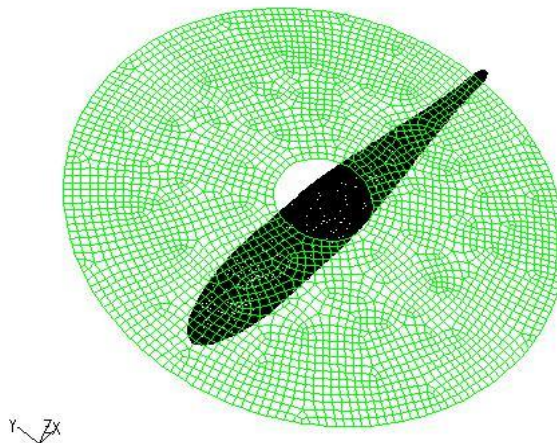


**Figure 61- Main rotor mesh (actuator disk)**

Since in this analysis different turbulent viscosity models were used, first cell size of the boundary layer was critical. The Spalart-Allmaras model is less sensitive to first cell size of the boundary layer than the other models. The reason is that it can adapt itself to first cell size. Since for the other models the first cell size plays an important role, a fine grid was generated. While generating this grid, the parameters related to the size of the first cell, ratio of two successive cells and the size of the last cell taken were into account. Close to the fuselage the ratio of grid expansion was taken small (1.05) and 10 layers of grid were generated. This was the fine part of the boundary layer. On top of this, a second part was generated with an expansion coefficient of 1.2 and again 10 layers of cells. Hence, a total of 20 cell layers were generated over the fuselage to resolve the turbulent boundary layer. These meshes were generated using TGRID [26] . Figure 62 shows the computational domain around the helicopter with boundary layer grid and Figure 63 shows the boundary layers around the ROBIN geometry.

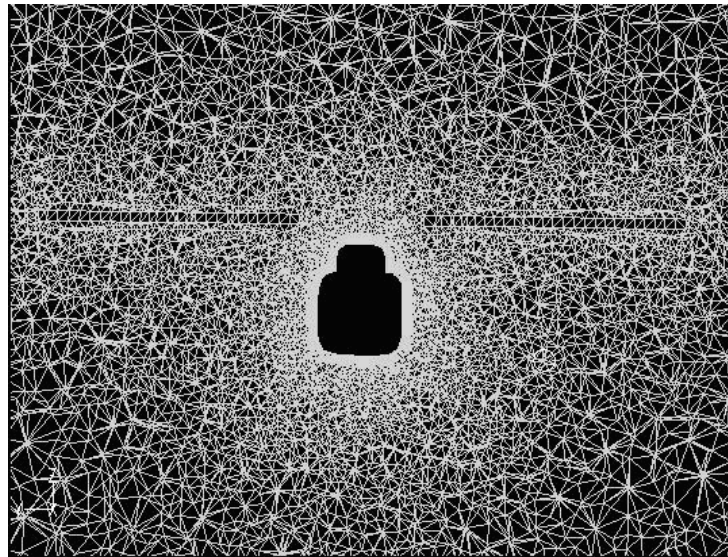


**Figure 62- Computational domain around the helicopter with boundary layer**

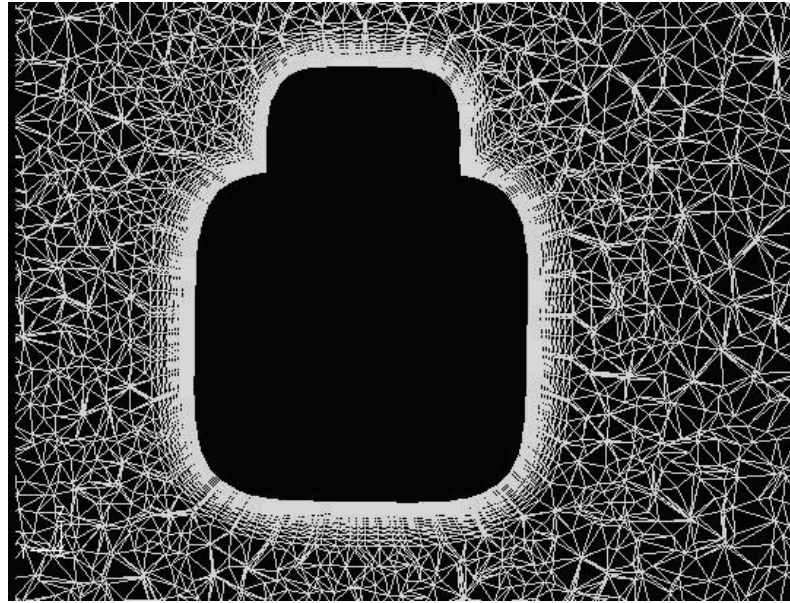


Figure 63- Boundary layers around the ROBIN geometry

## 5.4 TURBULENCE MODELS USED

As stated before various turbulence models were used for the numerical computations. A breakdown of the cases and the corresponding turbulence models used are given in the table below.

Table 7-Table of Cases

$\mu = 0.15$	Turbulence Model	Special model
Case-1	Spalart-Allmaras	
Case-2	k- $\epsilon$	Standart
Case-3	k- $\epsilon$	RNG
Case-4	k- $\epsilon$	Realizable
Case-5	k- $\omega$	Standart

## 5.5 RESULTS AND DISCUSSION

Figure 64a-e show the contours of surface pressure coefficient computed at  $\mu = 0.15$  using the turbulence models specified in the table above. Although no apparent difference is observed between the pressure contours in these figures, it will be more useful to compare along certain cuts on the geometry to experimental data.

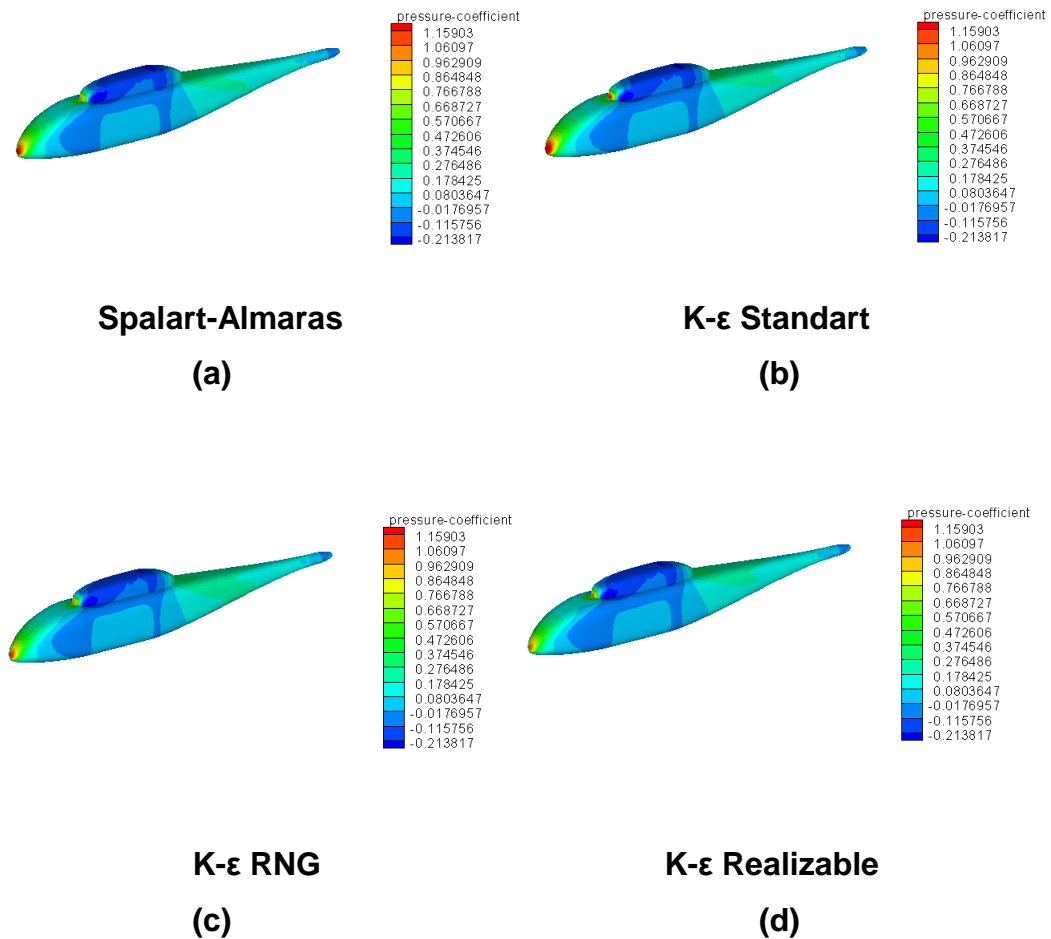
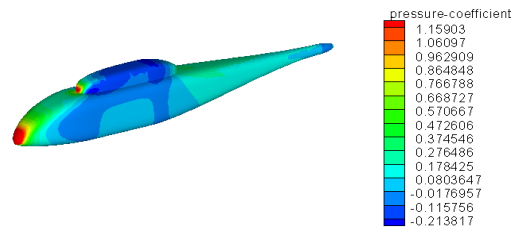


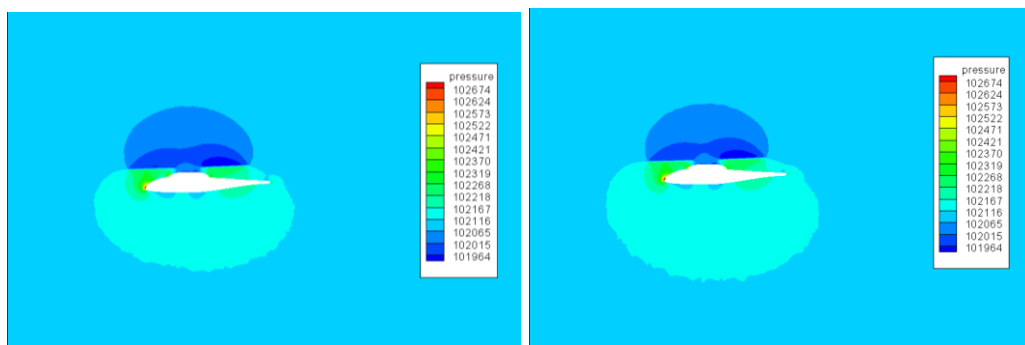
Figure 64- Value of pressure coefficient on geometry obtained from various turbulence models at  $\mu = 0.15$



**K- $\omega$**   
**(e)**

**Figure 64 (Continued)- Value of pressure coefficient on geometry obtained from various turbulence models at  $\mu = 0.15$**

Figure 65a-e show the values of pressure on the surface at constant  $Y=0$  m section. All turbulence models seem to have predicted the pressure on helicopter fuselage due to the main rotor equally well. From these contours how the main rotor affects pressure distribution around the fuselage can be visualized. There exists a pressure increase at the nose of the fuselage due to stagnation of main rotor wake over that region. Furthermore main rotor wake and airframe interaction causes pressure increase at the tail boom region. Figure 66 shows body shear stress lines for ROBIN geometry.



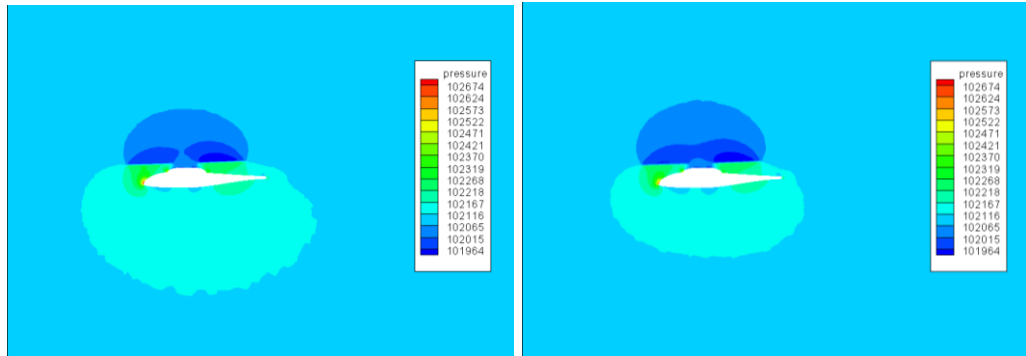
**Spalart-Almaras**

**(a)**

**K- $\epsilon$  Standart**

**(b)**

**Figure 65- Value of Pressure on surface at  $Y=0$  m at  $\mu = 0.15$**

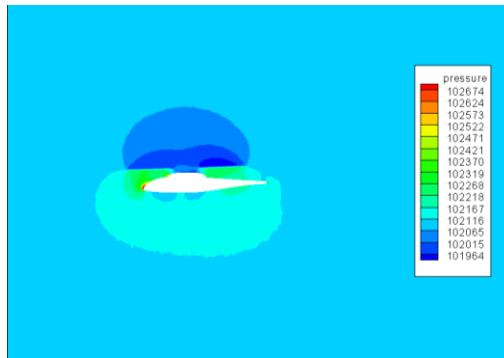


**K-ε RNG**

**(c)**

**K-ε Realizable**

**(d)**



**K-ω**  
**(e)**

Figure 65 (Continued)- Value of Pressure on surface at  $Y=0$  m at  $\mu = 0.15$

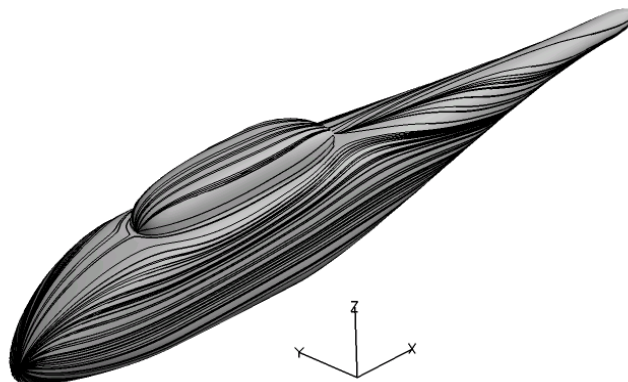


Figure 66- Body shear stress lines for ROBIN geometry

After the cross comparison of the pressure results yielded by the turbulence models used, comparison between the computed pressure coefficients and the experimental data which was taken from the wind tunnel tests [9], [5] can now be compared. Figure 67 shows the constant x-stations at which pressure data were acquired. Figure 68 to Figure 81 show the comparison of the computed pressure coefficients at these stations with the experimental data. Red colored data line corresponds to the left side of the fuselage while the black one corresponds to the right side. According to the comparisons presented in these figures, the  $k-\omega$  turbulence model does not seem to predict the flow features on the geometry at all. In the front region of the helicopter  $k-\varepsilon$  realizable turbulence model seem to yield closer results to the experimental data than the other turbulence models. However, toward the back part of the helicopter, none of the turbulence models captured the effect of the flow efficiently. One reason for the differences at the downstream stations could be the support strut not being modeled by the computations. One other reason could be that the turbulence models lacked accuracy in resolving the vortices coming from the main rotor tips, and the flow separation on the fuselage.

Figure 82 shows the stations marked with the turbulence models that gave relatively the best results there. It is evident from the comparisons spanning all the stations shown in this figure that the  $k-\varepsilon$  realizable turbulence model gave the most satisfactory comparisons among the all turbulence models, and, therefore, it is concluded that this model is the most suitable to the geometries of this type.

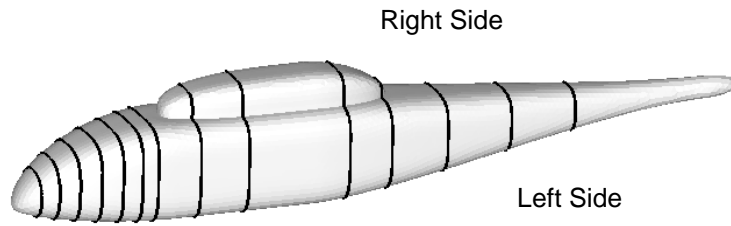


Figure 67- Pressure orifices located on ROBIN body

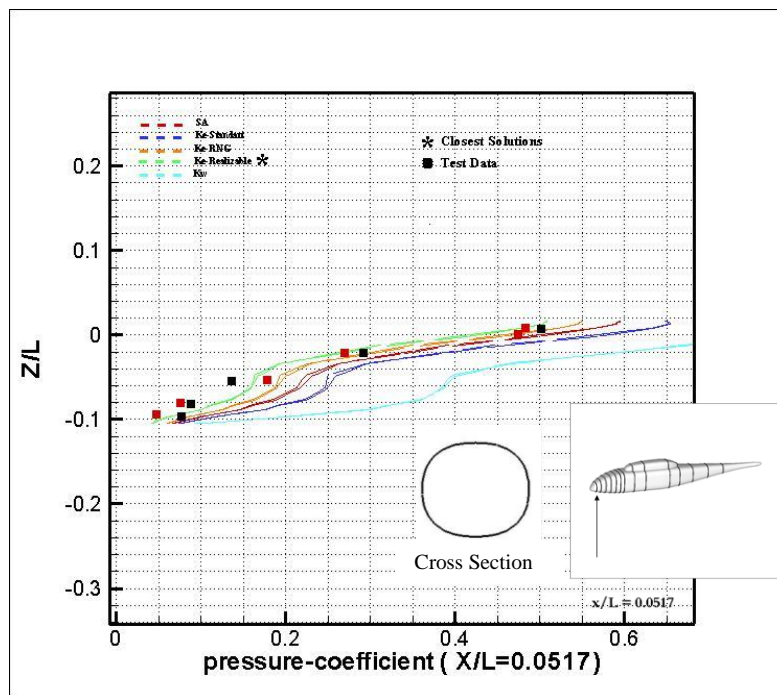


Figure 68-Comparison between test data and pressure coefficient on ROBIN surface at  $X/L=0.0517$

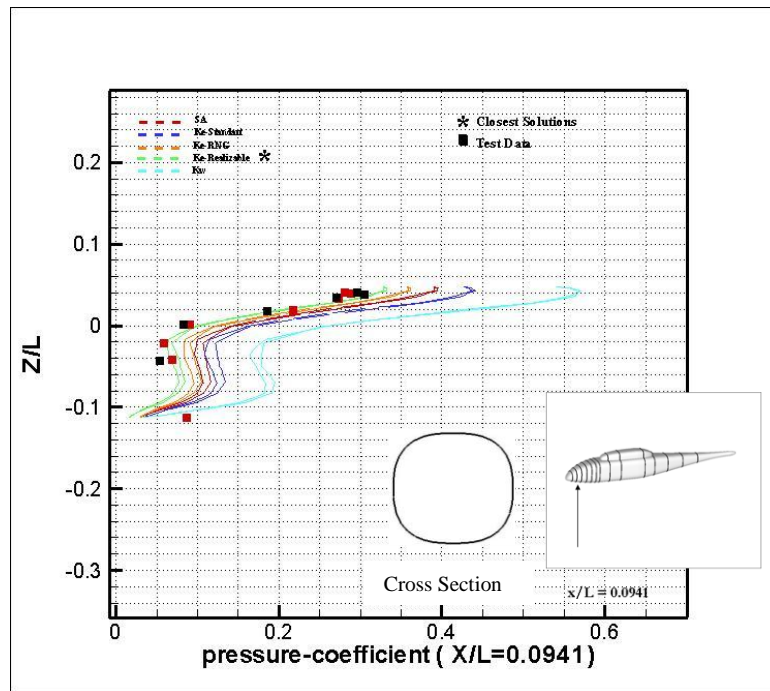


Figure 69-Comparison between test data and pressure coefficient on ROBIN surface at  $X/L=0.0941$

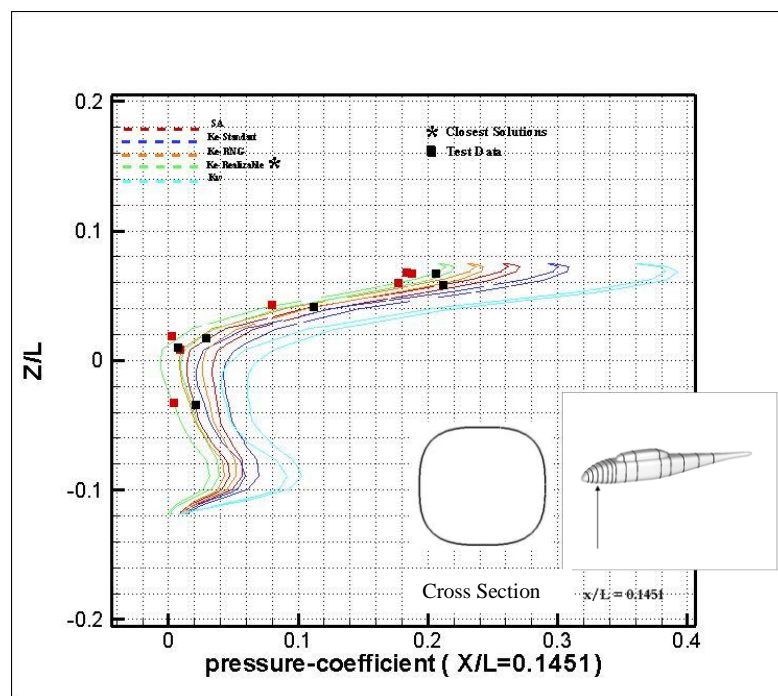


Figure 70-Comparison between test data and pressure coefficient on ROBIN surface at  $X/L=0.1451$

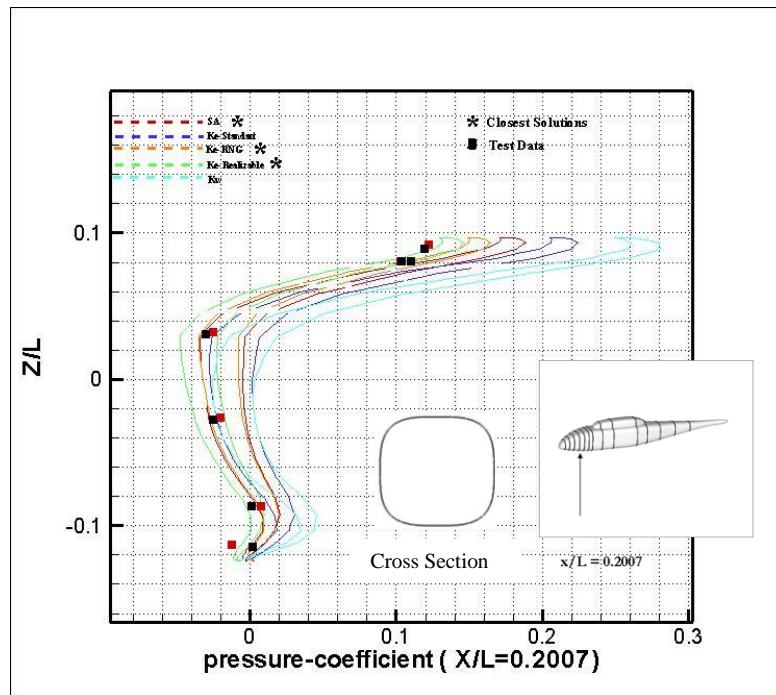


Figure 71- Comparison between test data and pressure coefficient on ROBIN surface at  $X/L=0.2007$

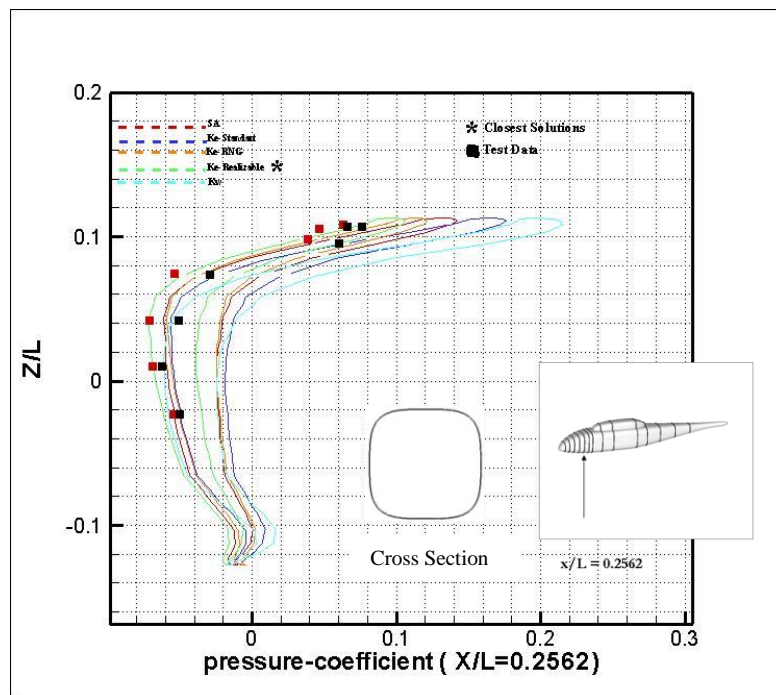


Figure 72-Comparison between test data and pressure coefficient on ROBIN surface at  $X/L=0.2562$

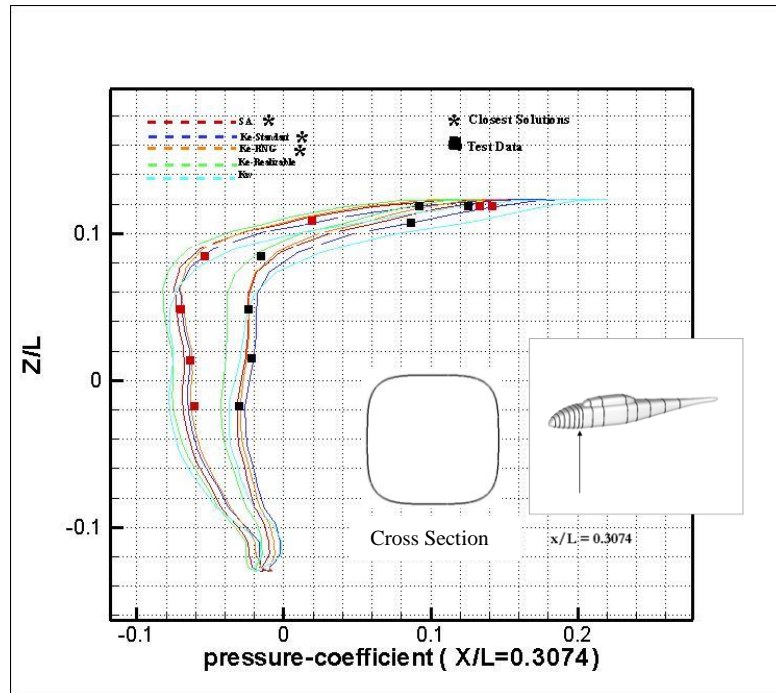


Figure 73- Comparison between test data and pressure coefficient on ROBIN surface at  $X/L=0.3074$

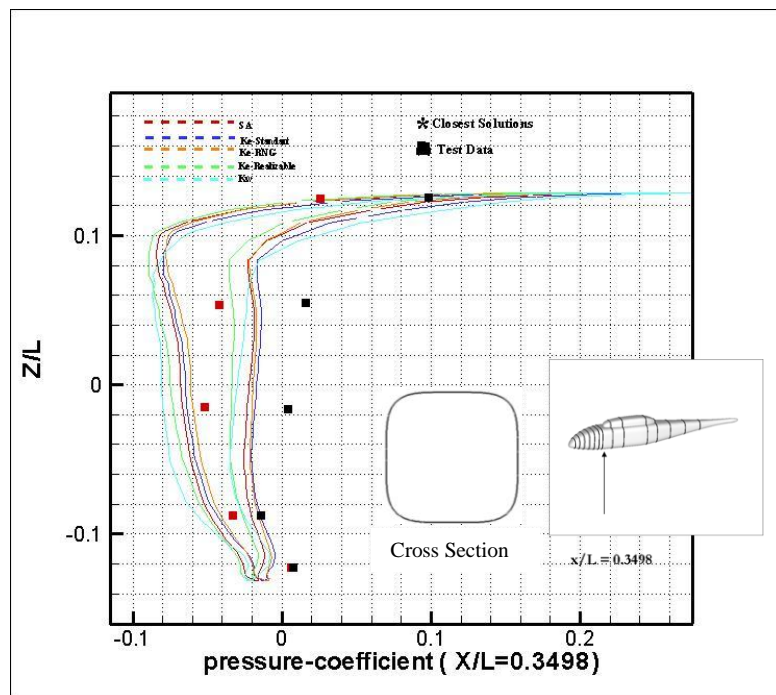


Figure 74- Comparison between test data and pressure coefficient on ROBIN surface at  $X/L=0.3498$

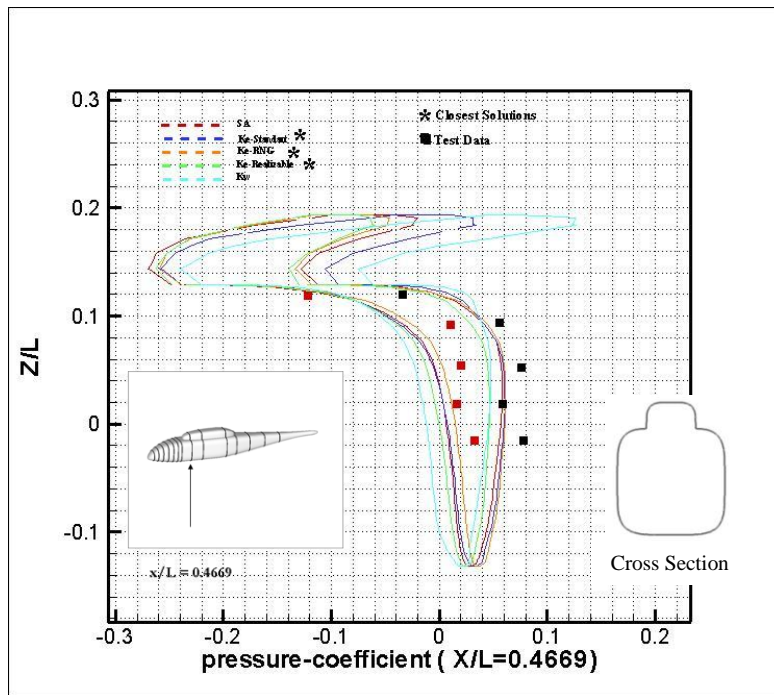


Figure 75- Comparison between test data and pressure coefficient on ROBIN surface at  $X/L=0.4669$

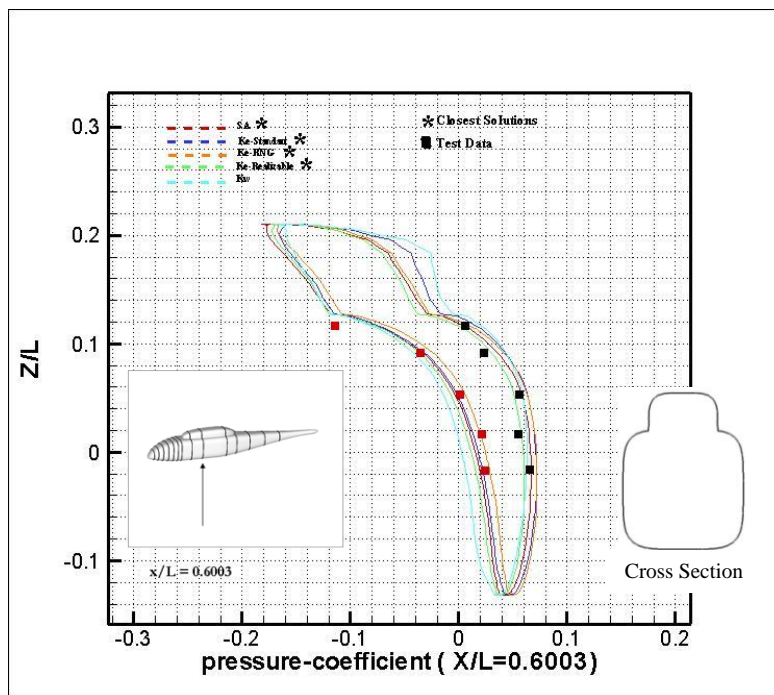


Figure 76- Comparison between test data and pressure coefficient on ROBIN surface at  $X/L=0.6003$

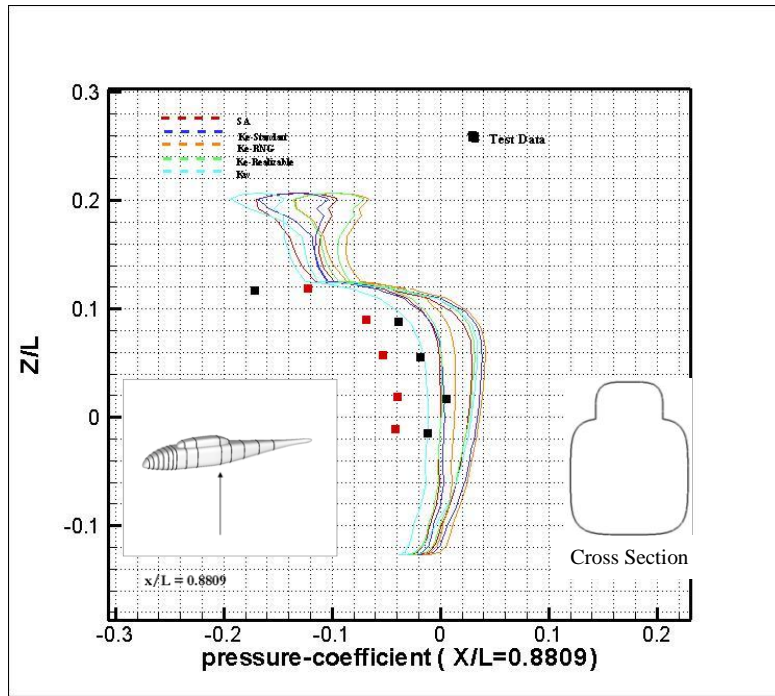


Figure 77- Comparison between test data and pressure coefficient on ROBIN surface at  $X/L=0.8809$

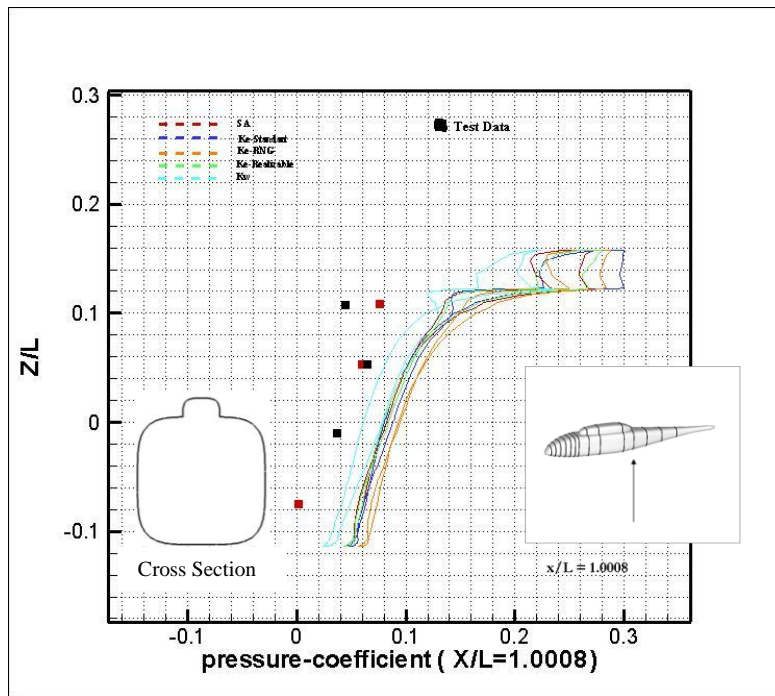


Figure 78- Comparison between test data and pressure coefficient on ROBIN surface at  $X/L=1.0008$

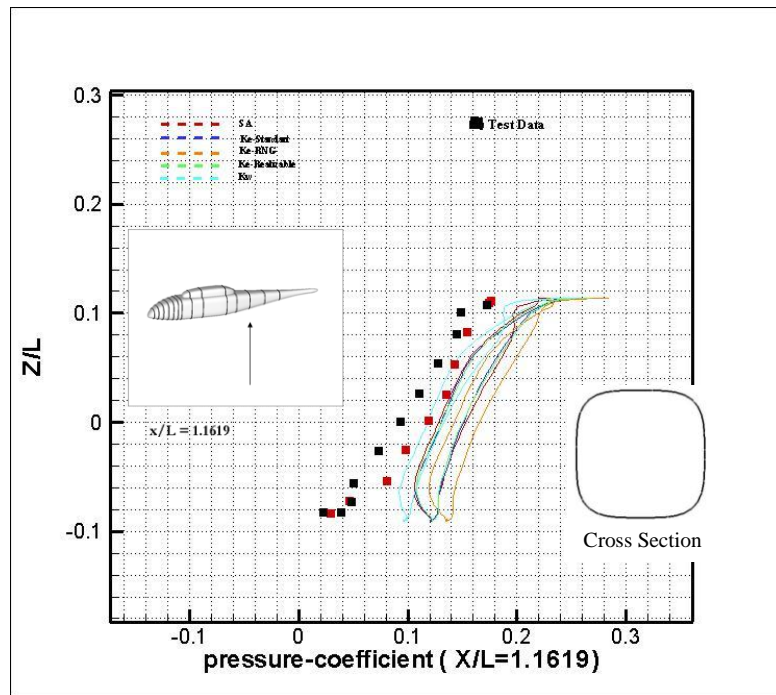


Figure 79- Comparison between test data and pressure coefficient on ROBIN surface at  $X/L=1.1619$

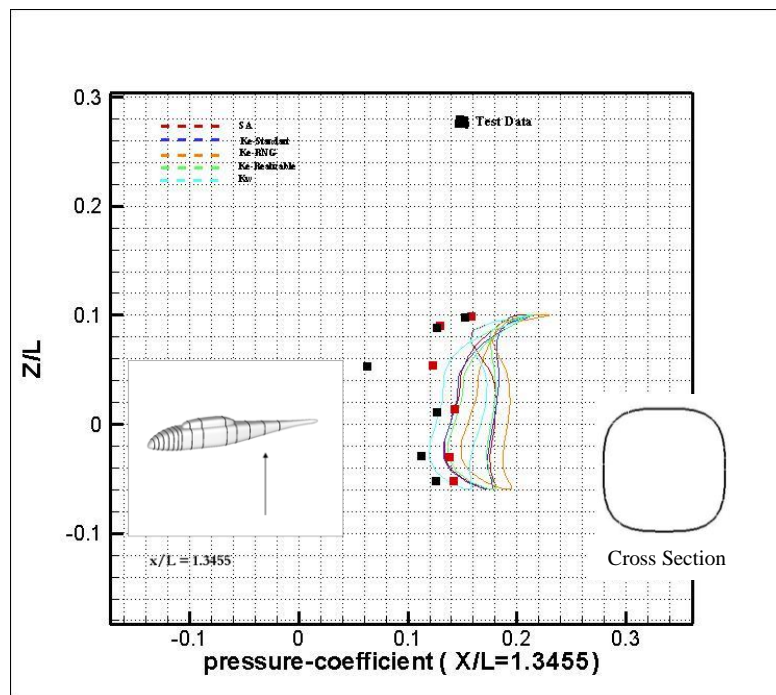


Figure 80- Comparison between test data and pressure coefficient on ROBIN surface at  $X/L=1.3455$

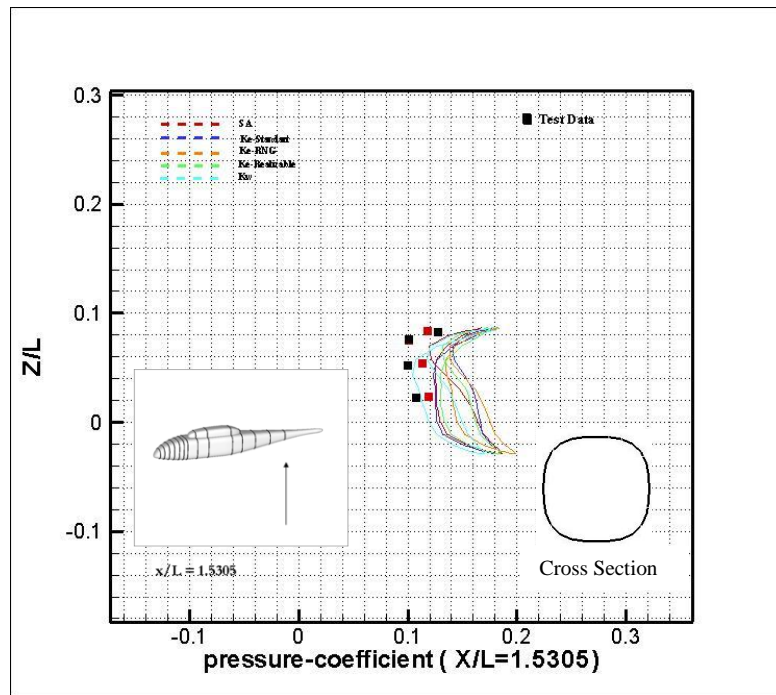


Figure 81- Comparison between test data and pressure coefficient on ROBIN surface at  $X/L=1.5305$

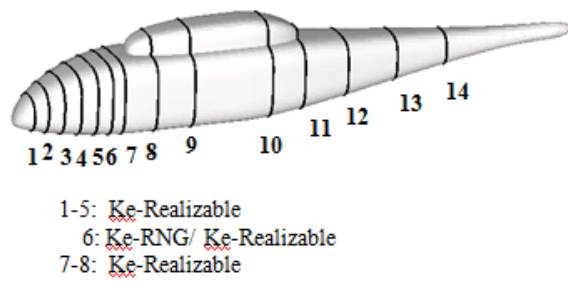


Figure 82- Model that gives closest results to test data at different faces at  $\mu = 0.15$

## CHAPTER 6

### RESULTS AND COMPARISON TO FLIGHT TESTS

Since in the simulations it was impossible to model the actual number of chaff particles, which in reality approaches 5.5 million, a limited number of particles was ejected. The particles were assumed to be released from a surface in the domain, and the number of particles that could be ejected during the simulations was a function of the underlying mesh on this surface. When the particle release surface was chosen to be a surface out of the actual chaff particle positions shortly after a firing, this corresponded to early stages of chaff dispersion, which is dominated by the so-called birdnesting phenomena, and hence in early stages, the chaff release surface was very small. Therefore, in the present analyses the number of modeled chaff particles ranged only from 100 to 600. As time passes, chaff particles disperse in a larger region, and therefore, a larger surface could be used as an initial boundary. This enabled us to model higher number of particles.

Although three chaff firings were performed during the flight tests, for the thesis study a total of eight sets of numerical computations for the chaff particle dispersion were carried out. The extra computations were done to investigate the effects of chaff particle mass, time step size, and initial chaff positions on the chaff cloud formations. In all the cases, the computed chaff distributions were compared with those reconstructed from the images taken during the flight tests.

The growth of initial surfaces can be seen in Chapter-3. All analyses were carried out at a forward flight velocity of 100 Knot. According to the results

that were obtained from the ROBIN validation test case study presented in the previous chapter, the  $k-\varepsilon$  realizable turbulence model was used also in the chaff particle dispersion simulations. Furthermore as discussed in Chapter-4, two different injection types were used. For the surface injection type, velocity components of all particles were set equal to each other. However, according to the experimental test data, the velocities were not equal. Therefore, to understand the effect of nonuniform velocity distribution in the initial surface, distributed particle velocity was used. In this injection type, all individual particle velocities were modeled separately.

As was discussed in Chapter-3, particles were tracked out from four different locations in an initial cross section. These locations corresponded to almost the outermost left, outermost right, top and bottom regions of a cross section of a chaff cloud. Figure 83 depicts an example chaff cloud cross section with the tracked chaff particles marked.

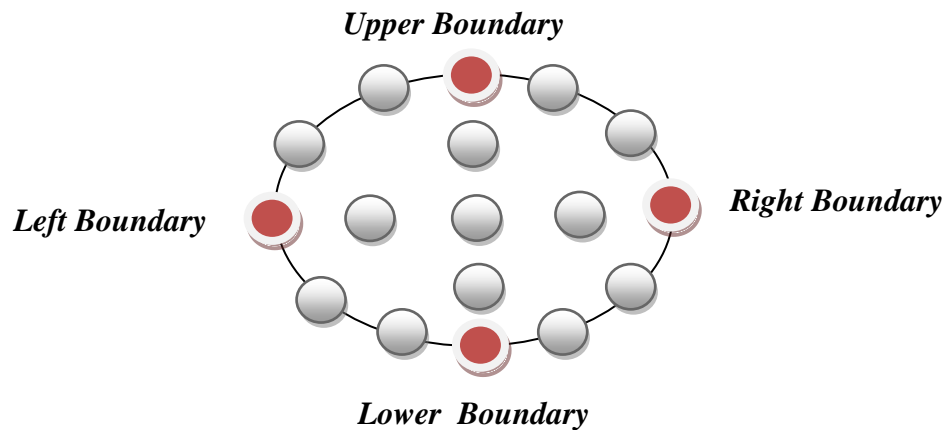


**Figure 83- Example of particle tracked locations (viewed from flow direction)**

In order to obtain an individual particle velocity value at any position on the chaff release surface, an interpolation procedure was used. Since the

problem was 3-D, equations were redefined for the three velocity components as follows

$$u(x, y, z) = a_1xyz + a_2xy + a_3xz + a_4yz + a_5x + a_6y + a_7z + a_8 \quad (35)$$

$$v(x, y, z) = b_1xyz + b_2xy + b_3xz + b_4yz + b_5x + b_6y + b_7z + b_8 \quad (36)$$

$$w(x, y, z) = c_1xyz + c_2xy + c_3xz + c_4yz + c_5x + c_6y + c_7z + c_8 \quad (37)$$

Clearly each of these equations has a total of eight unknown constants. In order to determine these unknown constants eight positions at which the velocity values were known selected. In addition to the four tracked positions, four additional locations were taken into account by simple averaging between them. Figure 84 shows the additional locations in blue that were used during interpolation calculation.

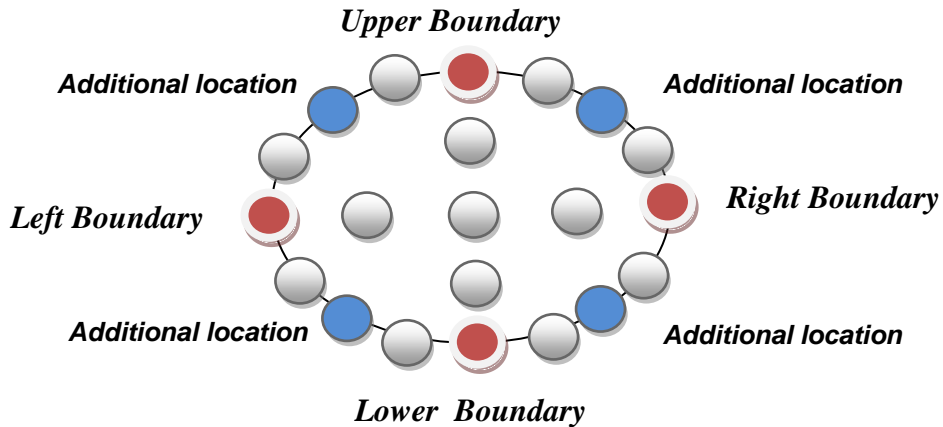


Figure 84- Locations used during interpolation (viewed from flow direction)

If a subscript is used to signify the angular positions of the discrete points, the  $u$  velocity component, for example, is given by

$$\begin{aligned}
u_0 &= a_1 x_0 y_0 z_0 + a_2 x_0 y_0 + a_3 x_0 z_0 + a_4 y_0 z_0 + a_5 x_0 + a_6 y_0 + a_7 z_0 + a_8 \\
u_{45} &= a_1 x_{45} y_{45} z_{45} + a_2 x_{45} y_{45} + a_3 x_{45} z_{45} + a_4 y_{45} z_{45} + a_5 x_{45} + a_6 y_{45} + a_7 z_{45} + a_8 \\
u_{90} &= a_1 x_{90} y_{90} z_{90} + a_2 x_{90} y_{90} + a_3 x_{90} z_{90} + a_4 y_{90} z_{90} + a_5 x_{90} + a_6 y_{90} + a_7 z_{90} + a_8 \\
u_{135} &= a_1 x_{135} y_{135} z_{135} + a_2 x_{135} y_{135} + a_3 x_{135} z_{135} + a_4 y_{135} z_{135} + a_5 x_{135} + a_6 y_{135} + a_7 z_{135} + a_8 \\
u_{180} &= a_1 x_{180} y_{180} z_{180} + a_2 x_{180} y_{180} + a_3 x_{180} z_{180} + a_4 y_{180} z_{180} + a_5 x_{180} + a_6 y_{180} + a_7 z_{180} + a_8 \\
u_{225} &= a_1 x_{225} y_{225} z_{225} + a_2 x_{225} y_{225} + a_3 x_{225} z_{225} + a_4 y_{225} z_{225} + a_5 x_{225} + a_6 y_{225} + a_7 z_{225} + a_8 \\
u_{270} &= a_1 x_{270} y_{270} z_{270} + a_2 x_{270} y_{270} + a_3 x_{270} z_{270} + a_4 y_{270} z_{270} + a_5 x_{270} + a_6 y_{270} + a_7 z_{270} + a_8 \\
u_{315} &= a_1 x_{315} y_{315} z_{315} + a_2 x_{315} y_{315} + a_3 x_{315} z_{315} + a_4 y_{315} z_{315} + a_5 x_{315} + a_6 y_{315} + a_7 z_{315} + a_8
\end{aligned}$$

In a matrix form,

$$\begin{bmatrix} u_0 \\ u_{45} \\ u_{90} \\ u_{135} \\ u_{180} \\ u_{225} \\ u_{270} \\ u_{315} \end{bmatrix} = \begin{bmatrix} x_0 y_0 z_0 & x_0 y_0 & x_0 z_0 & y_0 z_0 & x_0 & y_0 & z_0 & 1 \\ x_{45} y_{45} z_{45} & x_{45} y_{45} & x_{45} z_{45} & y_{45} z_{45} & x_{45} & y_{45} & z_{45} & 1 \\ x_{90} y_{90} z_{90} & x_{90} y_{90} & x_{90} z_{90} & y_{90} z_{90} & x_{90} & y_{90} & z_{90} & 1 \\ x_{135} y_{135} z_{135} & x_{135} y_{135} & x_{135} z_{135} & y_{135} z_{135} & x_{135} & y_{135} & z_{135} & 1 \\ x_{180} y_{180} z_{180} & x_{180} y_{180} & x_{180} z_{180} & y_{180} z_{180} & x_{180} & y_{180} & z_{180} & 1 \\ x_{225} y_{225} z_{225} & x_{225} y_{225} & x_{225} z_{225} & y_{225} z_{225} & x_{225} & y_{225} & z_{225} & 1 \\ x_{270} y_{270} z_{270} & x_{270} y_{270} & x_{270} z_{270} & y_{270} z_{270} & x_{270} & y_{270} & z_{270} & 1 \\ x_{315} y_{315} z_{315} & x_{315} y_{315} & x_{315} z_{315} & y_{315} z_{315} & x_{315} & y_{315} & z_{315} & 1 \end{bmatrix} \begin{bmatrix} a_1 \\ a_2 \\ a_3 \\ a_4 \\ a_5 \\ a_6 \\ a_7 \\ a_8 \end{bmatrix} \quad (38)$$

After inverting this equation of system, and substituting the chaff particle coordinates at the releasing point, the velocity component  $u$  can be obtained.

Overall the helicopter model used in the CFD analyses is shown with the main and tail rotors in Figure 85. At 100 Knot, downwash of the main rotor goes towards the back side of the helicopter. Figure 86 shows the computed flow around the helicopter. Flow up to helicopter geometry remains smooth, but after it faces the main rotor and helicopter geometry, flow becomes mixed. Figure 87 shows the main and tail rotor interaction. Flow coming from the main rotor affects both the tail rotor and the tail boom.

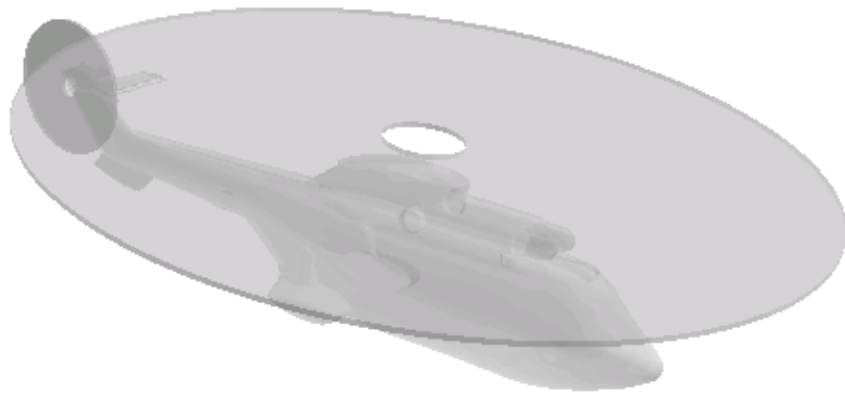


**Figure 85- Helicopter model with main and tail rotor**

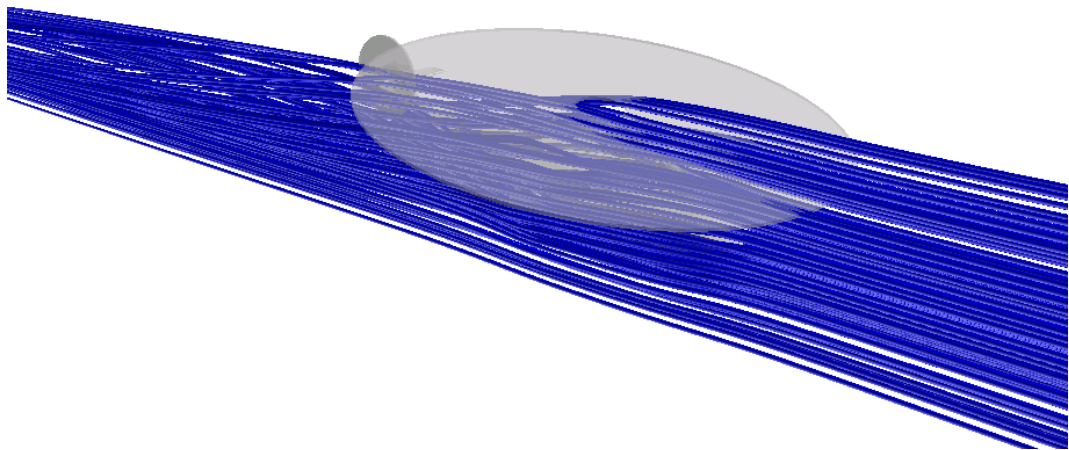


**Figure 86- Flow around a helicopter geometry**

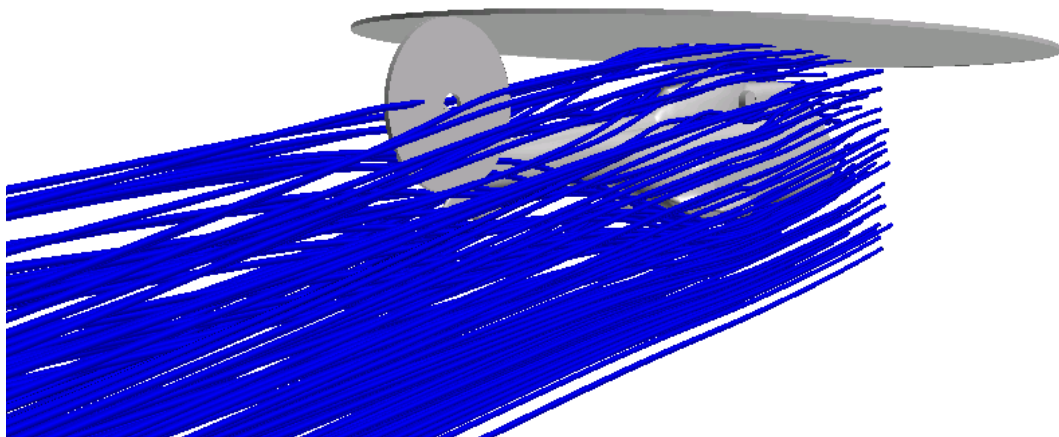


**Figure 87- Main and tail rotor interactions**

Figure 88 and Figure 89 show the main rotor streamlines where the effects can be clearly observed.



**Figure 88-Main rotor streamlines and tip effect, forward view**

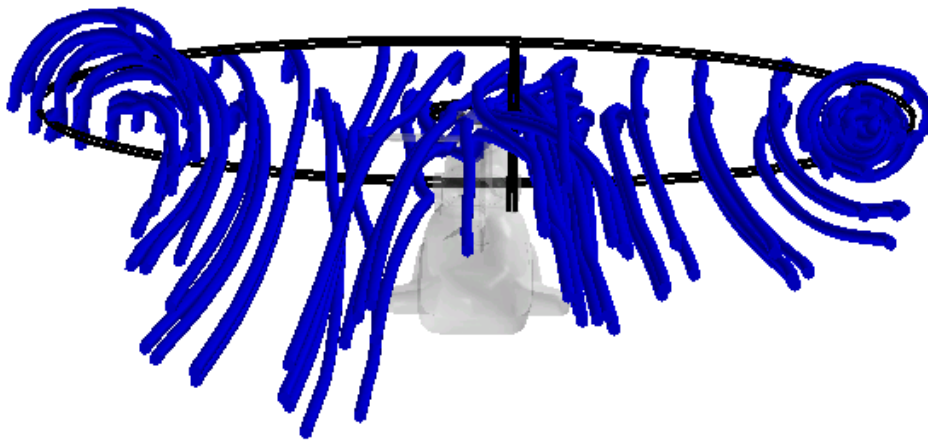


**Figure 89- Main rotor streamlines and tip effect, rear view**

## **6.1 ANALYSES OF FIRST FIRING**

Results pertaining to the first firing are presented below. These results were obtained using two different initial surfaces constructed out of the chaff particle positions after 100 ms from the flight test firing with uniform initial particle velocities and formed after 288 ms with linearly varying particle velocities.

The reason of using two different surfaces and two different injection types (particle velocity distributions) in the chaff particle injection process was to understand their effects on the spatial evolution of the particles in the flow field.

### **6.1.1 INITIAL SURFACE I AND UNIFORM PARTICLE VELOCITY**

In this section, the results obtained with a particle ejection surface constructed out of the chaff particle positions after 100 ms from the flight test firing with uniform particle velocities are presented.

Figure 90 shows the computed trajectories with an isometric view and Figure 91 shows the rear view of the trajectories. Figure 92 shows the top view and Figure 93 shows the side view of the simulated trajectories. Also the flow streamlines going through the initial chaff particle surface is displayed in Figure 94. It is evident from all these figures that there are significant differences between the computed trajectories of the particles and the flight test data. It is clear that when the particles are released, they start going downstream with the flow in the numerical simulation, whereas in the experimentally obtained chaff cloud particles seem to go sideways as they get dispersed. It is also observed in the flight test data that because of the birdnesting effects the particles stick together for a while after the firing.

This causes the whole chaff bundle to travel in the direction of firing for some time. This may be the main source of the differences between the computed trajectories and the actual ones. It is also observed that the computed dispersion of the particles has a radially uniform pattern, while in the flight test the dispersion had an elliptical pattern. This may be due to the applied uniform velocity boundary condition. Although not necessarily all the particles in the tests had the same velocity. The effects of this will be studied in later computations.

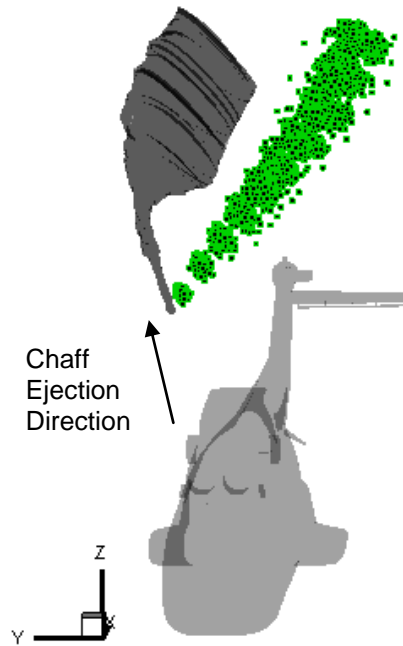


**Figure 90- Trajectory analysis of first firing from initial surface at 100ms, isometric view**

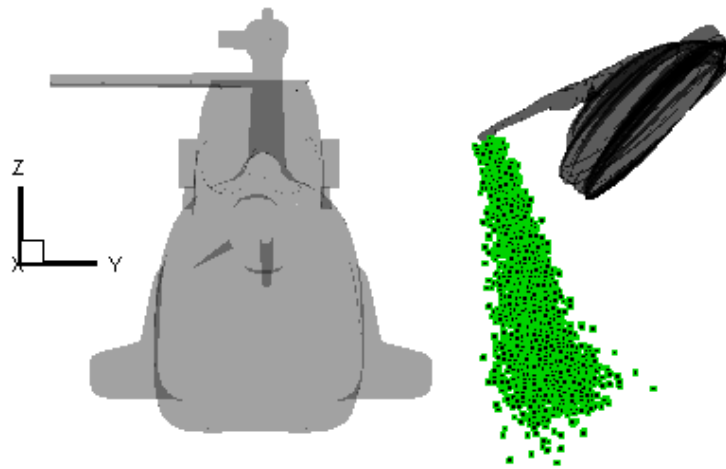


Figure 91- Trajectory analysis of first firing from initial surface at 100ms, rear view

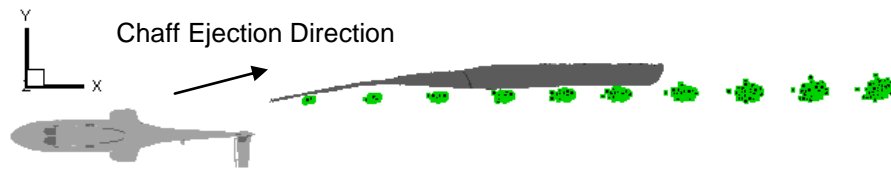


Figure 92- Trajectory analysis of first firing from initial surface at 100ms, top view

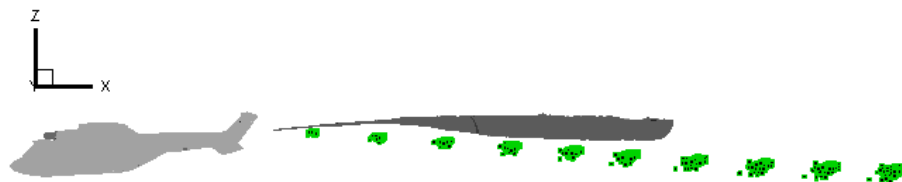


Figure 93- Trajectory analysis of first firing from initial surface at 100ms, side view

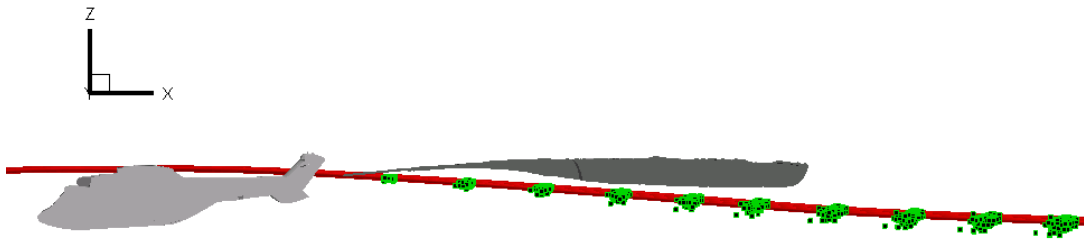


Figure 94- Streamlines from initial surface at 100ms, side view

### 6.1.2 INITIAL SURFACE II AND LINEARLY VARYING PARTICLE VELOCITY

In the second set of computations, chaff particles were ejected from a surface which was formed after 288 ms after the firing during the flight test. For the analysis distributed particle velocity was used as an injection. According to this type, all particles have different initial velocities. The used velocity distribution of the particles is shown in Figure 95. This distribution was obtained employing the interpolation method described above.

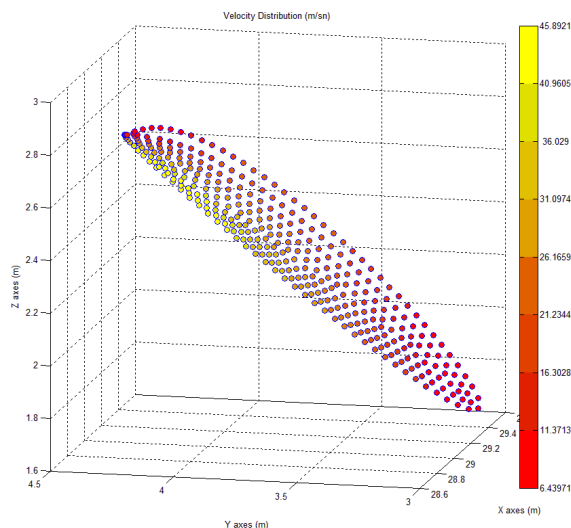
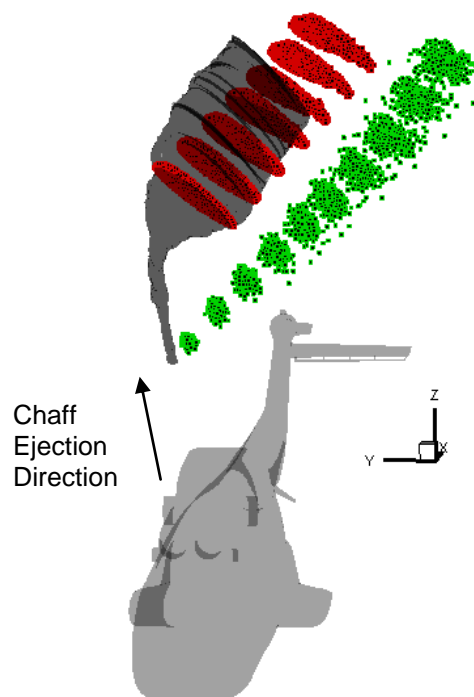


Figure 95-Particle velocity distribution at initial surface (288ms)

Figure 96 and Figure 97 show the predicted trajectories from isometric and rear views, while Figure 98 and Figure 99 show the trajectory results from top and side views. Figure 100 shows the streamlines that were passing through initial surface. In these figures green particles represent initial particles ejected from a surface which was formed after 100 ms with uniform particle velocities and red particles represent initial particles ejected from a surface which was formed after 288 ms with distributed particle velocities. According to these results, second computation exhibit more meaningful results for chaff particle dispersion when compared with those of flight test. The reason for this reasonably good agreement here is the fact that the injection surface come after the birdnesting effect lost its effectiveness. Furthermore, assigning more realistic initial velocity values to the injected particles impeded the previously obtained radial dispersion, and instead, an elliptical dispersion pattern was achieved. Therefore red particles distribution resembles the actual data more than green one.



**Figure 96- Comparison of trajectory analysis between two initial surfaces, isometric view**

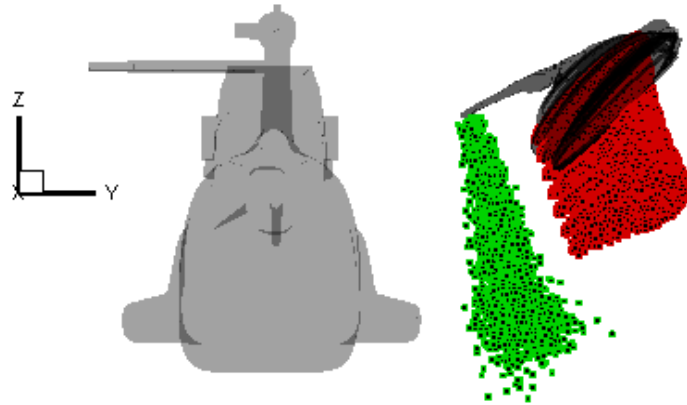


Figure 97- Comparison of trajectory analysis between two initial surfaces, rear view

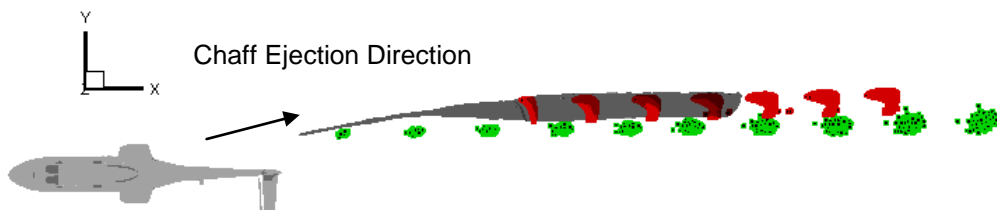


Figure 98- Comparison of trajectory analysis between two initial surfaces, top view

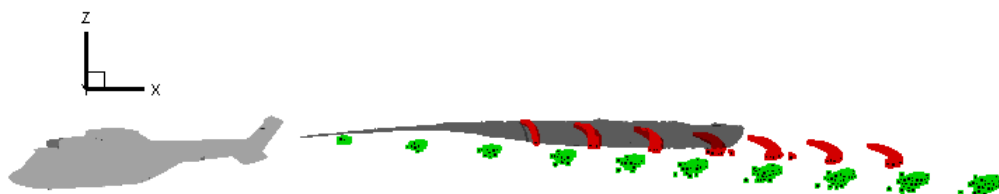


Figure 99- Comparison of trajectory analysis between two initial surfaces, side view

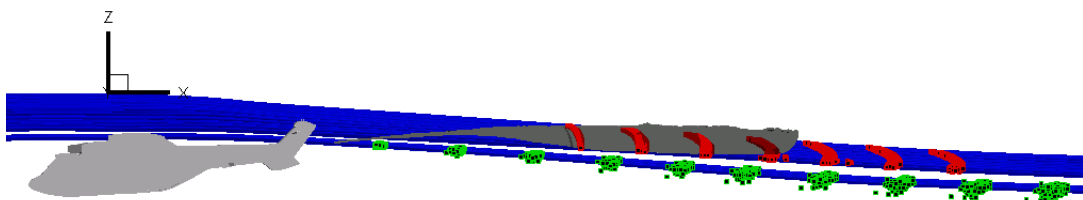


Figure 100- Streamlines from two initial surfaces, side view

## **6.2 ANALYSES OF SECOND FIRING**

Results pertaining to the second firing are presented below. These results were obtained using three different initial surfaces constructed out of the chaff particle positions after 110 ms from the flight test firing with uniform initial particle velocities, formed after 178 ms with linearly varying particle velocities and lastly formed after 245 ms with linearly varying particle velocities.

The reason of using three different surfaces and two different injection types (particle velocity distributions) in the chaff particle injection process was to understand their effects on the spatial evolution of the particles in the flow field.

### **6.2.1 INITIAL SURFACE I AND UNIFORM PARTICLE VELOCITY**

In this section, the results obtained with a particle ejection surface constructed out of the chaff particle positions after 110 ms from the flight test firing with uniform particle velocities are presented.

Figure 101 shows the computed trajectories with an isometric view and Figure 102 shows the rear view of the trajectories. Figure 103 shows the top view and Figure 104 shows the side view of the simulated trajectories. Also the flow streamlines going through the initial chaff particle surface is displayed in Figure 105.

Each chaff scattering differs from each other, because so many parameters affect this scattering characteristics. At this test, chaff particle starts to disperse earlier regarding the previous flight test data. Hence more uniform scattering was obtained. Because the region where particles were ejected

from may have under less birdnesting effect. Because of this reason, computed trajectory of particles is close to the flight test data. As in the previous computational results, the computed dispersion of particles has a radially uniform pattern. This is due to applied boundary condition.

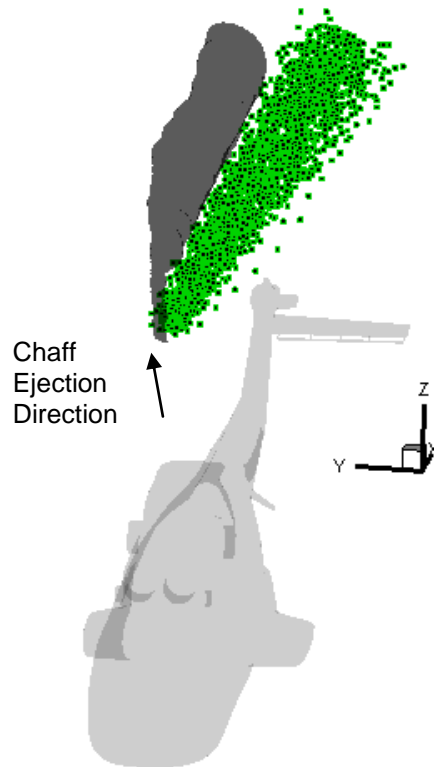


**Figure 101- Trajectory analysis of second firing from initial surface at 110ms, isometric view**

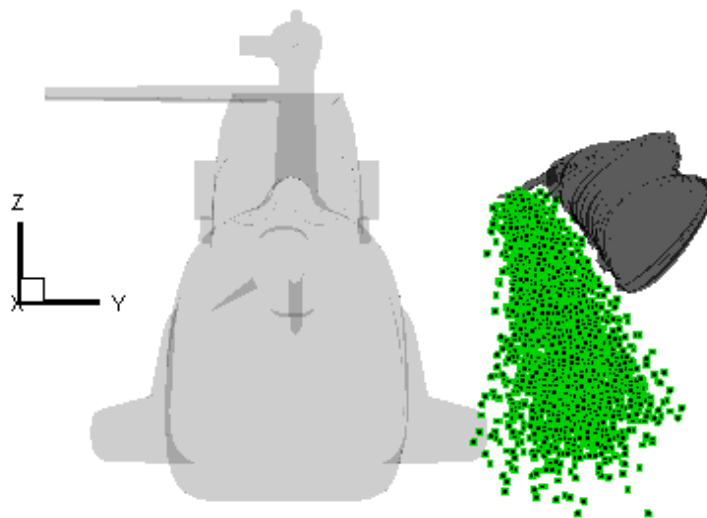


Figure 102- Trajectory analysis of second firing from initial surface at 110ms, rear view

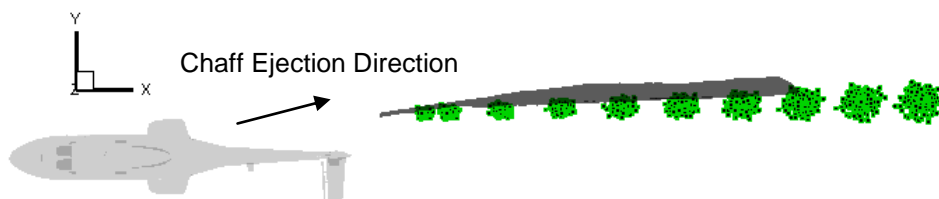


Figure 103- Trajectory analysis of second firing from initial surface at 110ms, top view

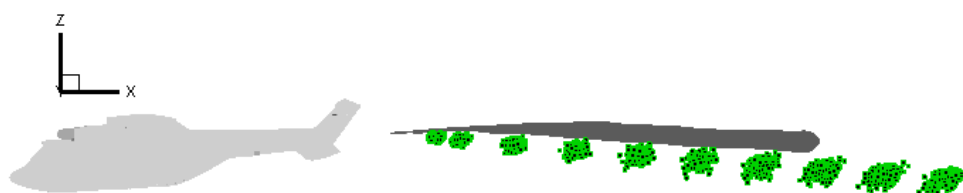


Figure 104- Trajectory analysis of second firing from initial surface at 110ms, top view

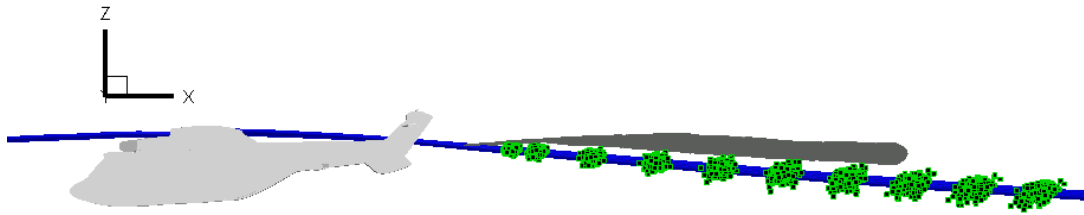


Figure 105- Streamlines from initial surface at 110ms, side view

## 6.2.2 INITIAL SURFACE II AND LINEARLY VARYING PARTICLE VELOCITY

In the second set of computations, chaff particles were ejected from a surface which was formed after 178 ms after the firing during the flight test. For the analysis distributed particle velocity was used as an injection. According to this type, all particles have different initial velocities. The used velocity distribution of the particles is shown in Figure 106.

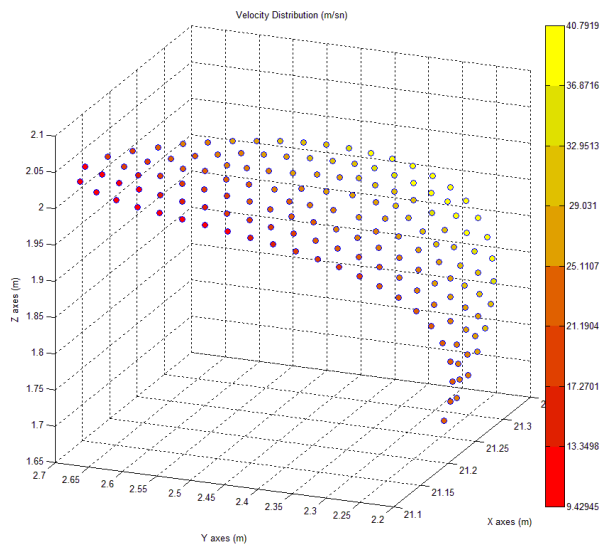
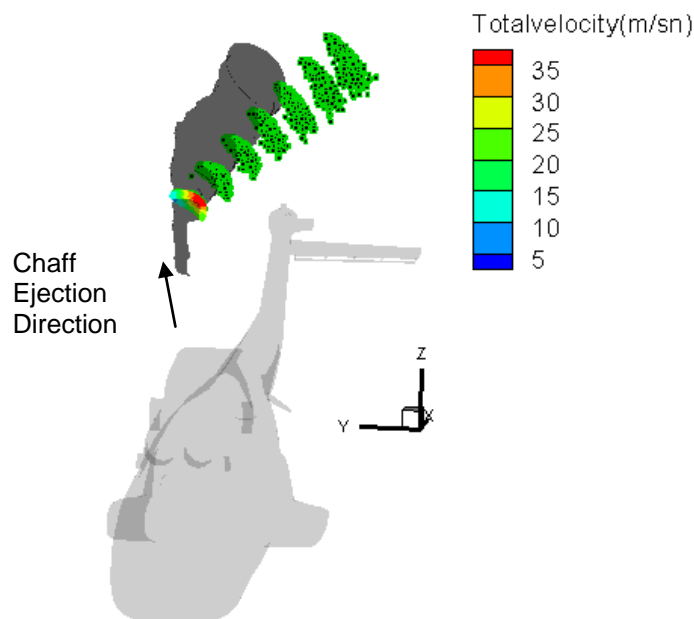


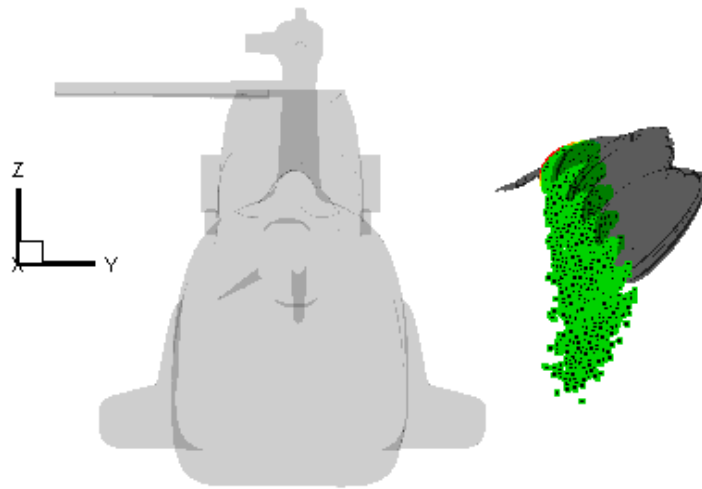
Figure 106-Particle velocity distribution at initial surface (178ms)

Figure 107 and Figure 108 show the predicted trajectories from isometric and rear views, while Figure 109 and Figure 110 show the trajectory results from top and side views. Figure 111 shows the streamlines that were passing through initial surface.

As expected from the previous trajectory results, trajectory of particles that were ejected from the surface constructed later come closer to the flight test data. As mentioned before the reason of this is birdnesting effect losses its effectiveness as time passes. Hence this surface used as an ejection region is under less birdnesting effect. Moreover affect of assigning distributed velocity values to particles is seen once more. Growth of scattering looks like an elliptical dispersion as achieved in flight tests. According to this results, particles almost travel in the chaff cloud.



**Figure 107- Trajectory analysis of second firing from initial surface at 178ms, isometric view**



**Figure 108- Trajectory analysis of second firing from initial surface at 178ms, rear view**

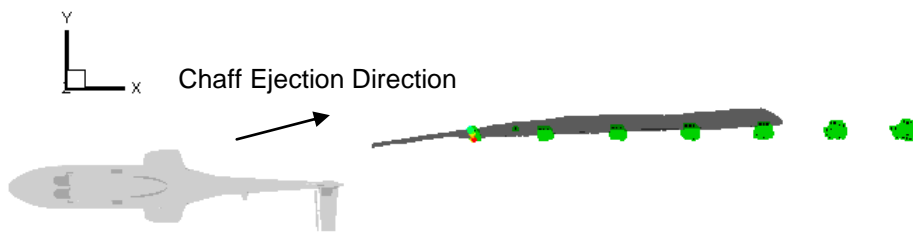


**Figure 109 Trajectory analysis of second firing from initial surface at 178ms, top view**

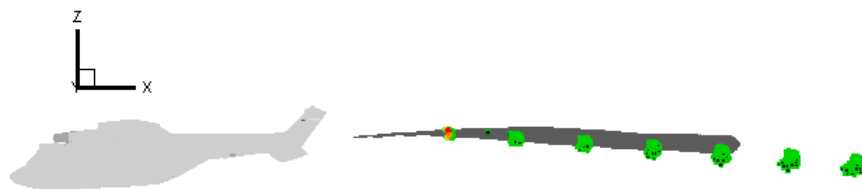


**Figure 110- Trajectory analysis of second firing from initial surface at 178ms, sideview**

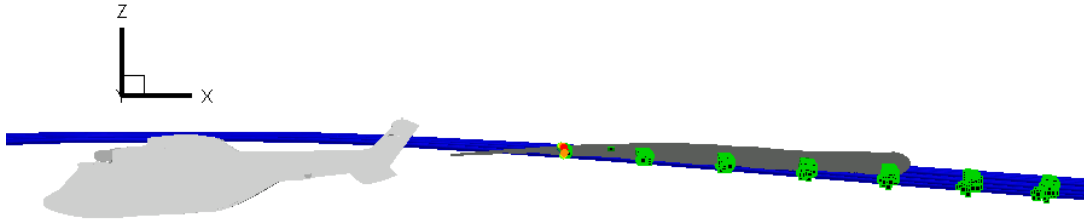


Figure 111- Streamlines from initial surface at 178ms, side view

### 6.2.3 INITIAL SURFACE III AND LINEARLY VARYING PARTICLE VELOCITY

In the third set of computations, chaff particles were ejected from a surface which was formed after 245 ms after the firing during the flight test. For the analysis distributed particle velocity was used as an injection. According to this type, all particles have different initial velocities. The used velocity distribution of the particles is shown in Figure 112.

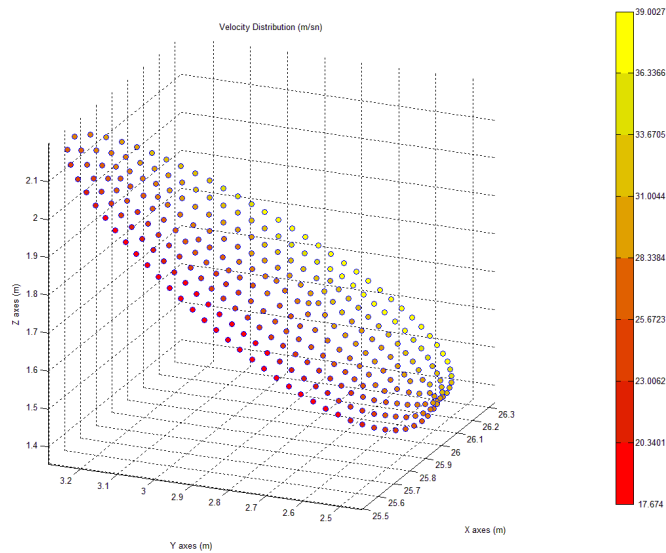


Figure 112- Particle velocity distribution at initial surface (245ms)

Figure 113 and Figure 114 show the predicted trajectories from isometric and rear views, while Figure 115 and Figure 116 show the trajectory results from top and side views. Figure 117 shows the streamlines that were passing thorough initial surface. In these figures green particles represent initial particles ejected from a surface which was formed after 110 ms with uniform particle velocities, red particles represent initial particles ejected from a surface which was formed after 178 ms with distributed particle velocities and lastly blue particles represent initial particles ejected from a surface which was formed after 245 ms with distributed particle velocities. According to these results, the third computations seem to have yielded more meaningful results for chaff particle dispersion when compared with those of flight test. According to the flight test images, after 245 ms from firing particles are commonly no longer sticks together and behave as an individual. So it is expected that, birdnesting effect plays a negligible role on chaff particle dispersion in that region. The third set of computational results also verify this phenomena. Because trajectory of blue particles almost completely travels in the chaff cloud.

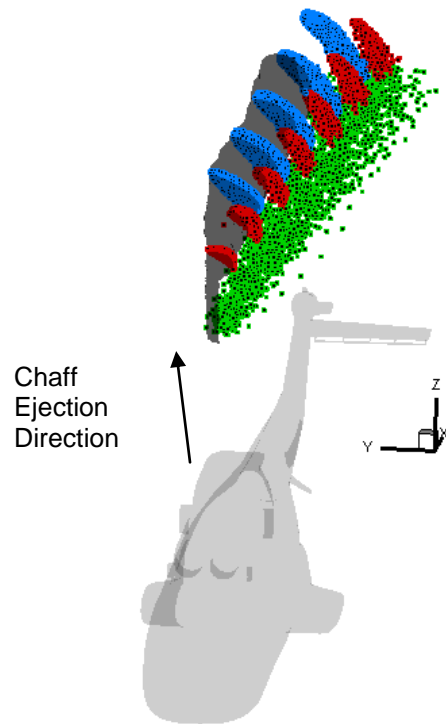


Figure 113- Comparison of trajectory analysis between three initial surfaces, isometric view

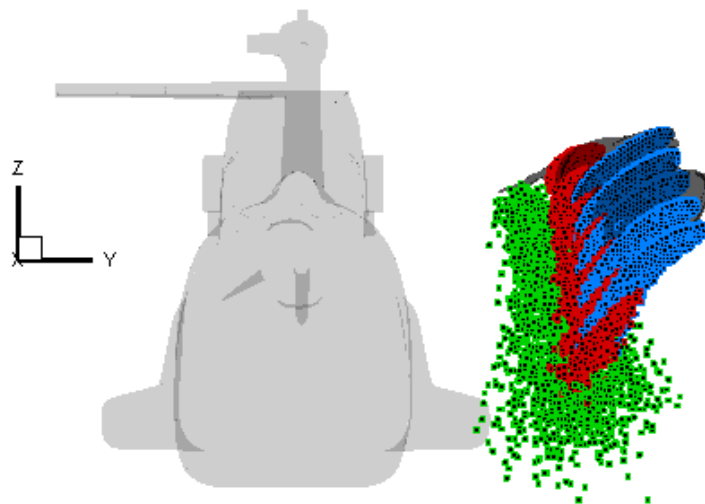


Figure 114- Comparison of trajectory analysis between three initial surfaces, rear view

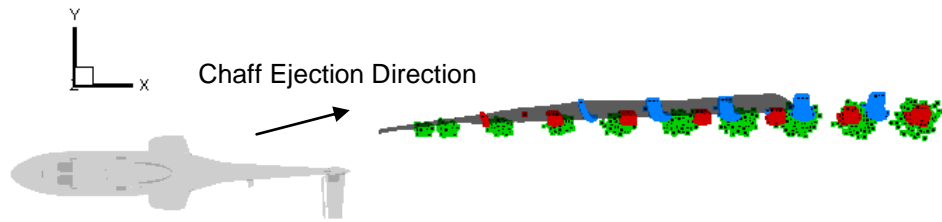


Figure 115- Comparison of trajectory analysis between three initial surfaces, top view

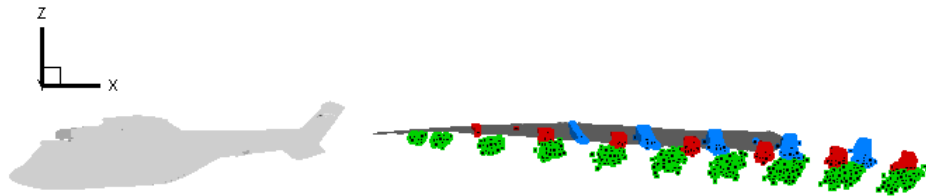


Figure 116- Comparison of trajectory analysis between three initial surfaces, side view

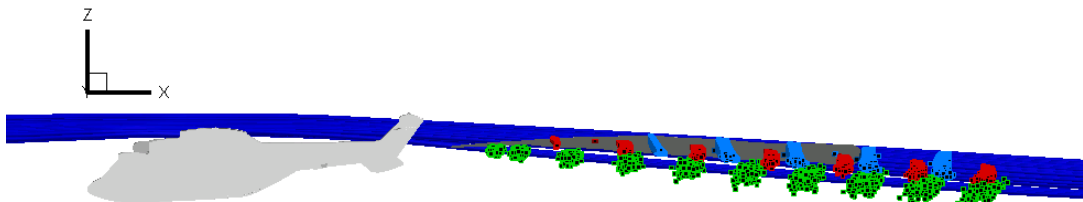


Figure 117- Streamlines from three initial surfaces, side view

### 6.3 ANALYSES OF THIRD FIRING

Results pertaining to the third firing are presented below. These results were obtained using two different initial surfaces constructed out of the chaff particle positions after 100 ms from the flight test firing with uniform initial

particle velocities and formed after 200 ms with linearly varying particle velocities.

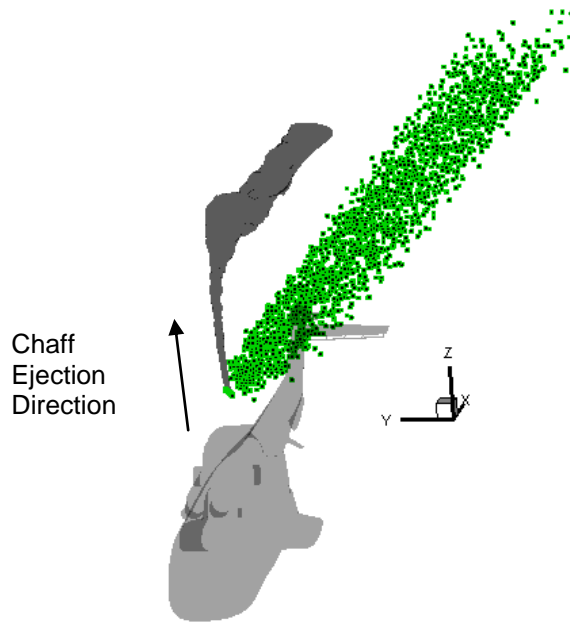
The reason of using two different surfaces and two different injection types (particle velocity distributions) in the chaff particle injection process was to understand their effects on the spatial evolution of the particles in the flow field.

### **6.3.1 INITIAL SURFACE I AND UNIFORM PARTICLE VELOCITY**

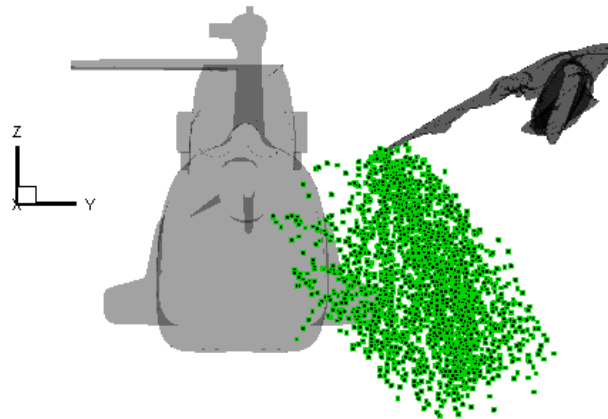
In this section, the results obtained with a particle ejection surface constructed out of the chaff particle positions after 100 ms from the flight test firing with uniform particle velocities are presented.

Figure 118 shows the computed trajectories with an isometric view and Figure 119 shows the rear view of the trajectories. Figure 120 shows the top view and Figure 121 shows the side view of the simulated trajectories. Also the flow streamlines going through the initial chaff particle surface is displayed in Figure 122.

As mentioned in section 6.2, chaff scattering differs from each other. Flight test data (scattering of chaff) for this firing is different from the other previous two ejection. In this case, chaff bundle travel more in the direction of firing regarding the previous ones. This unequal characteristics also affect radar cross section of the chaff particles. It makes prediction of chaff scattering harder. Since chaff particles start to disperse lately in this case, computational results do not suit well with the experimental data.



**Figure 118- Trajectory analysis of third firing from initial surface at 100ms, isometric view**



**Figure 119- Trajectory analysis of third firing from initial surface at 100ms, rear view**

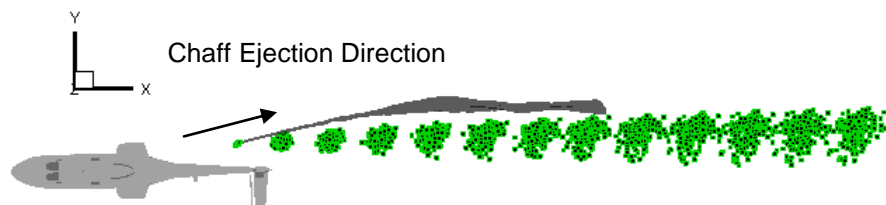


**Figure 120- Trajectory analysis of third firing from initial surface at 100ms, top view**

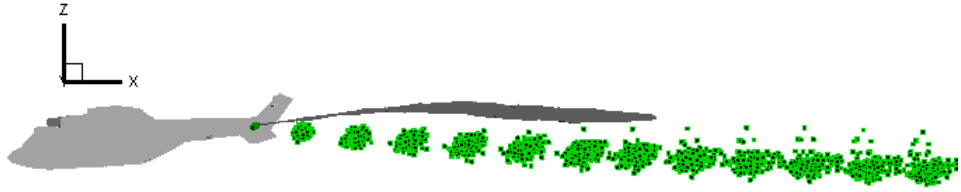


**Figure 121- Trajectory analysis of third firing from initial surface at 100ms, side view**

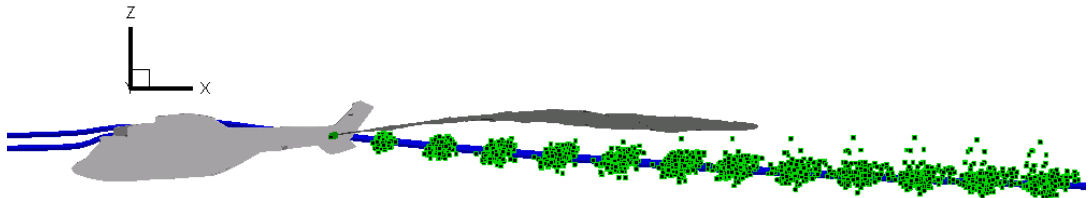


**Figure 122- Streamlines from initial surface at 100ms, isometric view**

### **6.3.2 INITIAL SURFACE II AND LINEARLY VARYING PARTICLE VELOCITY**

In the second set of computations, chaff particles were ejected from a surface which was formed after 200 ms after the firing during the flight test. For the analysis distributed particle velocity was used as an injection. According to this type, all particles have different initial velocities. The used velocity distribution of the particles is shown in Figure 123.

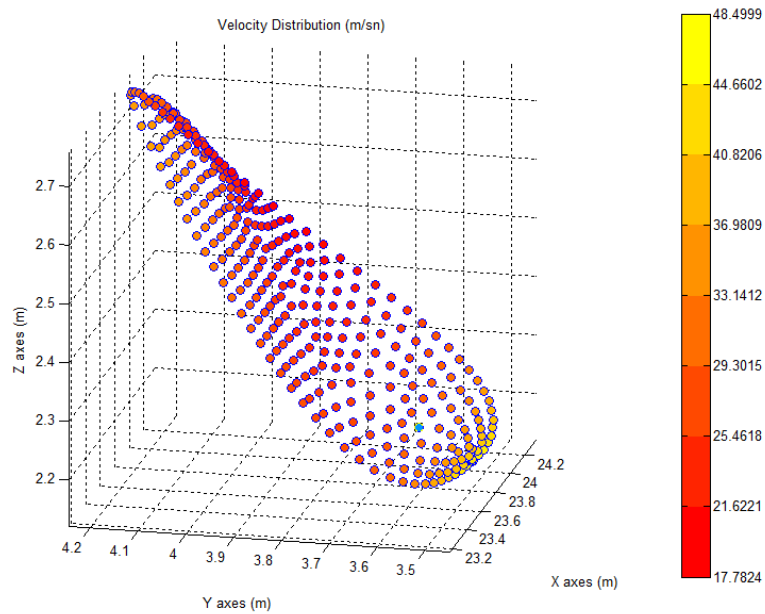


**Figure 123- Particle velocity distribution at initial surface (200ms)**

Figure 124 and Figure 125 show the predicted trajectories from isometric and rear views, while Figure 126 and Figure 127 show the trajectory results from top and side views. In these figures green particles represent initial particles ejected from a surface which was formed after 100 ms with uniform particle velocities and red particles represent initial particles ejected from a surface which was formed after 200 ms with distributed particle velocities. According to these results, the second computation has provided more meaningful results for chaff particle dispersion when compared with those of flight test. Since particles were ejected at later formed surfaces, which means it has less affected by chaff sticky phenomena, solutions get closer to the flight test data. Moreover assigning more realistic initial velocity values to the injected particles improved chaff particle distribution. Therefore red particles distribution resembles the flight test data more than green one. Hence red particles almost travel in the chaff cloud.

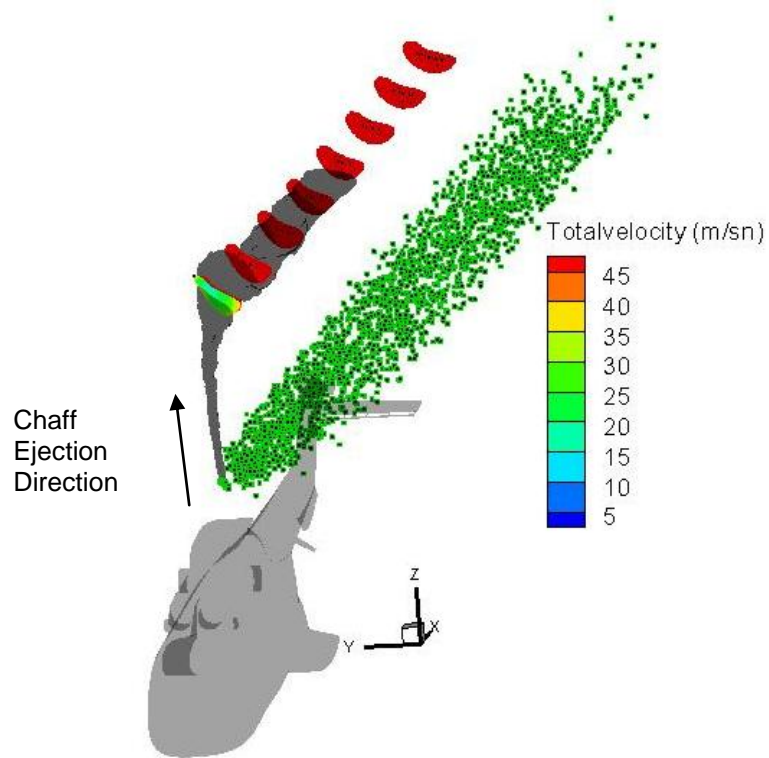
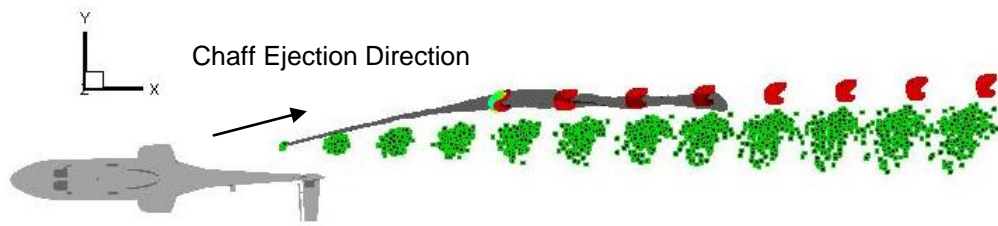


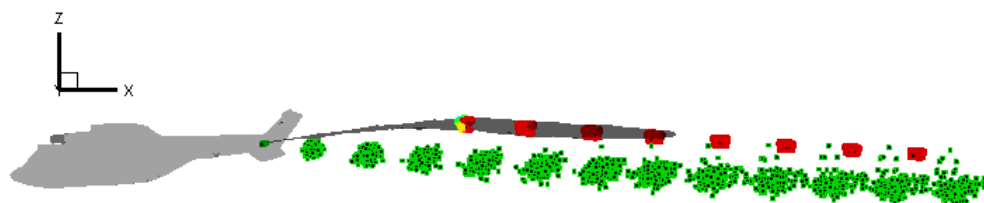
Figure 124- Comparison of trajectory analysis between two initial surfaces, isometric view



Figure 125- Comparison of trajectory analysis between three initial surfaces, rear view



**Figure 126- Comparison of trajectory analysis between three initial surfaces, top view**



**Figure 127- Comparison of trajectory analysis between three initial surfaces, side view**

## **6.4 MASS AND TIME STEP INDEPENDENCY**

The analysis regarding the mass independency contains three analyses at different particle weights. The lightest particle at the analyses is presented as green one and heaviest particle in the analyses is presented as blue. Initial condition for all three analyses are same. Blue one gets closer to the chaff cloud because of its mass density. Mass of blue particles equals to two hundred times of green particles or hundred times of red particles. The degree of mass change used at analyses and effect of this change on solutions are discussed together, it can be concluded that computational results are nearly independent of chaff particle mass in the range 1 to 200 times chaff particle weight.

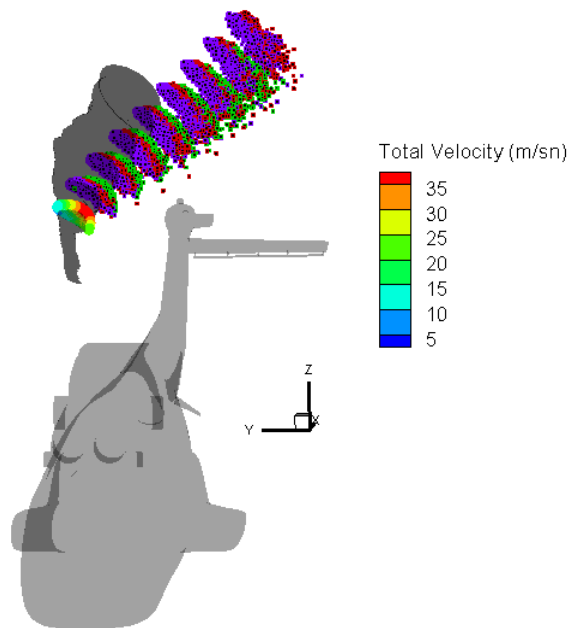


**Figure 128- Mass dependency on trajectory analysis, isometric view**

The analyses regarding the time step independency contains additional analysis with smaller time step size. Adequacy of applied time step size during analysis were checked by reanalyzing one case with five times smaller time step size and solution came out similar. Hence obtained results are insensitive to smaller time step size.

For all chaff firing analyses, in specified time duration computed chaff particle locations get close to the flight test data. Hence, an average chaff particle velocity can be calculated meaningfully by numerical solutions.

## CHAPTER 7

### CONCLUSION AND FUTURE WORK

This thesis has described trajectory computations of small solid particles in the flowfield of a medium size utility helicopter in forward flight. The computations were done using the commercial fluid dynamics solver FLUENT with its user defined functions for rotor modeling and the discrete phase model (DPM) for integrating the trajectories of the particles under the influence of the helicopter flowfield. Rather than modeling the dynamic motions of the individual rotor blades, their effects on the overall flowfield were included in the computations through the Virtual Blade Model. In the computations the solid particles were released into the flowfield from surfaces which were reconstructed out of the data acquired from the flight tests performed within the scope of a project conducted by ASELSAN, Inc. The computed results were compared with the data obtained from these flight tests.

In numerical simulations, a ROBIN validation test case was solved first to find out the most suitable turbulence model for forward flight helicopter analyses in general. Although depending on what part of the helicopter the computations were compared with the available experimental data brought different turbulence models forward, the  $k-\varepsilon$  realizable turbulence model seemed to have covered a larger area on the helicopter where relatively good comparisons with the experimental data were obtained. Hence, in the trajectory computations coupled to the flowfield solutions presented in the thesis, the  $k-\varepsilon$  realizable turbulence model was employed.

The analyses were performed at a 100 Knot forward flight velocity corresponding to the velocity of the helicopter during the flight tests. In comparisons to the flight test data it was observed that in CFD calculations the computed dispersion of particles is much dependent on their initial release surface in the flowfield. Ejecting particles only from a region where birdnesting effects became negligible yielded good agreement with the flight test data. Furthermore, assigning distributed particle velocities in accordance with the experimentally observed velocity distribution at the injection surface significantly improves the predictions. When chaff particles were injected in regions where the birdnesting effect was intact, significant differences between the numerical solutions and test data were observed. Hence, the thesis showed that boundary location and conditions for the particle injection play an important role for predicting chaff dispersion, and the flight test data helped in predicting this phenomenon. In the observed differences, atmospheric disturbances may have also played a partial role. Atmospheric disturbances were not included in CFD calculations.

As future work, models for including the birdnesting phenomenon should be developed. This way there will be not much dependence on flight test data to predict chaff distribution accurately. Also, chaff ejection tests should be carried out under controlled atmospheric conditions to obtain chaff dispersion characteristics in a wider range that can be utilized to develop models.

## REFERENCES

- [1] Yildirim, Z., Self Defense Of Large Aircrafts, M.S. Thesis, Naval Postgraduate School, March 2008
- [2] Characteristics of Chaff, [http://www.globalsecurity.org/military/library/report/enviro/DTI\\_EA/12\\_Appendix\\_A.pdf](http://www.globalsecurity.org/military/library/report/enviro/DTI_EA/12_Appendix_A.pdf), last visited on 22.09.2009
- [3] Ramasamy, M., Contributions To The Measurement And Analysis Of Helicopter Blade Tip Vortices, Ph.D, University of Maryland, 2004
- [4] O'Brien, D., Analysis Of Rotor Fuselage Interactions Using Various Rotor Models, AIAA 2005-0468, 2005
- [5] O'Brien, D., Analysis Of Computational Modeling Techniques For Complete Rotorcraft Configurations, Ph.D, Georgia Institute of Technology, San Francisco, May 2006
- [6] Renaud, T., O'Brien D., Smith M., Potsdam M., Evaluation Of Isolated Fuselage And Rotor-Fuselage Interaction Using CFD, American Helicopter Society 60<sup>th</sup> Annual Forum, 2004
- [7] Hall, C., High Order Accurate Simulations Of Wake And Tip Vortex Flowfields, M.S. Thesis, The Pennsylvania State University, 1998
- [8] Ruith, M., Unstructured, Multiplex Rotor Source Model With Thrust And Moment Trimming - Fluent's VBM Model, AIAA 2005-5217, 2005
- [9] Freeman, C., Mineck R., Fuselage Surface Pressure Measurements Of A Helicopter Wind-Tunnel Model With A 3.15-Meter Diameter Single Rotor, NASA Technical Memorandum 80051, 1979

[10] Mineck, R., Application Of An Unstructured Grid Navier-Stokes Solver To A Generic Helicopter Body, NASA/TM-1999-209510, 1999

[11] Berry, J., Letnikov V., Bavykina I., Chaffin M., A Comparison Of Interactional Aerodynamics Methods For A Helicopter In Low Speed Flight, NASA/TM-1998-208420, 1998

[12] Brunk, J., Chaff Aerodynamics, AD-A019 525 , 1975

[13] Fray, R., Simulation Of Chaff Cloud Signature, 1986

[14] Arnott, W., Hugging A., Kingsmill D., Walker J., Determination of radar chaff diameter distribution function, fall speed, and concentration in the atmosphere by use of the NEXRAD radar, 2004

[15] Leishmann, J., Principles of Helicopter Aerodynamics, Cambridge University Press, 2002

[16] Seddon, J., Basic Helicopter Aerodynamics, BSP Professional Books, 1990

[17] [http://cr4.globalspec.com/PostImages/200907/helicopter-pale-wake-interaction\\_98AD2CA7-D125-7CFC-515169B7EA127DD4.jpg](http://cr4.globalspec.com/PostImages/200907/helicopter-pale-wake-interaction_98AD2CA7-D125-7CFC-515169B7EA127DD4.jpg), last visited on 18.11.2009

[18] I.G.Currie, Fundamental Mechanics Of Fluids, McGraw-Hill, 1993

[19] Phantom V4.2 Datasheet, Vision Research, Inc., <http://www.visionresearch.com/>, last visited on 10.06.2009

[20] Phantom Camera Control Software Documentation, Vision Research, Inc., <http://www.visionresearch.com/>, last visited on 10.06.2009

[21] TrackEye User's Guide, Image Systems AB, 2005

- [22] TrackEye Product Information, Image Systems AB, 2009
- [23] MATLAB 7.5.0 (R2007b) User's Guide, The MathWorks, Inc., 2007
- [24] FLUENT 6.2 User's Guide, Fluent, Inc., 2005
- [25] GAMBIT 2.3 User's Guide, Fluent, Inc., 2005
- [26] TGRID 5.0 User's Guide, ANSYS, Inc., 2008
- [27] Pope, Stephen, . Turbulent Flows, Cambridge University Press, 2000
- [28] Virtual Blade Model,  
[http://www.fluvious.com.au/FLUENT\\_UGM05/UGM05\\_Virtual\\_Blade\\_Model\\_VBM.pdf](http://www.fluvious.com.au/FLUENT_UGM05/UGM05_Virtual_Blade_Model_VBM.pdf), last visited on 17.06.2008
- [29] Mineck, R., Gorton S., Steady And Periodic Pressure Measurements On A Generic Helicopter Fuselage Model In The Presence Of A Rotor, NASA/TM-2000-210286, 2000
- [30] Bettschart, N., Rotor Fuselage Interaction : Euler and Navier-Stokes Computations With An Actuator Disk, American Helicopter Society 55th Annual Forum, 1999
- [31] Knott, E., Lewinski D., Hunt S., Chaff Theoretical/Analytical Characterization And Validation Program, 1981
- [32] Schweitzer, S., Computational Simulation Of Flow Around Helicopter Fuselages, M.S. Thesis, The Pennsylvania State University, 1999
- [33] Prouty, R., Helicopter Performance, Stability and Control, Krieger Publishing Company, 1995
- [34] Black, J., Ellis T., Multi Camera Image Tracking, 2001

[35] Barreto, H., An Introduction To Least Median Of Squares, 2001

[36] Miller, S., The Method Of Least Squares, 2006

[37] Tecplot 360, User's Manual, Tecplot, Inc., 2006

[38] Fieldview 12.1, User's Guide, Intelligent Light, Inc., 2008

[39] Gürsoy Z.E.,A Numerical Investigation of Helicopter Flow Fields in Including Thermal Effects of Exhaust Hot Gases,M.S. Thesis, METU, September 2009